REPUBLIC OF CAMEROON
Peace –Work – Fatherland
****
THE UNIVERSITY OF YAOUNDE I
****
POSTGRADUATE SCHOOL OF SCIENCE, TECHNOLOGY & GEOSCIENCES
****
RESEARCH AND POSTGRADUATE TRAINING UNIT FOR PHYSICS AND APPLICATIONS
****
DEPARTMENT OF PHYSICS
P.O. Box812 Yaoundé
Email: crfdstg@uy1.uninet.cm

REPUBLIQUE DU CAMEROUN
Paix-Travail-Patrie
****
UNIVERSITE DE YAOUNDE I
****
CENTRE DE RECHERCHE ET DE FORMATION DOCTORALE EN SCIENCES TECHNOLOGIE ET GEOSCIENCES
****
UNITE DE RECHERCHE ET DE FORMATION DOCTORALE PHYSIQUE ET APPLICATIONS
****
DÉPARTEMENT DE PHYSIQUE
B.P.812 Yaoundé
Email : crfdstg@uy1.uninet.cm

LABORATOIRE DE MECANIQUE, MATERIAUX ET STRUCTURES

LABORATORY OF MECHANICS, MATERIALS AND STRUCTURES

EFFECTS OF METALATION ON THE NONLINEAR OPTICAL, CHARGE TRANSPORT AND PHOTOVOLTAIC PROPERTIES OF SOME GRAPHENE NANORIBBONS

Thesis presented in partial fulfillment for the obtention of a Doctorate /PhD in Physics

Option: Material Science

By:

Ernest MAINIMO
Matricule : 18z2976

Under the supervision of :
Pr. GEH Wilson EJUH
Associate Professor
University of Dschang

and
Pr. NDJAKA Jean – Marie Bienvenu
Professor
University of Yaoundé I

Year, 2022

UNIVERSITÉ DE YAOUNDÉ I
FACULTÉ DES SCIENCES

UNIVERSITY OF YAOUNDE I
FACULTY OF SCIENCE

DÉPARTEMENT DE PHYSIQUE
DEPARTMENT OF PHYSICS

ATTESTATION DE CORRECTION DE LA THÈSE DE DOCTORAT/PhD

Nous soussignés, Professeur **OWONO OWONO Luc Calvin et** Professeur **Pr HONA Jacques,** respectivement Président et Examinateur du jury de la Thèse de Doctorat/PhD de Monsieur **Ernest MAINIMO**, Matricule ***18Z2976***, préparée sous la supervision des Professeurs **NDJAKA Jean-Marie Bienvenu** et **GEH Wilson EJUH** intitulée : « **EFFECTS OF METALATION ON THE NONLINEAR OPTICAL, CHARGE TRANSPORT AND PHOTOVOLTAIC PROPERTIES OF SOME GRAPHENE NANORIBONS**.», soutenue le **lundi, 05 Décembre 2022**, en vue de l'obtention du grade de Docteur/PhD en Physique, Spécialité **Mécanique, Matériaux et Structures,** Option **Sciences des Matériaux,** attestons que toutes les corrections demandées par le jury de soutenance ont été effectuées.

En foi de quoi, la présente attestation lui est délivrée pour servir et valoir ce que de droit.

Fait à Yaoundé le ..... 16 MARS 2023 .....

Examinateur

Pr HONA Jacques

Président du jury

Pr OWONO OWONO Luc Calvin

Visa du Chef de Département de Physique

UNIVERSITE DE YAOUNDE I * FACULTE DES SCIENCES * Le Chef de Département * DEPARTEMENT DE PHYSIQUE

Pr NDJAKA Jean-Marie Bienvenu

DEDICATION

To

The MAINIMO’s family.

ACKNOWLEDGEMENTS

I thank the Almighty God for His guidance, strength, and knowledge given to me throughout this Thesis.

I seize this opportunity to express my profound gratitude to my supervisors, Professor GEH Wilson EJUH Associate Professor of Physics, University of Dschang, Cameroon and Professor Njaka Jean-Marie Bienvenu Professor of Physics, University of Yaounde I, Cameroon. Their guidance, suggestions, and fruitful discussion have made my journey as a post-graduate student a pleasant experience. Their constant motivations boosted my mindset to finish this Thesis. Their teachings, their sense of humor, their primary concern being my success have been of highest importance to us, not only as scientists but also in my everyday life. I found great joy working with them, discussing with them, not only like supervisors and student but also like a family.

I am thankful to the Council of Scientific and Industrial Research (CSIR), India for financial support through Emeritus Professor scheme (Grant No21(0582)/03/EMR-II) to late Prof. A.N. Singh of the Physics Department, Bahamas Hindu University, India which enabled him to purchase the Gaussian Software. We are most grateful to Late Emeritus Prof. A.N. Singh for donating this software to Prof GEH Wilson EJUH.

I am indebted to Prof GEH Wilson EJUH for donating to me the updated version of the software. He made the necessary materials and guidance available to me throughout this research work. Thank you, Sir.

I am grateful to the Physics Head of Department, Professor NJAKA Jean-Marie Bienvenu Professor of Physics, The University of Yaounde I, Cameroon, for accepting me as his graduate student in the Laboratory of Material Sciences at the Department of Physics.

I am grateful to the Director of the Post graduate school for allowing this Thesis work to be conducted in his school.

My sincere appreciation goes to Pr BEN-BOLIE Germain Hubert, Pr NJANDJOCK NOUCK Philippe, Pr ZEKENG Serge Sylvain and Pr HONA Jacques all lecturers of the Physics Department of University of Yaounde 1, who gave incisive input in term of correction and appreciation during my predefense.

My sincere appreciation goes to the members of Jury, namely: Pr OWONO OWONO Luc Calvin, Pr NJANDJOCK NOUCK Philippe, Pr HONA Jacque, Pr NDOP Joseph, Pr NJAKA Jean-Marie Bienvenu all from the University of Yaounde 1, Pr GEH Wilson EJUH and Pr FOTUE Alain Jerve all from the University of Dschang; for their time and intellectual contributions geared toward the betterment of this Thesis.

I am grateful with the Lectures of the Materials Science Laboratory, Department of Physics, University of Yaounde I and all the Lecturers of the Department of Physics for their teachings, encouragement and the knowledge they have impacted on me and their contributions in one way or the other

I express my special thanks to the post-graduate Students in the Materials Science Laboratory, University of Yaounde I, especially FONKEM Charly Claude for their moral and material support that undoubtedly contributed toward the success of this work.

I would like to express my gratitude to the University of Yaounde I for providing a joyful and peaceful environment and for accompanying us towards our success. Not forgetting the students and lecturers of the Condensed Matter Division of the University of Dschang, from where I earned my Master's Degree.

I thank my wife MAINIMO Mary and children: MAINIMO Percy, MAINIMO Synder and MAINIMO Alvery supporting me and standing by me throughout this period of my Thesis.

I owe immense thanks to my entire family (immediate and extended) and friends especially Mr. MENGJO Fonyuy Francis and Vincent De Paul NYUYKI, for their patience, love and moral support throughout this exercise.

Special thanks to Dr NYISOMEH Ibrahim, Mr FONKA valentine, for your words of encouragement from the beginning to the end of this work.

I wish to thank all those whose names might not have been mentioned above, but who contributed in one way or another toward the realization of this piece of work

TABLE OF CONTENT

LIST OF ABBREVIATIONS

NLO	nonlinear optical
HLS	Harmonic Light Scattering Electric Field Induced Second Harmonic Generation
TPA	two-photon absorption
SHG	second-harmonic generation
D	donor unit
A	acceptor unit
OPL	optical power limiting
FOM	figure of merit
MO	molecular orbitals
HOMO	highest occupied molecular orbital
LUMO	lowest unoccupied molecular orbital
PV	photovoltaic
SM	semiconductor material
ISM	inorganic semiconductor material
OSM	organic semiconductor material
OPVC	organic photovoltaics cell
DFT	Density Functional Theory
GNR	graphene nanoribbon
FET	field-effect transistor
MWCNT	multiwalled carbon nanotubes
CVD	chemical vapor deposition
GIC	graphite intercalation compound
GO	graphene oxide
STM	scanning tunneling microscopy
DBBA	10, 10'-dibromo-9,9'-bianthryl
AGNR	armchair graphene nanoribbons
HOPG	highly oriented pyrolytic graphite

AFM	atomic force microscopy
VLSI	Very large scale Integration
PCE	power conversion efficiency
P3HT	poly(3-hexylthiophene)
PCBM C60	phenyl-C61-butyric acid methyl ester
V_{oc}	open circuit voltage
FF	fill factor
QE	quantum efficiency
EQE	External Quantum Efficiency
IPCE	Incident Photon to Charge Carrier Efficiency
IQE	Internal Quantum Efficiency
FTO	fluorine-doped tinoxide
HTL	hole transport layer
PES	Potential Energy Surface
HF	Hartree–Fock
SCF	self-consistent-field
LCAO	Linear Combination of Atomic Orbitals
RHF	Restricted Hartree–Fock
UHF	Unrestricted Hartree–Fock
ROHF	Open-Shell Hartree–Fock
CI	Configuration Interaction
CC	Coupled Cluster
MP	Møller-Plesset
TDDFT	Time – Dependent Density Functional Theory
H – K	Hohenberg and Kohn
KS	Kohn Sham
LDA	Local density approximation
VWN	Vosko, Wilk and Nussair parameterization
LSDA	Local spin density approximation
GGA	Generalized gradient approximation

BLYP	Becke Lee, Yang and Parr
BP86	Becke's 1988 exchange functional and the Perdew's 1986 correlation functional
PBE	Pewdew, Burke and Ernzerhof
M06-L	Minnesota functional
TPSS	Tao–Perdew–Staroverov–Scuseria functional
B3LYP	Becke's three-parameter Lee-Yang-Parr
CAM B3LYP	Coulomb-attenuating method Becke's three-parameter Lee-Yang-Parr
STO	Slater-type orbitals
GTO	Gaussian type orbitals
CGTO	contracted Gaussian type orbitals
ANO	atomic natural orbital
SZ	single-zeta
DZ	double-zeta
TZ	triple-zeta
QZ	quadruple-zeta
IR	infrared
NMR	normal magnetic resonance
IP	ionization potential
EA	electron affinity
QSAR	quantitative structural analysis relationship
p-NA	*para*-nitroaniline
FMO	Frontier molecular orbitals
CT	charge transfer
DOS	density of state
TPD	N,N-diphenyl-N,N-bis(3-methlphenyl)-(1,1-biphenyl)-4,4-diamine,
Alq3	tris(8-hydroxyquinolinato)aluminum(III)
OLED	organic lead emitting diode
BHJ	bulk heterojunction junction
ZPVE	Zero-point vibrational energy
au	atomic units
ANSI	American national standard Institute

LIST OF FIGURES

LIST OF TABLES

ABSTRACT

In this study, we investigated the effects of metalation on the nonlinear, mechanical and charge transport properties of some small organic graphene nanoribons (GNRs) molecule. a theoretically investigation is done using the ab initio, rhf, together with the DFT, B3LYP and BPBE methods together with the 6-31+g(d,p) basis set integrated in Gaussian 09. Results reveals the metalated GNRs have a higher nonlinear optical activity than the virgin counterpart. Interestingly these GNRs metal derivatives also have a remarkable nonlinear optical effect in comparison to the classical push-pull organic crystal; *para*-nitroaniline and urea. Other remarkable results show that as compared to the starting GNRs the metalated counterparts are excellent ambipolar charge transport carriers, better than the prototypic electron transport Alq3 (tris(8-hydroxyquinolinato)aluminum(III), and hole tranport TPD (N,N-diphenyl-N,N-bis(3-methlphenyl)-(1,1-biphenyl)-4,4-diamine. However, the metal derivative have diminished mechanical stability than the starting molecule. Metalated GNRs could be therefore potential candidates for the fabrication of optoelectronic and photonic devices for second and third-order NLO application. The study was also carried out to determine if GNRs could act as potential donor material in organic photovoltaic cells. Analysis is made on HOMO, LUMO, band gap, reorganization energy, open circuit voltage, the driving force, and nonlinear optical properties. These organic photovoltaic properties are predicted with the aid of PCBM as modelled acceptor. Results reveal positive agreement with traditional classical and experimental organic values, presenting the fact that metalated GNRs and in some cases the virgin GNR may be used as an effective and potential donor of electron in organic Bulk Heterojunction solar cells, owing to their enhanced nonlinear and photovoltaic properties. The values obtained for the reorganization energy, driving force and nonlinear optical properties are promissory properties that may be directly implemented in the investigated photovoltaic material. The power conversion efficiency obtained for Rb-perylene is seen to be around the maximum current value for organic photovoltaic cell. Rb-perylene shows the best organic photovoltaic properties followed by k-azulene then k-phenanthrene. The results in this research might aid in computer assisted-design of OPV materials.

Keywords: Graphene nanoribons; nonlinear optical properties; charge transport, mechanical stability; metalation; organic photovoltaic; power conversion efficiency; Bulk Heterojunction solar cells.

RESUME

Dans cette étude, nous avons étudié les effets de l'ajout d'un métal sur les propriétés non linéaire, mécanique et le transport de charge de certaines petites molécules organiques de type nanoribons de graphène. une étude théorique est effectuée en utilisant les méthodes ab initio (rhf), ainsi que les méthodes de théorie de la fonctionnelle de la densité (DFT), en utilisant les fonctionnelles B3LYP et BPBE avec la base 6-31+g(d,p) intégrée dans Gaussian 09. Les résultats révèlent que les nanoribons de graphène métallisés présentent une non linéarité optique plus grande que sa contrepartie vierge. Il est intéressant de noter que ces dérivés métalliques de nanoribons de graphène ont également un effet optique non linéaire remarquable par rapport au cristal organique classique, la para-nitroaniline et urée utilisées comme référence dans l'optique non linéaire. D'autres résultats remarquables montrent que par rapport aux nanoribons de graphène de départ, leurs homologues métallisés sont d'excellents porteurs ambipolaire de charge, mieux que le transporteur d'électrons classique Alq3 (tris(8 hydroxyquinolinato)aluminium(III) et le transporteur de trous TPD (N,N-diphényl- N,N-bis(3-méthlphényl)-(1,1-biphényl)-4,4-diamine. Cependant, le dérivé métallique a une stabilité mécanique diminuée par rapport à la molécule de départ. Les nanoribons de graphène métallisés pourraient donc être les candidats potentiels pour la fabrication de dispositifs optoélectroniques et photoniques pour l'application non linéaire de deuxième et troisième ordre. L'étude a également été menée pour déterminer si les nanoribons de graphène ainsi que ses contreparties vierges pourraient servir comme matériaux donneurs potentiel dans les cellules photovoltaïques organiques. L'analyse est faite sur l'orbitale moléculaire la plus occupée, l'orbitale moléculaire la plus basse inoccupée, la bande interdite, l'énergie de réorganisation, la tension en circuit ouvert, la force motrice et les propriétés optiques non linéaires. Ces propriétés photovoltaïques organiques sont prédites à l'aide de PCBM comme accepteur modélisé. Les résultats révèlent une concordance avec les valeurs organiques classiques et expérimentales supplémentaires, présentant le fait que les nanoribons de graphène métallisés et, dans certains cas, les nanoribons de graphène vierge peuvent être utilisés comme donneur potentiel des électrons dans les cellules solaires organiques, en raison de leurs propriétés non linéaires et photovoltaïques améliorées. Les valeurs obtenues pour l'énergie de réorganisation, la force motrice et les propriétés optiques non linéaires sont des propriétés prometteuses qui peuvent être directement implémentées dans le matériau photovoltaïque étudié. Le rendement de conversion de puissance obtenu pour le Rb-pérylène se situe autour

de la valeur de courant maximale pour une cellule photovoltaïque organique. Le Rb-pérylène présente les meilleures propriétés photovoltaïques organiques suivi du k-azulène puis du k-phénanthrène. L'approche méthodologique proposée dans cette recherche pourrait aider à la conception assistée par ordinateur de matériaux photovoltaïques organiques.

Mots clés: nanoribons de graphène ; propriétés non linéaire, porteur du charge ; stabilité mécanique ; l'ajout de métal ; propriétés photovoltaïques organiques ; rendement de conversion de puissance ; cellules solaires organique

GENERAL INTRODUCTION

The quest for suitable materials to be used in optoelectronics and photonics devices has been of great importance in Physics, Chemistry and Materials science. Due to the fact that photons can carry information faster, more efficiently and over larger distances than electrons. Systems that use light as carrier of information are of great interest to information and communication technologies. Materials which exhibit high nonlinear optical (NLO) responses have been potential candidates for such devices, because of their high processing speed, transmission and data storage. The importance of molecular and nanomaterial engineering for science and technology has highly increased during the last 10 years. Materials with high nonlinear optical (NLO) activity may be used as electro-optic switching elements for telecommunication and optical information processing. Therefore, the design of NLO molecules has become a focus of current research. The NLO process requires materials that control the amplitude, phase, polarization and frequency of optical waves. In this context, a variety of dipolar and octupolar complex materials such as organometallic, photochromic, lanthanides and lanthanide complexes are synthesized and studied by powerful tools, e.g. Harmonic Light Scattering (HLS) and Electric Field Induced Second Harmonic Generation (EFISH) to determine their first hyperpolarizability (β). The NLO properties of these materials are tailored by using different donor and acceptor groups, metals and π-conjugation backbones. In recent times, many organic conjugated molecules have been found to exhibit extremely large nonlinear optical (NLO) responses such as second-harmonic generation (SHG) and two-photon absorption (TPA). Contrasting with traditional inorganic nonlinear crystals, organic molecular materials or polymers have many superior properties including ultrafast response times, lower dielectric constants, high damage threshold and flexible design with modern chemical synthetic techniques. Because the NLO response of these molecular materials is mainly governed by the characteristics of the constituent chromophores, the search of novel molecules with large NLO properties at desirable wavelengths becomes a highly active area of research at present. Theoretical investigations on possible structure-to-property relationships are very important for the design and synthesis of NLO materials with optimized performance. Organic molecules with π-conjugated scaffolds end-capped with electron donor and acceptor groups are widely investigated due to their immense application potentials and hence they belong to a promising area of organic chemistry. In these types of systems, the intra molecular charge transfer will occur from the donor unit (D) to the acceptor unit (A). Due to the interaction between the donor

unit and acceptor unit a set of new low-energy molecular orbitals (MO) are generated, which shift the absorption maximum to longer wavelengths in comparison to the individual uncoupled systems. Such systems are generally referred as charge-transfer chromophores [1-4]. The interaction between the donor and acceptor can occur through a bond or through space fashion. Stronger electronic coupling is observed when the donor and acceptor groups are in conjugation with each other. Such conjugated electron donor-acceptor (D-A) molecules are termed as "push-pull" systems. They have received increasing attention in the area of research focusing the development of organic materials for nonlinear optics, electro-optics, piezochromism, solvatochromism and photovoltaics. In such D-A frameworks, HOMO and LUMO energies can be easily tuned by appropriate structural modifications. By careful optimization of structural motifs the morphology of the self-assemblies in the solid-state can be tuned to the requirement of the application scenario. The extent of electronic coupling between the donor and acceptor groups govern the HOMO–LUMO energy gap and thereby control the first order linear optical properties and higher order nonlinear optical (NLO) properties. Some of the structural features that control these properties are (i) ionization potential of the donor and electron affinity of the acceptor (ii) extent of D-A interaction, (iii) topology of π-conjugation, (iv) degree of π-conjugation and (v) planarity of the molecule structure.

Organic molecules have received increasing attention in the area of research focusing the development of organic materials for nonlinear optics [5-7] and photovoltaics [8-10]. In such D-A frameworks, HOMO and LUMO energies can be easily tuned by appropriate structural modifications, achieved in this Thesis by the process of adding metal (metalation) to some chosen group of organic materials called graphene nanoribbons

It has been found that several structural factors, such as the electron richness of the π - conjugation center, the strength of donor and/or acceptor substituents, the planarity of the π - conjugation center, the molecular symmetry, and the dimensionality of charge transfer networks are particularly important for increasing the TPA activity of single organic conjugated molecule [11-15].

Industrialization, a drastic rise in the population and globalization, has increased the demand for sustainable and clean energy sources manifold ever than before. Moreover, conventional energy resources are rapidly depleting and concurrently creating problems such as global warming/environment pollution etc. In order to cope with these issues, clean and economical energy sources are in great demand as an alternative to oil and fossil fuels. Hence, researchers

have shown considerable interests in exploring alternative energy resources. As a matter of fact, the sun is the source that provides an abundance of renewable solar energy and is a viable source to realize the dream of cheaper and green energy. Apparently, the sunlight supplies approximately 10^4 times larger energy than our present needs. However, the biggest challenge is the conversion of solar energy into electrical energy in addressing the issue of world energy demands over a longer period of time through cheaper and environment-friendly technologies. In resolving the issue, photovoltaic (PV) technology is the most practical and attractive approach to exploit the sustainable energy source at all level as well as to overcome future energy crisis. The demands on PV technology are rapidly increasing with time [16]. The key to exploiting PV technology is majorly relying on the semiconductor materials (SMs) since solar energy is converted into electricity directly [17, 18], by manipulating the potential of SM materials. Day by day, this technology is attracting more and more attention of researchers towards exploring, tailoring and investigating the new and better SMs, which can realize the dream of green/sustainable energy. Although some SMs are already exploited in the technology, most of the modules are based on inorganic semiconductor materials (ISMs). Recently, researchers have diverted their interests in the organic SMs (OSMs) as well. It is due to the fact that the PV modules that are based on the conventional ISMs are very expensive if compared to the OSMs. Moreover, the optoelectronic device manufacturing based on the OSMs is easier than the ISMs. Regardless of the advantages, OSMs -based device efficiency is rather low [19-21]. Hence, the study of OSMs generally seeks opportunities to dominate in PV technology with enhanced performance over the current market of conventional crystalline silicon and other ISMs. The OSM-based device of organic photovoltaics (OPV) is thin, light and flexible. The versatility of OPV as the future energy efficient technology is paving towards replacing the utilization of conventional silicon in the mass production. Some examples of OPV technology that have been introduced these days are OPV polymers, OPV DSSC (dye-sensitized solar cells) and OPV oligomers. OPV devices consist of one or several photoactive OSMs overlaid between two electrodes of cathode and anode [19] Photoactive OSMs play a key role in the performance of optoelectronic/photovoltaic devices. OPVC fall into three categories: Organic and Polymer solar cells, Perovskite solar cells, and Photoelectrochemical cells - Organic dye sensitized solar cells (DSSC). We investigate the first category of polymer solar cell. Therefore, in order to determine suitable and efficient photoactive OSMs and attain their respective properties, comprehensive investigations on their electronic structure and optoelectronic properties are necessary. In this regard, the use of ab initio and density functional

quantum mechanical computational techniques in performing virtual experiment may lead to a cheaper experiment and shorter developmental cycle.

Computational ab initio methodologies based on Density Functional Theory (DFT) are intensely used by the theoretical researchers to solve complex problems. It was found to be more reliable and provides better results concerning the electronic structure calculations in designing and modeling new materials and tuning their properties without prior experimental knowledge. This feature of DFT has brought a new insight into research and education field.

The aim of this Thesis is to study the electronic and optical properties of a class of organometallic semiconductor materials in the form of GNRs for optoelectronic and organic photovoltaic applications using the theoretical approach

In order to achieve the aim of this Thesis, the following objectives are to be perform:

i) To optimize the geometrical structure of some GNRs organic materials (phenanthrene, azulene and perylene) as well as their organometallic counterpart

ii) To investigate the effects of metalation on the NLO, transport, OPV, mechanical, and thermodynamic properties of the GNRs

iii) To compare and contrast the properties of the virgin GNRs with their metalated counterparts

iv) To simulate OPV device based on GNRs and investigate its efficiency

As to the significance of this research work, this offers comprehensive study on optoelectronic properties of various organic materials based on GNRs that covered from molecule to crystal level and depicts the organic material potential in optoelectronic and OPV applications through computational approaches. In order to spawn a new generation of optoelectronic and solar-powered products which give benefits in several aspects of cost/money, sustainability, lifetime and environmental friendliness, the research was conducted through the state-of-the-art ab initio and DFT methods. Moreover, prediction of properties, that have not yet been explored experimentally, are determined within a short time and at low cost. This research will assist to solve the problems which constantly arise and are difficult to decipher experimentally. The computed optical and electronic properties highlight the promising future of organic material in optoelectronic and OPV technology. In addition, this research may provide promising characteristics of optoelectronic and OPV materials that could be a strong footing to the experimentalist, academicians, and industrial scientists to fabricate optoelectronic devices

based on the GNRs that are beneficial to the country, community and future generation of green energy technology.

Apart from the general introduction we have presented, which comprised of a background study, aims, objectives and the significance of the research work, this Thesis is subdivided into three chapters.

Chapter 1 comprises of the literature review on the advances in organic nonlinear response and OPV properties. It also explores recent works and rationale of investigating GNRs for NLO and OPV applications.

Chapter 2 is devoted to materials and methods. In this section we present the method used to model our molecular system for study based on molecular and quantum mechanics. Here we present clearly the tools and methods used to calculate the properties under investigation.

Chapter 3 is dedicated to the presentation of results and discussion. We end with a general conclusion and perspectives.

CHAPTER 1
LITERATURE REVIEW

1.0 Introduction

Atomically precise graphene nanoribbons (GNRs) attract great interest because of their highly tunable electronic, optical, and transport properties. Graphene nanoribbon (GNR) is a one sheet of graphite (monolayer) consisting of sp2 hybridized carbon atoms, it is creating a regular honeycomb (hexagonal) lattice in 2D. GNRs has attracted considerable importance in the industry and research community due to their outstanding properties. Quite recently, there has been large importance towards the study and realization of GNRs based on optical devices designed by appropriate tailoring of the electronic structure, exploiting not only the electric field effect but also other properties as applied strain. In other word, the GNRs have stimulated enormous outburst in research in both theoretic and experiment fields [22-26]. In recent years there has been extensive and much interest on molecules with large non-linearities, while the focus of current research is on GNRs and potential applications in various photonic and organic photovoltaic technologies, organic molecules in general and GNRs in particular exhibits numerous attractive NLO characteristics [27]. The extraordinary characteristics of GNRs has attracted keen interest, which has expanded its horizon of research fields. Consequently, there is significant progress in the numerous fabrications of this materials. Furthermore, organic molecules generally and GNRs on the other hand are becoming basic components in the advance of optoelectronics, and optical nano devices. Since the invention of the laser, photonics has emerged as a multidisciplinary field of science and technology that has captured the imagination of scientists and engineers because of its potential applications. Photonics is an analog to electronics, where in place of electrons, photons facilitate the generation, transmission, modulation and other processes associated with the manipulation of light.

We start this chapter with a presentation of the structure and classification of GNRs, their preparation and purification, their toxicity and their properties and applications. Then we proceed to discuss nonlinear optical effect, charge transport and photovoltaic effect in organic molecules of which GNRs form part.

1.1 Structure and classification of graphene nanoribbons

Graphene nanoribbons (GNRs) are planar, finite, quasi-one-dimensional graphene structures. They are generally categorized by the structure of their long edges, which can have an armchair, a zigzag, or an intermediate character as in fig. 1.1. This edge structure has profound implications for the electronic properties of the GNRs. Generally, GNRs are semiconducting, but the one-dimensional band structure and specifically the size of the band gap depend critically on the edge geometry. Its isolation in 2004 and the extensive research that followed has led, to electronic structure components having nano-scale dimensions and semiconducting or metallic electronic properties that depend on its geometry and dimensions. These characteristics of GNRs are in stark contrast to those of graphene, which is a carbon sheet with semimetal, zero band gap characteristics. More specifically, GNRs are predicted to exhibit electronic properties that are dictated by the ribbon width and the shape of the edges [28, 29]. In terms of their edge structure, GNRs can be categorized as zigzag- or armchair-edged. The difference between these two GNRs types is that zigzag-edged GNRs possess a localized nonbonding π state around the zigzag edges, while armchair-edged GNRs lack such a state. The localized nonbonding π state is predicted to yield specific magnetic activities in GNRs. This peculiar electron localization, along with the symmetry-broken spatial spin distribution in zigzag GNRs, is referred to as the "edge state". Zigzag GNRs are predicted to be always metallic, whereas armchair GNRs can be metallic or semiconducting depending on their width [28, 29]. The quasi one-dimensional nature of GNRs results in additional advantages over graphene sheets, the more widely known two-dimensional counterpart to GNRs. For example, the high aspect ratio of GNRs significantly lowers the percolation threshold in conductive films and polymer composites, and renders them suitable for spinning fiber from their liquid crystalline alignment.

GNRs possess band gaps that distinguishes them from extended, two-dimensional graphene and, together with a high charge carrier mobility, making them interesting materials for a variety of applications such as radio-frequency transmitters or field-effect transistors (FETs) [30]

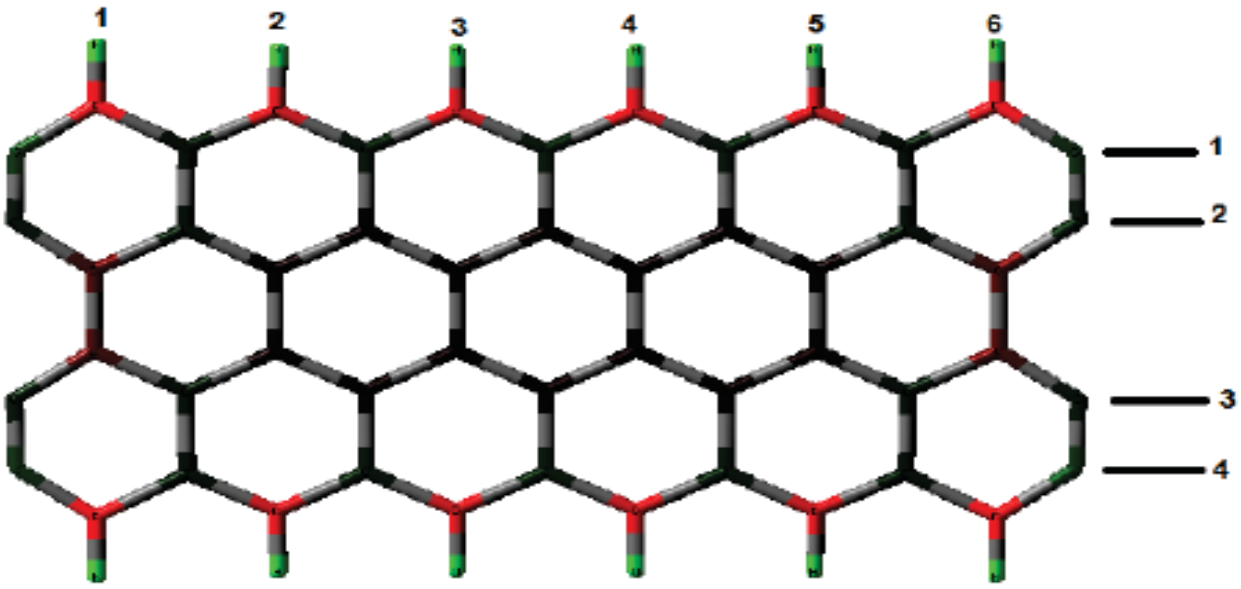

Fig. 1.1: Rectangular GNR with width = 4 (in the armchair trend) and length = 6 (in the zigzag trend), viz: designated as GNR [4, 6]

1.2 Synthesis of GNRs

To date, GNRs are obtained following two very different strategies, namely the top-down (the breaking down of large preformed carbon-based structures) and the bottom-up (the assembly of simple building blocks into a complex structure). Top-down techniques involve the unzipping of carbon nanotubes using an e-beam [31] or via chemical oxidation using potassium permanganate and sulfuric acid [32], by intercalating lithium into multiwalled carbon nanotubes (MWCNTs) followed by thermal expansion, [33] and by longitudinal splitting of MWCNTs using transition metal clusters [34]. GNRs have also been prepared via the etching of graphene by lithography, [35] by plasma chemical vapor deposition (CVD) under a Ni bar [36], via mechanical exfoliation of highly-oriented pyrolyzed graphite (HOPG) [37], through solution-based exfoliation of graphite intercalation compounds (GICs) [38], by chemical oxidation/exfoliation of graphite followed by reduction of the resulting graphene oxide (GO) [39-42], as well as resist-based patterning [43] and scanning tunneling microscopy (STM) patterning. [44] While top-down methods have the advantage of producing GNRs with micrometer length, they frequently involve complicated procedures, they lack reproducibility, and the final materials have poorly-defined chiralities. Furthermore, top-down-produced GNRs' edge structures feature a large number of defects and the width of the ribbon can be larger than the molecular dimensions.

On the other hand, bottom-up techniques can afford GNRs with distinct structural and geometrical characteristics (defined edge type and narrow widths), without edge abnormalities, very low polydispersity, and the potential for scale-up [45-47]. Importantly, the precursor monomers used to chemically synthesize the GNRs define the ribbon dimensions, which in turn dictates the band gaps and electronic properties of the final material. On this basis, producing GNRs with tailor-made predefined widths, edge structure geometries and suitable solubility constitutes an important challenge for synthetic chemists. While bottom-up synthesis in solution allows for growth of large quantities of GNRs with relatively large lengths on the order of hundreds of nanometers, the solubility of the GNRs and thus the ability to create a dispersed solution is a major challenge. An alternative synthesis pathway is the bottom-up synthesis on surfaces. This approach allows exploitation of catalytic properties of the substrate and furthermore offers the possibility to study the structural and electronic properties of individual, immobilized GNRs on a sub-molecular level with scanning probe techniques.

We will discuss just the processes involved in the on-surface bottom-up synthesis of GNRs and the different types of GNRs realized in this manner up to date.

On-surface bottom-up synthesis of GNRs

In 2007, Hecht and coworkers pioneered the covalent on-surface synthesis of molecular nanostructures [48]. They used thermal activation of Br-substituted porphyrin-building blocks on Gold to form a covalently bonded molecular network on the surface. Since then, this concept has been extensively used to form different kinds of two-dimensional networks [49-54] and one-dimensional molecular wires [55-57] on metal substrates. It has also been shown that aryl halides can perform thermally induced coupling reactions on insulators [58-62]. The dehalogenation barrier varies with halogen and substrate, which has been exploited for hierarchical growth of molecular networks using iodinated and brominated monomers in two subsequent annealing steps [63, 64].

Three years later, Müllen, and coworkers applied this concept of thermally induced on-surface synthesis to the fabrication of GNRs [65]. Using a Br-substituted bianthryl monomer (10, 10'-dibromo-9,9'-bianthryl, DBBA,), they were able to grow an armchair GNR (AGNR) with a width of N=7 carbon atom rows (thus labeled 7-AGNR) on Au(111). Upon deposition of the monomers onto the surface, the GNR synthesis proceeds in two on-surface reaction steps at different temperatures, both of which rely on the catalytic activity of the metal substrate. First, at 200^{o}C, dehalogenation and homo-coupling of the monomers lead to the formation of a three-

dimensional polyanthrylene intermediate with anthracene units coupled only through single σ-bonds. In the second reaction step at 400°C, this polymer undergoes a cyclodehydrogenation reaction which yields a flat, fully aromatic 7-AGNR with a width of less than 1 nm. The well-defined armchair edge structure and the low-defect density of the resulting GNRs are evident in non-contact atomic force microscopy (nc-AFM) topographs [66].

1.3 Purification of GNRs

As mentioned above, with currently known GNRs manufacturing methods, compositions contain not only the desired target GNR but also contaminants are obtained. The term “contaminant” refers to components of a GNR composition having a structure and properties different from those of the "target" graphene nanoribbons (GNR1) to be purified. Depending on the manufacturing method used, the type of contaminants may vary. Typical contaminants of the graphene nanoribbons manufacturing process (e.g., a GNR production process by a cyclic hydrogen desorption reaction in a solution-based process or a surface-assisted process) include unreacted precursor molecules, unreacted precursor polymers, graphene nanoribbons (e. g., originating from the catalyst) that are not structured, aggregates (e.g., agglomerated particles that cause aggregate structures that are too large to be effectively dispersed), solid substrates, and/ or metal residues. In the GNR manufacturing method using the surface-assisted cyclic hydrogen elimination reaction of the precursor polymers, the solid substrate on which the graphene nanoribbons (GNR1) are provided also exhibits a contaminant. Typically, the contaminants are non-GNR materials. However, contaminants may also include graphene nanoribbons (GNR2) that differ in at least one characteristic from graphene nanoribbons (GNR1). Severally methods of purification exist, we will list only 2 methods.

A method for purifying GNRs consists of contacting a composition comprising graphene nanoribbons (GNR1) and one or more contaminants with a liquid medium comprising a dispersing agent, dispersing the graphene nanoribbons (GNR1) in the liquid medium, obtaining a liquid dispersion of ribbon GNR1, separating the liquid dispersion of graphene nanoribbons (GNR1) to obtain a liquid dispersion of purified graphene nanoribbons (GNR1) by at least partially removing the one or more contaminants.

Another method exist wherein the separation process comprises filtration, centrifugation, density gradient centrifugation, chromatography, electrophoresis, precipitation, or any combination thereof.

1.4 Toxicity of GNRs

The increased utilization of GNRs for biomedical and material science applications, necessitates the thorough evaluation of potential toxicity of these materials under both intentional and accidental exposure scenarios. GNRs have not only proved valuable in materials research, but are also in the process of being developed for drug delivery, imaging and other therapeutic applications. Yet, reports indicate that graphene nanoparticles, depending on their chemical compositions and method of synthesis, show diverse effects in terms of oxidative stress, uptake and toxicity in cells and tissues [67]. With the advancement of use of graphene-based nanomaterials in research and industry, they may ultimately end up in landfills and eventually in nearby surface and groundwater bodies [68, 69]. Graphene nanoparticles have shown to be stable in surface water and thus could ultimately have adverse effects in the surface and subsurface organisms in natural water bodies [68]. Comparative studies of graphene-based nanoparticles in both cell lines and zebrafish embryos indicate that the shape of the materials influences both absorption and toxicity [70,71]. Recently, a number of studies have evaluated the biodistribution and toxicity of graphene-based nanoparticles in cell lines, and small animals [72-74]. These studies report a size- and concentration-dependent decrease in cell viability [75]. GNRs can enter cells through membrane penetration and cause oxidative stress [76]. Some GNRs depending on their shape have been shown to cause mitochondrial injury [77], and cell cycle alterations [78]. A study reported that both bath and probe sonication of oxidized GNRs result in increased hemolysis of red blood cells however, these sonicated oxidized GNRs were less toxic to fibroblasts as compared to unsonicated aggregated oxidized GNRs sheets [79]. Other studies show oxidized GNRs could penetrate into the cells and cause DNA fragmentations as well as chromosomal aberrations, even at low concentration of 1.0lg/mL after short exposure time of 1hour [80].

1.5 Properties and application of GNRs

GNR has attracted considerable importance in the industry and research community due to its outstanding properties. Its fascinating electrical, optical, and mechanical properties have ignited enormous interdisciplinary interest from physics, chemistry and materials science fields [80-83]. The newly discovered properties pave the way to applications in transparent conductive films, electronic and optoelectronic devices, actuators, sensors, composites, and much more. Graphene is a promising material for high-performance electronics owing to its exotic electronic structure and high mobility. The charge transport properties and device

performances of GNRs depend highly on the quality of the materials and their synthesis methods. We would like to stress here that recently GNRs have been used in many other applications, such as in composite materials [84, 85], thin film coatings [86, 87] and energy storage [88, 89]. Also multi-layer GNR has been proposed and considered as an emerging interconnect material in future (Very large scale Integration) VLSI technology [90]. One of the most attractive applications of GNRs is in logic transistor. Great efforts have been made in this area with GNRs fabricated by various techniques, such as sono-chemical, top– down etching, MWCNT-unzipping, molecular assembly, gas atmosphere etching, plasma etching [91]. Besides logic transistor applications, GNRs are also interesting in terms of quantum devices. GNRs with short channel lengths are analogous to graphene quantum dots and potentially suitable for single electron transistors. As previously discussed, the edge quality greatly influences the transport behavior and device performance. At low temperature, narrow etched GNRs act as a series of quantum dots [92]. On the other hand, high quality GNR could behave like single quantum dot at low temperature with well-defined Coulomb blockade diamonds [93]. We also remark that GNRs can be used as charge detectors to detect individual charging events in graphene nano-systems [92], where the Coulomb blockade resonances of the nano-systems can be barely measured because the current levels are too low.

Another potential device application of GNR lies in optoelectronics [93, 94] because of its tunable band gap and GNRs have been demonstrated to exhibit strong nonlinear optical and optical limiting response [95]. These results demonstrate the practical applications of GNRs in high performance nanometer-scale optical devices. We also expect more advanced devices such as resonant tunneling diodes and photovoltaic devices based on GNR heterostructures to emerge in the near future.

1. 5. 1 Nonlinear optical properties of GNRs

GNRs produce interesting NLO properties. This NLO process occurs when a molecule is subjected to a strong electric field $\vec{E}$, which polarizes the molecule. The polarization $\vec{P}$ is linked to the electric field by $\vec{P} = \mathcal{E}\chi\vec{E}$, where χ is the electric susceptibility of the material. The susceptibility is an inherent parameter of a material. Generally the susceptibility is a function of the electric field applied to a material, thus in the presence of a strong electric field, the polarization induced to the material can be described in a Taylor series expansion

$$\vec{P} = \varepsilon_0\chi\vec{E} = \varepsilon_0\left(\chi^1 + \chi^2\vec{E} + \chi^3\vec{E}^2 + \cdots\right)\vec{E} \qquad 1.1$$

Where χ^j is the susceptibility of j order. χ^1 is the first order susceptibility which determines the linear polarization $\vec{P}^L$ of the molecule given by

$$\vec{P}^L = \varepsilon_0 \chi^1 \vec{E} \qquad 1.2$$

The second and third order susceptibility χ^2 and χ^3 respectively and other higher order susceptibility are given by the nonlinear polarization $\vec{P}^{NL}$,

$$\vec{P}^{NL} = \varepsilon_0 \left(\chi^2 \vec{E} + \chi^3 \vec{E}^2 + \cdots\right) \vec{E} \qquad 1.3$$

Also a dipole moment can be induced into a material subjected to an electric field. In the presence of a strong electric field $\vec{E}(\omega)$ of frequency ω, the dipole moment can be described in a Taylor series expansion by

$$\mu_i(\vec{E}) = \mu_0 + \sum_j \alpha_{ij} E_j + \sum_{j \le k} \beta_{ijk} E_j E_k + \sum_{j \le k \le l} \gamma_{ijkl} E_j E_k E_l + \qquad 1.4$$

μ_0 is the permanent dipole moment of the molecule, α_{ij}, β_{ijk} and γ_{ijkl} are tensors representing the polarizability, the first order hyperpolarizability and the second order hyperpolarizability respectively. α_{ij} gives the linear response of the molecule, while β_{ijk} and γ_{ijkl} determine the nonlinear response of the molecule. The hyperpolarizability tensor is an important factor used in the search of molecules with large nonlinear response used in the field of optoelectronics where photons play the role of electrons in electronics [96,97]. The dipole moment and the polarizability are also very important in the calculation of other optoelectronic properties of a molecule as shown by ejuh [98].

Nanostructured graphene systems, such as graphene nanoribbons and nanoislands, have been predicted to have a strong plasmon-enhanced nonlinear optical behavior in the nonretarded regime.

Plasmons concentrate the light field down to subwavelength scales and can enhance the nonlinear optical effect. GNRs, particularly armchair GNRs, have a remarkably strong nonlinear optical response in the long-wavelength regime and over a broad frequency range from terahertz to the near infrared [99]. Also, there are a number of theoretical papers on the nonlinear optical properties of graphene [28–38] and nanostructured graphene, such as graphene nanoribbons (GNRs) [100, 101]. Apart from the invaluable physical properties, two dimensional graphene can be patterned into narrow ribbon that causes the carriers to be

confined in quasi-one-dimensional GNRs (with the diverse topologies depending on the ribbon form) [43,102]. Although the band structure of a GNR differs for patterns with different boundaries, a common feature of the GNRs is a width-dependent sizable band gap [103] suitable and significant for nano-optoelectronics. Such nanostructures exhibit optical properties fundamentally different from those of graphene [104-106]. At the same time, carriers in GNRs have the same outstanding transport properties as in graphene. Strong near electric fields generated by plasmons in graphene nanostructures can be exploited to enhance nonlinear optical processes [107]. Another important advantage of GNRs over extended graphene monolayer is the confinement of quasiparticles in GNRs in the one additional dimension. In another research by Avetissian [108], it has been shown that the width size and Fermi energy level of the GNR in the nonlinear optical response are quite considerable [109]. It has become increasingly apparent that the future of next generation of electronic devices can and will rely on graphene nanoribbons. Graphene nanoribbons and sister structures showcase several key properties that can address the emerging need of terahertz science and technology, and break through the many technological limits on conventional semiconductor electronics operating in the terahertz spectrum. One of the most striking features of GNRs is the high sensitivity of their properties to the details of the atomic structure. In addition to an overall decrease of energy gap with increasing ribbon width, also observed experimentally [43, 110] theoretical studies predict a superimposed oscillation feature [111], which is maximized for A-GNR. GNRs are intriguing systems with tunable optoelectronic features, which we quantitatively evaluate through our calculations. A combined theoretical and experimental understanding of ribbon size, family, and edge termination as control parameters for their performance can be considered as the first step toward the design of graphene-based applications in nano scale optoelectronics.

1. 5. 2 Issues with the use of NLO organic conjugated materials for OPL applications

Intensive fundamental research over the past thirty years has positioned organic NLO materials to make a technological impact in a variety of photonic applications. Particularly, for third-order NLO phenomena, the knowledge obtained from structure-property studies has resulted in a plethora of discrete molecule and polymer systems that possess strong, third-order NLO responses, as well as the requisite properties for desired applications. Therefore, the question remains as to why organic NLO materials have not played a more central role in photonics, particularly for commercialized photonic devices.

To discuss where the bottlenecks exist for organic NLO materials, we must first consider the desired application. Particularly for OPL, many optical and material properties must be optimized. This is especially true for NLO materials that exploit both instantaneous and accumulative processes for limiting. As previously mentioned, the effectiveness of accumulative NLO process for OPL depends on the rate of formation and decay of the excited states or free carriers. Should the dynamics of the absorbing states be significantly shorter than the duration of the laser-pulse, OPL will be ineffective. For example, if the excited-state lifetime of an NLO material is ~10-12 s [48], it will not serve as an effective limiter for nanosecond or microsecond laser pulses.

Organic materials offer the possibility of facile solution processing. However, conjugated molecules and polymers are known to exhibit strong intermolecular interactions due to their polarized π-systems, often referred to as π-π stacking. Due to π-π stacking and also due to potential solvation issues, many organic materials show a tendency to aggregate at high concentrations. Particularly strong aggregation due to non-covalent forces has been observed in conjugated polymers, resulting in supramolecule polymeric structures. These aggregation effects in conjugated organic systems can result in drastic changes in the linear and nonlinear optical properties of the material as well as and quenching of excited states [107], which may inevitably limit their usage in OPL.

The spectral coverage of limiters is becoming increasingly important as the wavelengths of commercially-available lasers can extend from the ultraviolet to the mid-IR spectral region.

Identifying OPL materials with accumulative nonlinearities that show high transparency >50% with broad and strong, excited-state absorption bands is difficult.

It has been deduced that FOMs [46] are required for the implementation of organic conjugated materials in commercially-viable OPL applications according to ANSI standards. These large FOMs have not yet been achieved in single element organic conjugated materials. For accumulative OPL materials, increased FOMs would require significant increases in excited-state absorptivities. For instantaneous OPL materials, increases in the third-order NLO response is needed to achieve such goals.

1.6 Charge transport in GNRs

In graphene nanoribbons (GNRs), the lateral confinement of charge carriers opens a band gap, the key feature to enable novel graphene-based electronics. In spite of the advantage of having

a band gap, the mobility in GNRs is reduced compared to its mother material [93, 112]. It is understandable within the framework that the narrower the structure is, the more the valence and conduction bands become parabolic: this decreases the curvature around the K point and increases the effective mass of the charge carriers, which is likely to decrease the mobility [113]. However, edge roughness can introduce extra back-scattering, thus degrade the mobility and conductivity even more severely, especially for sub-20 nm GNRs when the edge effect becomes more prominent. In a moderately disordered GNR, the electron mean free path (ℓ_e) is usually less than the width and the length of the GNR. In this case, impurity scattering is of greater importance and the electron motion remains diffusive along the channel, where the conductance scale is proportional with the width and inversely with the length. This transport regime is called the diffusive regime [114]. In etched GNRs, the edge disorder reduces the ℓ_e to less than 5 nm [115]. The edge defects also scatter electrons into all sub bands equally, giving rise to a strong suppression of the conductance at high energy where more sub bands are available. GNRs obtained from unzipping multi-walled carbon nanotubes (MWCNTs) [116] have been demonstrated to have ultra-smooth edges, higher mobility, and longer electron mean free path. In this regime, one would expect much less scattering along the channel direction. Also, the conductance formula shifts from Ohm's law in the diffusive regime to the Landauer formula in the quasi-ballistic regime and the ballistic regime. The fact that GNR enters the quasi-ballistic regime is of great importance, because it signifies its potential to be used not only in modern high speed electronics but also in quantum devices. GNRs made by sonication unzipping carbon nanotubes have been demonstrated to exhibit signatures of intrinsic quantum-confined band gaps and quasi-ballistic transport, making them feasible for both fundamental research and electronic applications. Recently, Baringhaus, reported ballistic transport over a remarkably long distance in epitaxial GNR on SiC [115]. Using density functional theory combined with coherent quantum transport models, the transport properties of GNRs are predicted to strongly depend on the geometry of the reconstructed edge profile and local defect chemical reactivity. The effect of single edge defects ranges from a full suppression of either hole or electron conduction to a vanishing contribution of backscattering. Besides, hydrogenation, chemically active defects is found to globally restore electron and hole conduction. Finally, owing to the derivation of a suited tight binding model, mesoscopic transport calculations of disordered ribbons with lengths up to several micrometers are achieved, and conduction is found to change from metallic to insulating regime depending on the geometry and density of edge defects up to several micrometers are achieved.

Modeling the charge carrier transport in the networks reveals that this process is governed by inter-ribbon hopping mediated by nuclear tunneling, with a hopping length comparable to the physical length of the GNRs. Furthermore, it is shown that nuclear tunneling is a general charge transport characteristic of the GNR networks by using two different GNRs. Overcoming the challenge of low-yield single-ribbon transistors by the networks and identifying the corresponding charge transport mechanism puts GNR-based electronics in a new perspective. Field-effect transistors (FETs) based on two-dimensional materials have attracted immense interest as potential next generation of electronics with exceptional properties, such as mechanical flexibility and optical transparency. Various novel two–dimensional materials have recently become available, and among them, graphene plays a unique role due to its extremely high charge carrier mobility [117]. While graphene itself does not have a band gap, a prerequisite for many semiconductor applications, geometrical confinement to one dimension, as occurring in graphene nanoribbons (GNRs), allows for the modification of the electronic structure, and a band gap opening [118, 119]. High-quality GNR films are produced by the use of the chemical vapor deposition (CVD) method which are scalable and cost-effective [120], such ribbons with armchair edges and a width of five carbon atoms (5-AGNRs) are particularly interesting for charge transport because they exhibit a particularly low band gap, as predicted theoretically and confirmed spectroscopically [121, 122]. Furthermore, photoconductivity measurements on 5-AGNRs indicate very high mobility of charge carriers in these nanoribbons [123]. Despite the evident promise in the study of GNRs most importantly, many of the fundamental charge transport mechanisms of GNRs have so far remained unclear. Up to now, most device studies on bottom-up GNRs have aimed at observing charge transport through single ribbons, employing short-channel FETs [124, 125]. While these devices show promise for nano-electronics applications, they are typically highly resistive, which has been attributed to large energy barriers at the contacts for charge injection [125].

1.7 Photovoltaic properties in organic materials and GNRs

1.7.1 Organic photovoltaic

When the global warming and depletion of common energy supplies, such as fossil fuels started threatening the balance of human life, great attention was driven towards the renewable (alternative) energy sources. Among number of alternative sources, such as wind energy, hydroelectric energy, biomass and geothermal energy, solar energy has the highest amount of potential availability on earth. Renewables are expected to account for 90% of total global capacity increases in both 2021 and 2022, according the International Energy Agency (IEA)'s

[126]. An additional 270GW capacity of renewable energy is expected to become operational this year, with a further 280GW in 2022 [126], surpassing the previous record-level annual capacity additions of 2017-2019 by more than 50%. Although new wind capacity is expected to decrease in 2021-2022 following significant expansions in China last year, capacity is still expected to be 35% higher than in 2019, with 80GW of annual installations anticipated globally. The slower rate of wind capacity additions will be partly offset by increased solar photovoltaic (PV) rollout, on lower investment costs and ongoing policy support. Net renewable capacity by technology for 2020-2022 by IEA is shown in fig 1.2 below

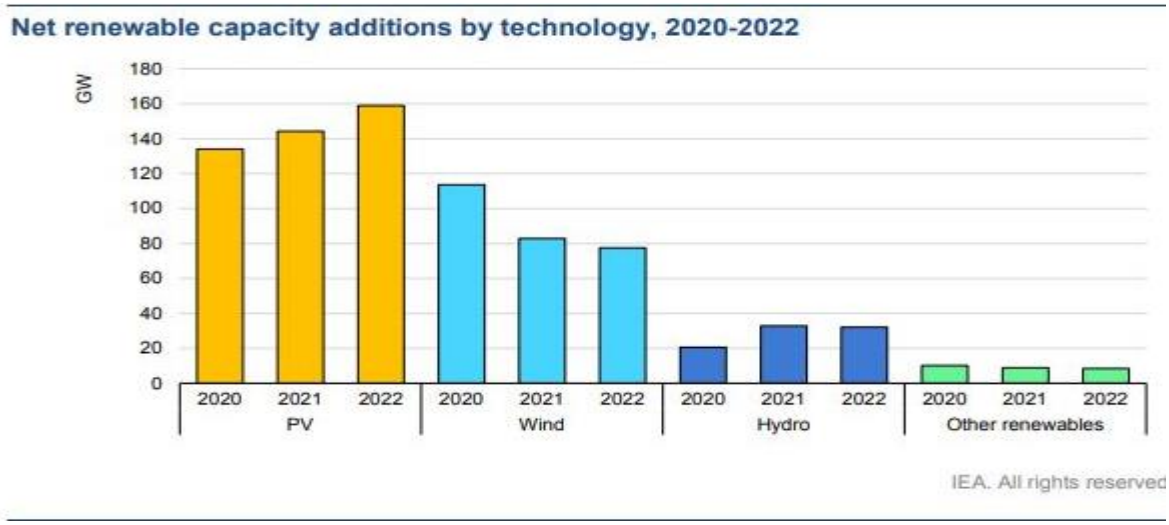

Fig 1.2 Net renewable capacity by technology for 2020-2022 by IEA [126]

A very small fraction of sun power (less than 0.02 %) reaching the earth surface can cover the whole energy demand of the world. There are various solar technologies for harvesting the sun energy, which can be divided to two categories: passive solar and active solar. An example of passive technique can be the designing of a building in such a way that it efficiently harvests and stores the sun energy in the building. Active solar technologies are the solar thermal collectors or photovoltaic (PV) devices. However, the fastest and most efficient direct conversion of sun light into electrical energy is possible only through photovoltaic devices. The photovoltaic (PV) effect discovered by Becquerel [127] is the basic physical process, by which a semiconductor material converts electromagnetic radiation (sun light) into electric power.

While our environment is surrounded with abundant solar power, the PV technology is still too expensive to become a primary energy source. Therefore, the main task of the solar cell field is to develop a technology, which can provide cheap PV products and make the

photoconversion of sun light into electrical power cost efficient. Global demand for energy is steadily increasing, consequently the total world energy demand use will surge at a typical annual rate of 1.8% to reach 18.49 TW in 2030 [126]. The usage of environmental friendly eco material, is of critical concern in the assembly of systems for renewable energy applications. Incidentally, the search for organic photovoltaic (OPV) molecules for solar cells technological implementation, has become a subject of passionate research in the last years. The task of acquiring new renewable energy sources to fill the energy gap is daring with photovoltaic solar energy being a promising research avenue to fill the energy deficit. Nevertheless, harnessing solar energy into electrical energy at low cost is no easy job. By 2019, the world record for solar cell efficiency developed by National Renewable Energy Laboratory, Golden, Colorado, USA stood at 47.1% realized with the use of multijunction concentrator solar cells [128, 129]. Photovoltaic solar cells produced from inorganic matter, such as silicon have some limitation in terms of scarcity, toxicity, unconstrained resource storage, expensiveness and unmodifiable energy levels [130]. Faced with such limitation, attention is now directed to polymer or organic photovoltaic cells (OPVCs) due to the numerous virtues of organic material over their inorganic counterpart in mechanical flexibility, modifiable energy level, environmentally friendliness and low cost. Moreover, there exist immeasurable variety of organic molecules to choose from, for design purposes with very great tunable and optical absorption. GNRs being an organic molecule is not left out of such current research. However, OPVCs possess a disapproving low power conversion efficiency (PCE) than inorganic photovoltaic cells, ensuing from their large band gaps [20,130-133]. Besides having a low efficiency, OPVCs have low strength and stability and are more prone to water and oxygen attacks [134]. Accordingly, it remains a great challenge to achieve high performant OPVCs for practical purposes. Despite tremendous efforts put in the research of OPVCs they still lag far behind those of their inorganic counterparts in the power conversion efficiency (PCE). To study OPVCs technology a glance is first taken into conventional inorganic silicon based PVCs and the three type of OPVCs.

1.7.2 Silicon-based Photovoltaic Solar Cell Mechanisms

Semiconductor materials can either be inorganic compounds (such as silicon) or organic compounds. Photovoltaic cells based on inorganic compounds presently have efficiency between 12 – 25% [126] while photovoltaic cells based on organic compounds have efficiency in the region of 12% [126, 134]. The solar cell market is still dominated by silicon-based photovoltaic technology because of the abundant supply of silicon as raw material and the established technology. The silicon technology has been well developed before the advent of

photovoltaics and high quality material was already being produced for the use in transistors and integrated circuit. The first silicon solar cell was reported by Bell Laboratories in 1954 with a power conversion efficiency of 6% [129]. Significant progress in the silicon-based solar cell industry has contributed in no small measure to the current power conversion efficiency that stands at a maximum of ~ 25% [130]. When light with appropriate energy is incident on silicon, electrons are promoted from the valence band into the conduction band. The valence band is the region with the highest probability of finding electrons and it is located below the conduction band. On the other hand, the conduction band is the region that an electron that is already freed from the electron affinity of the valence bound is free to move to. Materials can be categorized by the amount of energy required to free electrons from the valence band to the conduction band known as the band gap. Figure 1.3 shows a schematic of the band structure of a typical semi-conductor material.

For metals, the conduction band and the valence band overlap and this is the reason why metals are very conductive. The band gap of a semi-conductor material is between that of a conductor and an insulator. Silicon is an example of a semi-conductor with an indirect band gap because the crystal momentum (k-vector) in the minimum energy state of the conduction band and the maximum energy state in the valence band are the different. In an indirect band gap material, an electron can only emit a photon through an intermediate state. This has the implication of limitation of absorption in silicon-based materials because light has to penetrate the silicon materials much farther before being absorbed. Consequently, it requires more materials to make silicon-based solar cells as light absorption cannot effectively take place over thin active layer. The weak absorption of light in silicon-based material has implication on its cost from the material stand point. Silicon will require 100 μm of thickness to absorb 90% of incident light compared to 1 μm GaAs which is a direct band gap material.

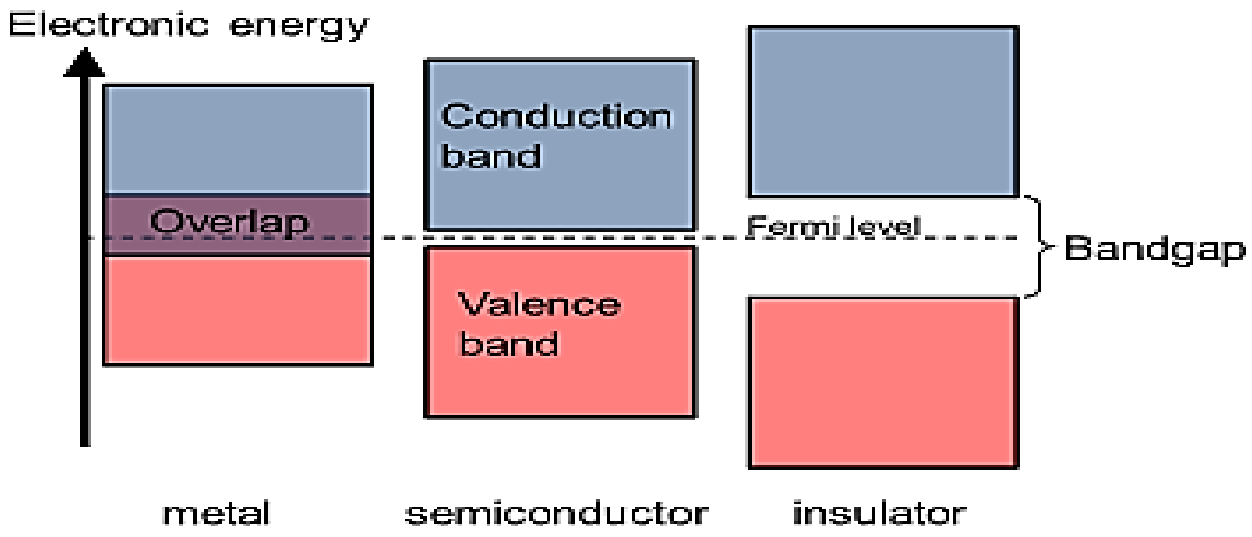

Fig 1.3 Schematic of the band structure of a typical semiconductor compared to metal and insulator

High purity silicon crystals are usually required to manufacture solar cells. Silicon atoms have four electrons in its outermost electrons and the electrons are locked in the valence band. Pure silicon can be doped by 'impurities' (dopant) to modulate its electrical properties and therefore make it conductive. Charge carriers can be introduced into the lattice of silicon by introducing suitable extrinsic materials. The charge carriers can either be electrons or holes. Group III and V elements are usually used as dopants. When group III elements (such as boron) having three electrons in their valence bands are used as dopants, p-type of semiconductor having excess holes is produced. Alternatively, when group V elements having five electrons (such as phosphorus) in their valence bands are used as dopants, n-type of semiconductor having excess electrons are produced. When a p-type semiconductor is placed near an n-type semiconductor, a p-n junction is produced. Light of adequate intensity and energy can generate a free electron which is attracted to the n-region of the p-n semiconductor through the p-n junction. This creates an imbalance of charge between the n-type semiconductor and the p-type semiconductor. The imbalance in charge promotes the flow of electrons from the n-type semiconductor to an external load thereby generating electricity.

Crystalline silicon still dominates the silicon solar cell market but there have been tremendous progress in the thin-film materials which require only small amounts of material. In the emerging markets of thin-film materials are amorphous silicon, cadmium telluride, copper indium gallium diselenide and organic polymers.

1.8.1 Organic Photovoltaic

There are basically three types of organic photovoltaics, namely: polymer solar cell, Perovskite solar cells and Dye sensitized solar cell (DSSC). In this work, will duel on polymer solar cell

1.8.2 Device Architecture and Operational Mechanism of polymer OPV

The main criterion that distinguishes the working principle of the organic PVs from inorganic PVs is that upon absorption of a photon by inorganic material free charge carriers are created, while in the case of organic material an excited pair or so-called “exciton” is generated, from which charge carriers still need to be dissociated [135].

The mechanism by which the light is converted to electric power in OPVs consists of 4 basic steps as shown in fig 1.4.

(1) The photon is absorbed by the active material, which promotes the electron to the lowest unoccupied molecular orbital (LUMO), while leaving the positive charge carrier or so called “hole” in the highest occupied molecular orbital (HOMO). The exited pair is still bounded by coulomb attraction forces forming an exciton.
(2) The exciton diffuses to the interface of the donor and acceptor.
(3) The exciton is dissociated into free carriers at the interface between donor and acceptor.
(4) Finally, the free carriers are being transported and collected at the opposite electrodes.

Each of the steps is crucial for the efficient power generation and there are many loss mechanisms involved in this sequence. The terms donor and acceptor refer to materials with either high ionization potential (donor) or high electron affinity (acceptor). The free charge collection at opposite electrodes is assured by the asymmetric ionization energy or work function of the electrodes.

An important parameter of the absorbing material is its optical band gap, which is defined by the difference of HOMO and LUMO. One of the main losses in the efficiency of OPVs is the poor matching of the absorption spectrum of the polymer with the solar emission spectrum. As an example, the band gap of commonly used poly(3-hexylthiophene) P3HT is around 1.9 eV, limiting the absorbance to wavelengths below 650 nm. Since the photon flux reaching the surface of earth from the sun has a maximum of approximately 1.8 eV (700 nm) P3HT is only able to harvest up to 22.4% of the available solar photons [136, 137].

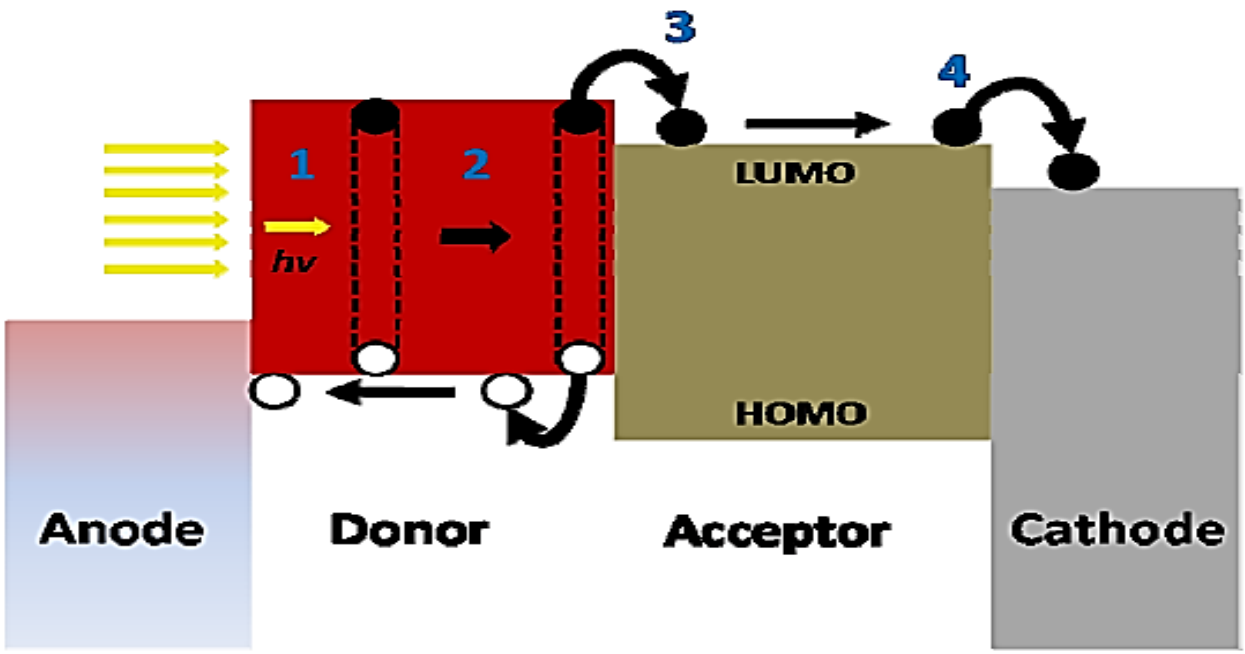

Fig. 1.4 Schematic illustration of the photoelectric conversion mechanism [136]

In order to increase the efficiency of OPVs to their optimal value the band gap of the polymer has to be tuned to the light spectrum in the way that it collects the highest number of photons possible. While tuning the band gap one has to take into account also the alignment of the bands of donor and acceptor to ensure charge separation. The offset of LUMO levels between the two materials needs to be at least few hundred MeV in order to efficiently separate the excitons to free carriers [138]. Often this offset is called exciton binding energy. The voltage of the device is theoretically defined by the difference of donor HOMO and acceptor LUMO, while the number of absorbed photons and consequently the current is defined by the lowest band gap of two materials. A commonly used derivative of fullerene C60, phenyl-C61-butyric acid methyl ester (PCBM) is the most widely used acceptor.

The common structure of the organic solar cells is comprised of a stack of layers. Usually the active layer which is a combination of donor and acceptor materials is sandwiched between two electrodes. One of the electrodes needs to be transparent for illumination of the cell. In some cases, certain buffer layers are being applied between the electrodes and the active layer to ensure charge selective transport. Figure 1.5 shows typical device architecture for OPVs. Excitons have a very short life time and the distance they can cross before recombination (Diffusion length) in several different conjugated polymers has subsequently been measured to

be 4 – 20 nm [139]. Therefore, after the generation of an exciton it has to be separated to free charges very fast before recombination takes place.

The active layer can be designed in three different ways as shown on the right-hand side of Figure 1.5. It can be 1) a single layer, 2) double layer (bilayer heterojunction) or 3) bulk heterojunction (mixture of donor and acceptor in a bulk). The first OPVs were based on a single layer structure, where the excitons are separated into free charges at the interface between the active layer and the electrode. The separation of charges however is very inefficient in this concept. The efficiencies severely increased after the introduction of donor/acceptor bilayer structure, where the donor and acceptor layers are brought together forming a heterojunction. However, only the excitons generated within the distance of the diffusion length from the interface can successfully diffuse to the interface and be separated to free carriers. Therefore, only the light absorbed by a very thin layer next to the interface can contribute to the photocurrent, while the rest is lost due to recombination processes. For that reason the photocurrent delivered by these devices is quite low. The breakthrough came with the idea of bulk heterojunction, where the donor and acceptor materials are mixed in a bulk forming nanoscale morphology [140]. In that way the interface is distributed throughout the whole active layer providing more efficient charge separation.

The solar cell in the dark acts as a simple diode. The equal electric circuit that approximates the organic solar cell performance is shown in Figure 1.6. It is comprised of: (1) a diode with ideality factor n and saturation current I_0 (current in the dark at the reverse bias), (2) a source to provide current that corresponds to photocurrent I_L generated during illumination, (3) R_s series resistance, which takes into account all the resistance at interfaces in the layers, the conductivity of the semiconductors and the electrodes and (4) Shunt resistance R_{sh}, which takes into account the leakage of the current through the shunts due to the defects in the films. For good performance of the device R_s needs to be low and R_{sh} has to have high values.

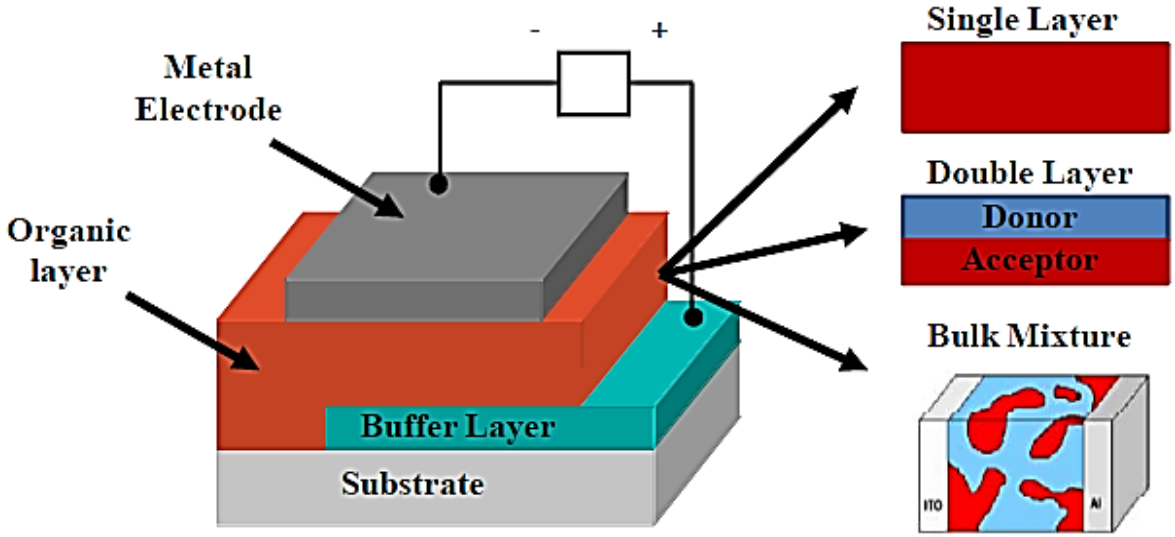

Fig 1.5 Device structure of a polymer solar cell. Three different designs of active layer are shown on the right hand side [136].

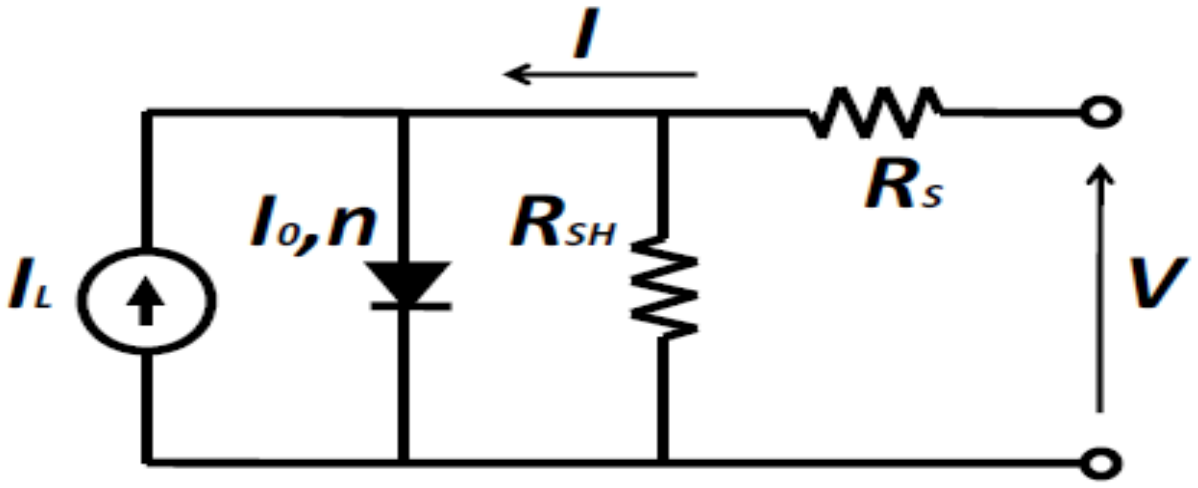

Fig. 1.6: Electric circuit that approximates the operation principle of OPV device

Figure 1.7 shows the current voltage characteristics (IV curves) for a typical solar cell. When light is shined on the device the IV curve of the cell becomes a superposition of the dark IV with the light generated current and the curve is shifted down to the 4th quadrant. The right hand side of Figure 1.5 presents the 4th quadrant of the IV curve, which shows the part where the actual power is being produced by the cell during the illumination. The figure also shows the key parameters that define the performance of the cell, which are the open circuit voltage V_{oc}, short circuit current I_{sc}, fill factor FF, the maximum power P_{max}, the voltage and the current at max power point V_{max} and I_{max}.

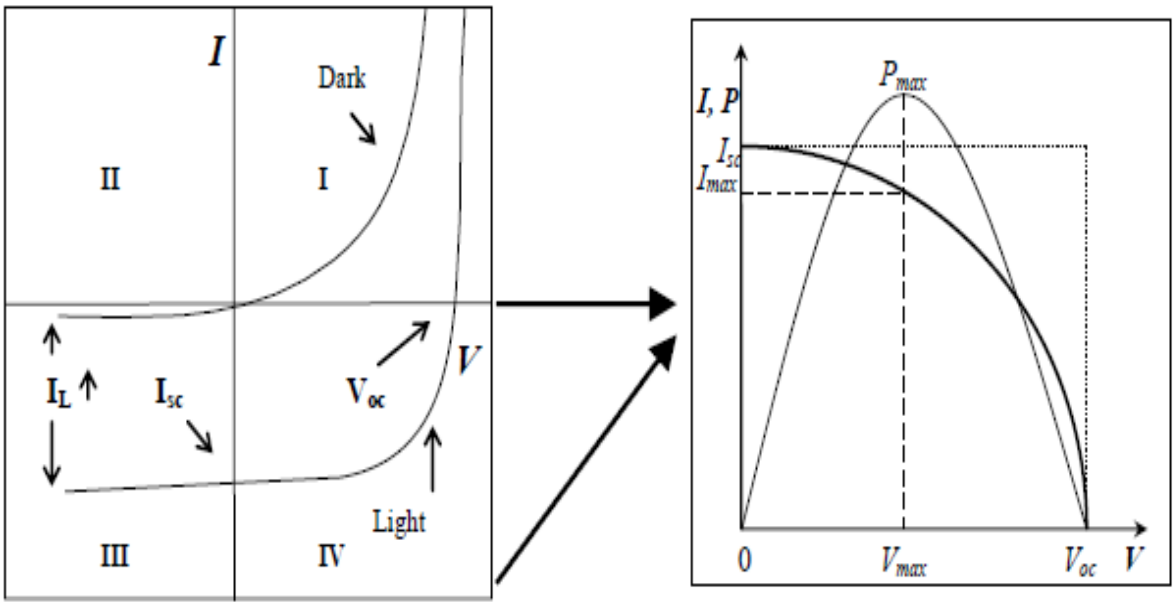

Fig. 1.7: Dark and light IV characteristics of OPV device (left) and the inverted and enlarged 4th quadrant with additional power curve (right).

The following expression defines the current for the circuit

$$I = I_0\left(\exp\left[\frac{e(V-IR_s)}{nkT}\right]-1\right)+\frac{V-IR_s}{R_{sh}}-I_L \qquad 1.5$$

where e is the elementary charge, kT the thermal energy. From this equation V_{oc} and I_{sc} can be obtained by placing 0 values for I and V respectively. For the approximation on right hand side of the equations below it is considered that R_s is very small and R_{sh} is very big

$$I_{sc} = I_0\left(\exp\left[\frac{eI_{sc}R_s}{nkT}\right]-1\right)-\frac{I_{sc}R_s}{R_{sh}}-I_L \qquad 1.6$$

$$V_{oc} = \frac{nkT}{e}\ln\left[1+\frac{I_L}{I_0}\left(1-\frac{V_{oc}}{I_L R_{sh}}\right)\right] \approx \frac{nkT}{e}\ln\left[1+\frac{I_L}{I_0}\right] \qquad 1.7$$

The power of the energy produced by the solar cell is defined by the product of the current and voltage and the maximum power will correspond to the maximum product of $I_{max}\times V_{max}$. Equation 1.7 below is the basic equation that defines the power conversion efficiency (PCE) η of the solar cell, which shows the ratio between maximum electric power produced by the cell and the power of the incident light on the cell with given active area of A

$$\eta = \frac{I_{max}V_{max}}{P_{in}A} = FF\frac{I_{sc}V_{oc}}{P_{in}A} \qquad 1.8$$

where FF is the fill factor

$$FF = \frac{I_{max}V_{max}}{I_{sc}V_{oc}} \quad 1.9$$

Fill Factor FF is a relative measure of how much power is produced by the cell with given I_{sc} and V_{oc} in practice compared to the theoretically possible value. FF is significantly affected by parasitic resistances R_s and R_{sh}. Typically, good operating organic solar cell delivers FF values in a range of 60 – 65 %.

Another important quantity that defines the quality of energy conversion is the quantum efficiency (QE) of a solar cell. QE defines the number of charge carriers collected at the electrodes per number of incident photons on the solar cell area at a given wavelength. If every incident photon results in one collected charge carrier then the QE is equal to unity (no recombination losses). There are two ways of defining the QE:

External Quantum Efficiency (EQE) or often called Incident Photon to Charge Carrier Efficiency (IPCE) is the ratio between number of collected carriers and number of all **incident** photons on the cell at a given wavelength. Internal Quantum Efficiency (IQE) is the ratio between number of collected carriers and number of all **absorbed** photons by the active layer of the device at a given wavelength (IQE does not take into consideration the light transmitted through and reflected from the cell as well as the light collected by the other layers that do not contribute in photoconversion process).

A comprehension of the energy loss mechanisms and its limitation arising from the optical excitation process in the OPVC, to the collection of charge at the electrodes ought to lead to greater efficiencies in the near future with single heterojunction. However, higher efficiencies could emanate from stacking of multiple cells [141, 142]. The interrelatedness between photo electronic properties and molecular structure can't be overemphasized, so reasonable structural modifications can effectively improve the PCEs of the device. By 2012, research had realized a PCE for the best performing OPVC of not more than 10% [143, 144].

1.8.3 Perovskite solar cells

Perovskite solar cell is one of the latest introductions to the thin film photovoltaic devices and they are low cost technology for the future. In these type of cells, methylammonium lead halide ($MAPbX_3$, X=halide) or mixed halides serve as the light harvesting layer which injects electrons to the conduction band of the semiconductor such as TiO_2. The layered assembly of the cell consists of a bottom TiO_2 blocking layer on a conducting FTO (fluorine-doped tinoxide) glass, the light harvesting MAPbX3 followed by the hole transport material (HTM)

such as PEDOT-PSS, Spiro-OMETAD or simple electron rich organic compounds in contact with an external transparent FTO glass or noble metal electrode [126] The block diagram and the energy level diagram for a typical perovskite cell is shown in Figure 1.8. Efficiency of over 12% has been achieved for these types of cells. The major disadvantage is the lack of long term stability and the use of toxic metal ions in the construction of these types of cells. The future research in this area is directed towards development of alternate perovskite light harvesting materials which is devoid of toxic metals, possessing long term stability and having higher efficiency

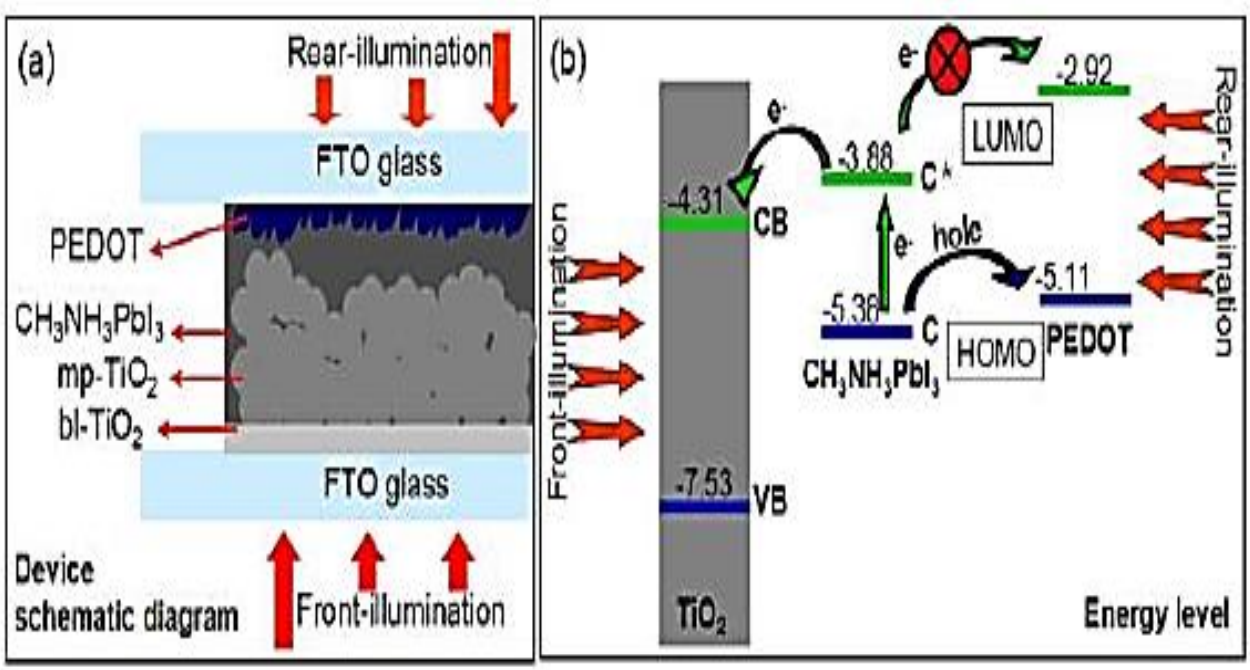

Fig 1.8 The schematic representation of perovskite cell [136]

1.8.4 Photoelectrochemical cells - Organic dye sensitized solar cells (DSSC)

Dye sensitized solar cells are devices which generate electricity via a photoelectrochemical reaction wherein, a light harvesting molecule gets oxidized in the presence of a semiconductor and subsequent regeneration of the dye by an electrolyte of appropriate redox potential. The first dye-sensitized solar cell was introduced in 1991, by Grätzel *et al*. with an efficiency of 7.1-7.9% (under simulated solar light) using nanocrystalline TiO_2 semiconductor coated with a trimeric Ruthenium complex as dye on a transparent conducting oxide layer along with a liquid redox electrolyte couple I-/I3-[137]

Dye-sensitized solar cells have attracted much attention in recent years due to their potential advantages of low cost, ease of production, flexibility, and transparency. Generally DSSC consists of a transparent conducting oxide, a mesoporous semiconductor, photosensitizer dyes which can absorb radiations in the UV-Visible region, a redox couple electrolyte and a counter electrode. The photosensitizer dye is a key component of the DSSC since it is the one which harvests sunlight. On illumination, the dye molecule get photo-excited, whereby an electron transition occurs from its highest occupied molecular orbital (HOMO) to the lowest unoccupied molecular orbital (LUMO). This excitation energy corresponds to the energy difference between HOMO and LUMO of the dye molecule. The electron in the excited state of the dye (LUMO) is then injected into conduction band (CB) of TiO_2. It is then transported through the semiconductor layer by diffusion, to reach the conducting layer, i.e., a transparent conducting oxide (TCO), such as, Fluorine doped Tin Oxide (FTO) on glass substrate. The regeneration of the oxidized dye molecule occurs due to a redox reaction taking place in electrolyte. Typically an electrolyte containing a redox couple such as I-/I3- is used. In such cases, the iodide ion donates an electron to the oxidized dye (S+) at anode. The oxidized species of the electrolyte, i.e., the triiodide in iodide-triiodide complex, is reduced to iodide at the cathode. The above processes go in a cycle and consequently current flows through the external circuit as long as light is incident on the cell. The schematic diagram illustrating the working principle of a DSSC is given in Figure 1.9.

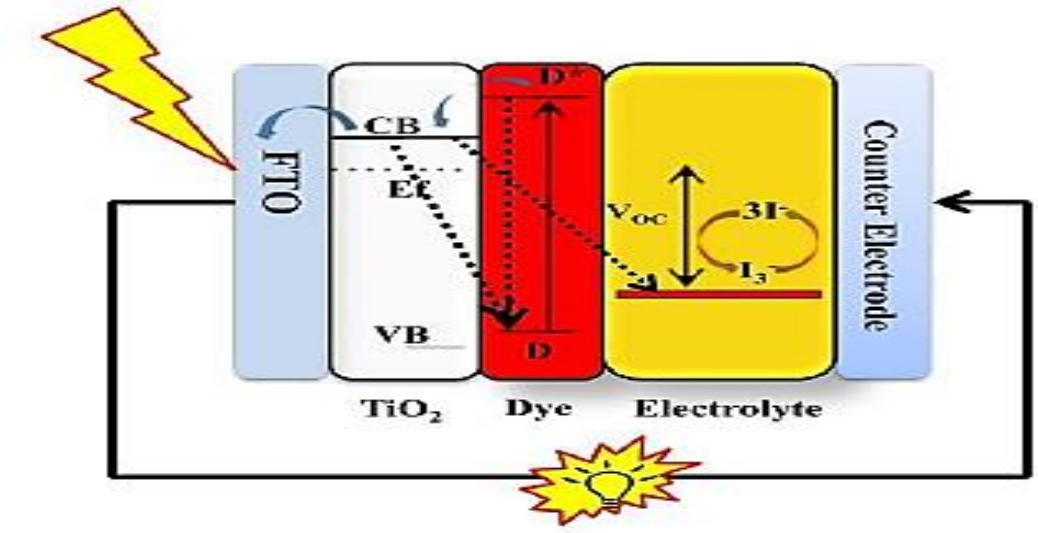

Fig 1.9 Schematic diagram illustrating the working principle of a DSSC [136]

1.8.5 Advances in GNRs photovoltaic

Compared to graphene, GNRs show distinctive features in their electronic structure and optical properties, such as the opening of a finite band gap (graphene being a zero overlap semimetal), which makes them attractive materials for carbon-based nanoelectronics [145, 146]. The geometrical arrangement of carbon atoms at the periphery, the passivation of the end carbon atoms with, for example, hydrogens, and the finite width of the GNRs strongly affect their electronic properties [111, 147]. These confinement effects yield an increased band gap in armchair edge nanoribbons (ANRs) that behave as semiconductors. A-GNRs feature band gaps that scale inversely proportional to the ribbon width and are highly sensitive to the number of armchair chains across the ribbon [148]. Nanoribbons with a higher fraction of zigzag edges exhibit a smaller band gap than a predominantly armchair edge ribbon of similar width. Finite widths combined with periphery effects also provide GNRs with peculiar optical properties. Another important feature pertaining to graphene ribbons is the existence of edge states, which play an important role in the optical absorption spectrum in the visible range [149]. Those peculiarities have raised the interest of scientists for the design, synthesis, and electrical characterization of GNRs. Because of their interesting optoelectronic properties and the possibility to tune their (optical) band gap through a proper design of their length, width, and edge structure, GNRs may be used as alternative to low band gap conjugated polymers (molecules) in bulk heterojunction organic solar cells. For this purpose, however, GNRs should fulfill two necessary requirements revolving around their one-electron energy diagram and optical response, respectively revolving around their one-electron energy diagram and optical response, respectively [150].

i. On the one hand, suitable GNR donors should yield type II heterojunction in combination with common electron acceptors such as C_{60} or its soluble derivatives. Namely, an energy offset of a few tenths of an electronvolt between the LUMO (HOMO) levels of the donor and acceptor materials is typically needed to favor electron transfer from the photoexcited donor to the ground-state acceptor while preventing the corresponding hole transfer; in addition, the energy difference between the donor HOMO and the acceptor LUMO should be as large as possible to maximize the open circuit voltage (V_{oc}) [138, 151]

ii. As light harvesting occurs primarily on the donor material in C_{60}-based organic solar cells, the GNRs should also feature strong optical absorption over the broad spectral range of the solar emission. In addition, the primary step in the dissociation process should involve a

coulombically bound charge-transfer state [152]. It is believed that local electric fields at the interface, as, for example, induced by interfacial dipoles associated with electronic polarization or charge-transfer effects, can potentially reduce the barrier height for full charge separation. Thus, the electronic structure at GNR acceptor interfaces is also key for efficient charge photogeneration.

iii. Lastly, low-lying triplet excited states might act as sinks for the photogenerated electron-hole pairs, which appears as an efficient competitive process in high V_{oc} material combinations, hence the need for donors with low singlet-triplet exchange energy [153].

When GNRs were applied as the hole transport layer (HTL) in OPV, this optimized device exhibits an efficiency of over 5%. In fact, in the presence of multiple layers of GNRs, the efficiency is significantly increased with a concomitant significant increase in the photocurrent, open-circuit voltage as well as the fill factor (FF), nearly destroying the performance. This effect was tested in a regular structure, where the regular OPV geometry is set up, in which the photons enter through a transparent anode and must travel through the hole transport layer to reach a photoactive layer. Single and double stacked hole transport layers were then used to evaluate their compatibility. The ability to serve as a HTL is very useful for regular OPVs, as any suitable pair will result in much higher photovoltaic performance [154]. OPVs with printed GNRs serving as the HTL is an encouraging architecture for realizing highly efficient OPVs

1.8 Tackling Performance Challenges in Organic Photovoltaics

Organic Photovoltaics (OPVs) based on Bulk Heterojunction (BHJ) blends are a mature technology. Having started their intensive development two decades ago, their low cost, processability and flexibility rapidly funneled the interest of the scientific community, searching for new solutions to expand solar photovoltaics market and promote sustainable development. However, their robust implementation is hampered by some issues, concerning the choice of the donor/acceptor materials, the device thermal/photo-stability, and, last but not least, their morphology. Indeed, the morphological profile of BHJs has a strong impact over charge generation, collection, and recombination processes; control over nano/microstructural morphology would be desirable, aiming at finely tuning the device performance and overcoming those previously mentioned critical issues. The employ of compatibilizers has emerged as a promising, economically sustainable, and widely applicable approach for the donor/acceptor interface (D/A-I) optimization. Thus, improvements in the global performance of the devices can be achieved without making use of more complex architectures. Even though

several materials have been deeply documented and reported as effective compatibilizing agents, scientific reports are quite fragmentary. Here we would like to offer a panoramic overview of the literature on compatibilizers, focusing on the progression documented in the last decade.

With the continuous efforts on the development of new organic materials and innovative device engineering, the PCE of OPV devices has been steadily improved up to 6.1%; however, this efficiency is still not sufficient to meet the realistic specifications for commercialization. The major obstacle for achieving high PCEis the mismatch of the absorption of photoactive materials to the terrestrial solar spectrum. In particular, the optical band gap of most photoactive organic materials is much larger than the maximum photon flux at 1.8 eV, wasting over 60% of the solar spectrum. Scharber et al. [138] had systematically studied the dependence of V_{oc} on the band gap and HOMO levels of 26 conjugated polymers and predicted the limited efficiency of bulk heterojunction OPV devices. It was found that PCE of 10% can theoretically be achieved for the PCBM-based polymeric OPV device, provided that the donor polymer must have a band gap <1.74 eV and a LUMO level < -3.92 eV, assuming that the FF and the average EQE remain equal to 0.65. Photovoltaic responses of small molecular-based OPV devices. This model infers that the maximum PCE as high as 12% is feasible for an optimized double heterostructure OPV device. However, its success relies on the development of new organic materials, in which the donor and acceptor materials should have optical band gap of 1.5 and 1.8 eV, respectively, and a large interface offset energy, that is, IP (donor) – EA (acceptor) = 1.1 eV. This suggests that new photoactive materials with low optical band gap are definitely needed to be developed.

With the growing demand on energy consumption, there is an urgent need for implementing more energy saving measures. Many nations have committed on their new policies to implement the ways for saving energy and promoting it. Particularly, solid-state organic devices, especially organic solar cells, is targeted as effective ways for reducing the energy consumption and developing renewable energy in the world. Because of ultra-low costs of organic materials, organic solar cells gaining acceptance as the new generation of solid-state lighting sources to replace and complement the incandescent bulbs and an alternative type of solar cells to dislodge or complement the traditional Si solar cell for electricity generation, respectively. Indeed, organic solar cells with high PCE of 6.1% have been achieved in the laboratory. With the continuous efforts on improving their lifetimes and reducing the manufacturing cost, organic solar cells have a very bright future to be used widely.

1.9 Conclusion

It is quite recent, there has been a large importance towards the study and realization of GNRs based on optical devices designed by appropriate tailoring of the electronic structure exploiting not only the electric field effect but also in other applied such as strain. In other word, the GNR has stimulated enormous outburst of both fields theoretic and experiment an investigation. Likewise, shed light on molecules with non-linearities optical component which have been extensively (interestingly) in recent years. While the focus of current research in explain of their potential applications such as various photonic technologies. On the other hand, organic molecules generally and GNR specially are play a significant role in exhibiting of them possess numerous attractive NLO characteristics This chapter was devoted to the literature review on GNRs, their NLO, charge transport and Photovoltaic properties, we saw that GNRs had a wide range of properties ranging from electrical, optical, and mechanical properties and ignited enormous interdisciplinary interest from the physics, chemistry, and materials science fields which enables it to have a wide range of applications especially in the field of optoelectronics and OPV. This justifies the current theoretical and experimental research on GNRs. We equally examined the synthesis and purification of GNRs. Equally of interest were the current applications of GNRs in the fields of physics, chemistry, and materials science fields with fascinating applications. A review was done on the NLO and charge transport properties of GNRs and it showcase several key properties that can address the emerging need of terahertz science and technology, and break through the many technological limits on conventional semiconductor electronics operating in the terahertz spectrum. The OPV properties of GNRs were reviewed together with the general mode of functioning of organic PV and it was concluded GNRs serving as the HTL is an encouraging architecture for realizing highly efficient OPVs. From all these finding we therefore conclude that a profound research on how the effect of metalation can affect the already advanced NLO, charge transport and OPV properties of GNRs is of vital importance.

CHAPTER 2
MATERIAL AND METHOD

2.0 Introduction

Today, with the development of advanced numerical methods and high-performance computers, it is possible to theoretically determine many properties (physico-chemical, thermodynamic, electronic, nonlinear, etc) of classical molecular systems and of nano-dimension. Knowledge of the structure of molecular edifices makes it possible to understand and also to predict what is achieved in a physical, chemical or biological transformation. Both understanding and forecasting are greatly facilitated when we can visualize the structures. Modeling a molecule consists of specifying, from calculations, the position of the atoms that constitute it in space and calculating the energy of the structure thus generated. A representation "as close as possible to reality" will correspond to a structure of lower energy. There are two main classes of molecular computation modeling, namely: quantum mechanics and molecular mechanics. The choice of one of these molecular modeling calculation methods depends on the problem studied (degree of freedom of the system and desired calculation precision), the properties sought and obviously the calculation resources (computer power). Density Functional Theory (DFT) is a quantum computation method allowing the study of electronic structure exactly, in principle. Today, it is one of the most widely used methods in quantum calculations in condensed matter physics due to its possible application to systems of a wide variety of sizes, ranging from a few atoms to several hundred. The results of molecular simulations can be compared with experimental results from the same or similar systems to validate the modeled structures and predict other properties.

In this chapter, we present only the modeling methods based on quantum mechanics (ab-initio and DFT methods), also called *electronic structural methods*. In this regard, we shall be solving the Schrodinger's equation in order to determine the electronic properties of our molecules.

2.1 The Schrödinger equation

Ever since the birth of quantum mechanics, the rationalization of the properties of systems by solving the Schrödinger equation has been a major preoccupation of physicist. The essence of quantum mechanics is the computation of observables such as structures, energies, spectroscopic parameters and so forth that can be directly linked to experiments, so that theory

and experiment can complement each other. However, the Schrödinger equation cannot actually be solved for any but a one-electron system such as the hydrogen atom, and approximations need to be made. Finding approximate solutions to the non-relativistic time-independent Schrödinger equation **(2.1)** [155] for a many-electron system is the ultimate goal of electronic structure theory.

$$\hat{H}\Psi(\boldsymbol{r},\boldsymbol{R}) = E\Psi(\boldsymbol{r},\boldsymbol{R}) \qquad 2.1$$

Here, $\hat{H}$ is the Hamiltonian operator that describes the kinetic and potential energies of the electrons and nuclei within the many-electron system in the absence of a magnetic or an electric field. $\Psi(\boldsymbol{r},\boldsymbol{R})$ is the wave function of the system, wherein the electronic and nuclear coordinates are described by the position vectors $\boldsymbol{r}$ and $\boldsymbol{R}$ respectively, and E is the energy of the system. In atomic units, the Hamiltonian operator for a molecular system comprising M nuclei and N electrons is given by:

$$\hat{H} = -\frac{1}{2}\sum_{i=1}^{N}\nabla_i^2 - \frac{1}{2}\sum_{A=1}^{M}\frac{1}{M_A}\nabla_A^2 - \sum_{i=1}^{N}\sum_{A=1}^{M}\frac{Z_A}{\boldsymbol{r}_{iA}} + \sum_{i=1}^{N}\sum_{j>i}^{N}\frac{1}{\boldsymbol{r}_{ij}} + \sum_{A=1}^{M}\sum_{B>A}^{M}\frac{Z_A Z_B}{\boldsymbol{R}_{AB}} \qquad 2.2$$

where i and j refer to the N electrons, A and B denote the M nuclei, Z_A and Z_B are the atomic numbers of nucleus A and nucleus B respectively, and M_A is the mass of nucleus A. The distance between the ith electron and the Ath nucleus is $\mathbf{r}_{iA}$, the distance between the ith electron and the jth electron is $\mathbf{r}_{ij}$, and the distance between the A_{th} nucleus and the Bth nucleus is $\boldsymbol{R}_{AB}$. The first two terms of the Hamiltonian operator $\hat{H}$ describe the kinetic energies of the electrons (T_e) and nuclei (T_n) respectively, where the Laplacian operator ∇^2 is defined as:

$$\nabla^2 = \frac{\partial^2}{\partial x^2} + \frac{\partial^2}{\partial y^2} + \frac{\partial^2}{\partial z^2} \qquad 2.3$$

The third term of the operator $\hat{H}$ represents the coulombic attraction between electrons and nuclei (V_{ne}), while the fourth and fifth terms respectively represent the repulsive potential energy among the electrons (V_{ee}), and among the nuclei (V_{nn}) of the system. Hence $\hat{H} = T_e+T_n+V_{ne}+V_{ee}+V_{nn}$, but other terms are required in the Hamiltonian operator in the presence of an external electric or magnetic field, and in the event where spin-orbit coupling and scalar relativistic effects are to be taken into consideration when dealing with the heavy elements such as transition metals

Although **Equation (2.2)** cannot be solved exactly even for a simple two-electron system such as the Helium atom or the Hydrogen molecule, various approximations have been proposed over the past decades to render this equation solvable, at least approximately. The primary approximation (proposed by Born and Oppenheimer [155] basically neglects the coupling between nuclear and electronic motion

2.1.1 Born-Oppenheimer approximation

The Born-Oppenheimer approximation forms the basis of almost all electronic structure calculations. It greatly simplifies the Schrödinger equation by assuming that the nuclei in a molecule do not move, since they are much heavier than the electrons and thus move very slowly compared to the speed at which electrons move. Based on this approximation, the kinetic energy of the nuclei is assumed to be zero (i.e., $T_n \approx 0$) and the potential energy due to nucleus-nucleus repulsion (V_{nn}) is treated merely as a constant. Hence, the complete Hamiltonian operator in **Equation (2.2)** reduces to the so-called *electronic Hamiltonian* $\widehat{H}_e$

$$\widehat{H}_e = -\frac{1}{2}\sum_{i=1}^{N}\nabla_i^2 - -\sum_{i=1}^{N}\sum_{A=1}^{M}\frac{Z_A}{\boldsymbol{r}_{iA}} + \sum_{i=1}^{N}\sum_{j>i}^{N}\frac{1}{\boldsymbol{r}_{ij}} = T_{ee} + V_{ne} + V_{ee} \qquad 2.4$$

The Born-Oppenheimer approximation therefore leads to an electronic Schrödinger equation **(2.5)**, the solution of which comprises the electronic wavefunction $\psi_e(\boldsymbol{r}, \boldsymbol{R})$ and the electronic energy E_e. Note that $\psi_e(\boldsymbol{r}, \boldsymbol{R})$ contains a lot of useful information about molecular properties, such as dipole (and multipole) moments, polarizability, etc

$$\widehat{H}_e\psi_e(\boldsymbol{r}, \boldsymbol{R}) = E_e\psi_e(\boldsymbol{r}, \boldsymbol{R}) \qquad 2.5$$

The wavefunction $\psi_e(\boldsymbol{r}, \boldsymbol{R})$ describes electronic motion as fully as possible, since it is dependent on the electron coordinates **r**. Here, the nuclear coordinates **R** are parameters (not variables). The total energy of the molecule E_{tot} is then the sum of the electronic energy E_e and the constant nuclear repulsion term V_{nn}**.**

$$E_{tot} = E_e + \sum_{A=1}^{M}\sum_{B>A}^{M}\frac{Z_A Z_B}{\boldsymbol{R}_{AB}} \qquad 2.6$$

The Born-Oppenheimer approximation allows the electronic Schrödinger equation to be solved at different nuclear positions as parameters, and the resulting potential energies can be plotted against nuclear coordinates to obtain a Potential Energy Surface (PES) [155]. The PES is therefore, a function of the energy of a molecule in terms of the geometric coordinates of its atoms, from which the molecule's equilibrium or most stable geometry (that which corresponds to the lowest energy), and vibrational frequencies can be obtained.

Based on the Born-Oppenheimer approximation, attention herein will be solely focused on the electronic Hamiltonian operator and the electronic wavefunction, unless otherwise stated. For the sake of convenience, **R** that represents nuclear coordinates and the subscript "e" that indicates electronic parameters will be dropped.

2.1.2 Variation principle

In order to solve the Schrödinger equation **(2.2)** for a many-electron molecule, the first step is to set up the specific Hamiltonian operator $\widehat{H}$ of the target system. The second step is to obtain the eigenfunctions $\psi_i(\boldsymbol{r})$ and the corresponding eigenvalues E_i of $\widehat{H}$ for the ith state of the system. With the molecular wave functions $\psi_i(\boldsymbol{r})$ in hand, all physical observables (physical properties) of interest can then be obtained by the application of the appropriate quantum mechanical operators. Lamentably, no strategy for obtaining the set of molecular wave functions $\psi_i(\boldsymbol{r})$ by directly solving the Schrödinger equation **(2.2)** is exactly known. Nevertheless, the ground-state wave function $\psi_0(\boldsymbol{r})$ and the ground-state energy E_0 can be estimated by applying the variation principle.

The variation principle is an approximation method for solving the Schrödinger equation that provides approximations to $\psi_0(\boldsymbol{r})$ and E_0 of a many-electron system [156]. In many applications of quantum mechanics to chemical systems, knowledge of the ground-state energy is sufficient. From standard quantum mechanics, the expectation value of the energy of a system described by an acceptable and normalized function $\psi(\boldsymbol{r})$ is given by Equation **(2.7)**.

$$E = \int \psi^*(\boldsymbol{r})\widehat{H}\psi(\boldsymbol{r})d\tau = \langle \psi(\boldsymbol{r}) \left| \widehat{H} \right| \psi(\boldsymbol{r}) \rangle \qquad 2.7$$

$\psi^*(\boldsymbol{r})$ is the complex conjugate of $\psi(\boldsymbol{r})$. The second notation is so called Dirac notation and will be predominantly used in this presentation. The variation principle states that the energy computed from a trial normalized wave function $\psi_{\text{trial}}(\mathbf{r})$ is greater than or equal to the actual ground-state energy E_0 [157].

$$E = \langle \psi_{trial}(\boldsymbol{r}) \left| \widehat{H} \right| \psi_{trial}(\boldsymbol{r}) \rangle \geq E_0 \qquad 2.8$$

The equality can only hold if $\psi_{\text{trial}}(\mathbf{r})$ is identical to $\psi_0(\mathbf{r})$. By applying the variation principle, a set of approximate wave functions to $\psi_0(\mathbf{r})$ can be obtained by minimizing the energy of the system such that $E \geq E_0$.

2.1.3 The Hartree–Fock method

The electronic Schrödinger equation that results from the time-independent Schrödinger equation after invoking the Born-Oppenheimer approximation is still intractable and further approximations are required. The Hartree–Fock (HF) method is the starting point of such approximations. Indeed, the HF method is the corner stone of nearly all conventional wave function-based quantum mechanical methods. For a many-electron system, the HF method advances that the motion of each electron can be described by a one-electron function (an orbital), and that each electron's motion does not depend explicitly on the instantaneous motions of the other electrons. It is impossible to solve the electronic Schrödinger equation **(2.5)** by searching through all acceptable *N*-electron wave functions. To overcome this difficulty, the HF method approximates the overall *N*-electron wave function for a many-electron system by an *antisymmetrized* product of N one-electron functions called spin-orbitals [157]. A spin-orbital, $\mathcal{X}_i$ is the product of a spatial-orbital $\emptyset(\mathbf{r})$ and the α or β spin-function, i.e., $\mathcal{X}_i = \emptyset(\mathbf{r})\ \alpha$ or $\mathcal{X}_i = \emptyset(\mathbf{r})\ \beta$. The spin-functions α and β are orthonormal, meaning that $\langle\alpha|\alpha\rangle = \langle\beta|\beta\rangle = 1$ and $\langle\alpha|\beta\rangle = \langle\beta|\alpha\rangle = 0$. Consequently, spin-orbitals are usually chosen to be orthonormal such that

$$\langle \mathcal{X}_i | \mathcal{X}_j \rangle = \delta_{ij}$$

$$\delta_{ij} = \begin{cases} 1 \text{ for i } = \text{ j} \\ 0 \text{ for i } \neq \text{ j} \end{cases} \qquad 2.9$$

where δ_{ij} is the Kronecker delta symbol

In an effort to approximate the *N*-electron wave function of a multiple-electron system in terms of one-electron functions, Hartree assumed that the electrons in the system are noninteracting, and then constructed the *N*-electron wave function as a product of *N* one-electron functions, which is known as a *Hartree product*, ψ_{HP}.

$$\psi_{HP}(\boldsymbol{r}_1, \boldsymbol{r}_2, \ldots \boldsymbol{r}_N) = \mathcal{X}_1(1)\mathcal{X}_2(2) \ldots \mathcal{X}_N(N) \qquad 2.10$$

The Hartree product is fairly convenient, but fails to satisfy the *antisymmetry principle*, which states that an electronic wave function must change sign with respect to interchange of any two

electron coordinates (since electrons are fermions, particles with half integer spin of 1/2). Therefore, the Hartree product is not *antisymmetrized* and consequently does not satisfy the *Pauli Exclusion Principle*, which states that no two electrons can occupy the same quantum state having the same values of all four quantum numbers. To guarantee the antisymmetric nature of a wave function, it should be constructed as a *Slater determinant* [158].

2.1.4 Slater Determinant

Generally, the HF method assumes that the *N*-electron wave function of a multiple-electron system can be approximated by a single Slater determinant. For a molecule with *N* electrons and *N* spin-orbitals, the Slater determinant (ψ_{SD}) is given by

$$\psi_{SD} = \frac{1}{\sqrt{N!}} \begin{vmatrix} \mathcal{X}_1(1) & \mathcal{X}_2(1) & \dots & \mathcal{X}_N(1) \\ \mathcal{X}_1(2) & \mathcal{X}_2(2) & \cdots & \mathcal{X}_N(2) \\ \vdots & \vdots & \ddots & \vdots \\ \mathcal{X}_1(N) & \mathcal{X}_2(N) & \cdots & \mathcal{X}_N(N) \end{vmatrix} \qquad 2.11$$

where $1/\sqrt{N!}$ is a normalization constant. In a Slater determinant, the spin-orbitals or the one-electron functions are along the columns, while the electron coordinates are along the rows. The Slater determinant is antisymmetric because interchanging the coordinates of any two electrons corresponds to interchanging two rows of the determinant, which results in a change of the determinant's sign which is a known property of determinants. If two columns of the Slater determinant are identical, implying that two electrons with same spin (identical fermions) simultaneously occupy the same spatial orbital, the determinant vanishes. This demonstrates that the Slater determinant satisfies the Pauli Exclusion Principle, which is a direct consequent of the antisymmetry requirement [158, 159].

The HF approach essentially replaces the *N*-electron wave function of a many-electron system with a single Slater determinant comprising *N* molecular orbitals (MOs) or spin-orbitals (a fairly drastic approximation), which allows each electron to be affected by the average field of all the other electrons. This leads to the main shortcoming of the HF method, which is that it treats electrons as if they were moving independently of each other, and each electron only experiences a coulomb repulsion due to the average field of all the other electrons; in other words, it neglects electron correlation [160]. Due to this drastic approximation, the HF method is known as the *independent electron* or *independent particle* approximation. The HF method begins with the selection of a single-determinant trial wave function of the target system. Then

the variation principle is applied, whereby the MOs or spin-orbitals $\mathcal{X}_i$ of the system are varied under the constraint that they remain orthonormal, so that the HF energy obtained is minimal

2.1.5 Hartree–Fock energy

Having known the form of the wave function used in the HF method, it is important to examine the Hamiltonian operator as well. A closed-shell molecule with 2*N* electrons and *M* nuclei will be considered here because the HF method works best with closed-shell systems (those containing an even number of electrons), since a single Slater determinant is usually sufficient to describe the molecular wave functions of such systems. The explicit electronic Hamiltonian operator for the system is given by **Equation (2.12)**

$$\hat{H} = -\frac{1}{2}\sum_{i=1}^{2N}\nabla_i^2 - \sum_{i=1}^{2N}\sum_{A=1}^{M}\frac{Z_A}{\boldsymbol{r}_{iA}} + \sum_{i=1}^{2N}\sum_{j>i}^{2N}\frac{1}{\boldsymbol{r}_{ij}} \qquad 2.12$$

Note here that the inter-nuclear repulsion potential energy term V_{nn} is omitted from this Hamiltonian operator as a consequence of the Born–Oppenheimer approximation. However, to obtain the total energy of the molecule, V_{nn} must be added to the calculated electronic energy. In the meantime, V_{nn} will be ignored, since it is a constant for a fixed set of nuclear coordinates, and thus only shifts the eigenvalues without changing the eigenfunctions. The explicit electronic Hamiltonian operator described by **Equation (2.12)** can be further split into a one-electron operator $\hat{h}$ and a two-electron operator $\hat{v}$, given by **equations (2.13)** and **(2.14)**, respectively

$$\hat{h}(i) = -\tfrac{1}{2}\nabla_i^2 - \textstyle\sum_A^M \frac{Z_A}{\boldsymbol{r}_{iA}} \qquad 2.13$$

$$\hat{v}(i,j) = \frac{1}{\boldsymbol{r}_{ij}} \qquad 2.14$$

Then, the explicit electronic Hamiltonian operator can be rewritten as

$$\hat{H} = \textstyle\sum_{i=1}^{2N}\hat{h}(i) + \sum_{i=1}^{2N}\sum_{j>i}^{2N}\hat{v}(i,j) \qquad 2.15$$

By applying the variation principle, the HF energy of the 2*N*-electron molecule with "frozen nuclei" is given by **Equation (2.16)**

$$E_{HF} = \int \psi_{SD}^{*}\, \hat{H} \psi_{SD} d\tau = 2\sum_{i=1}^{N} \langle i|\hat{h}|i\rangle + \sum_{i=1}^{N}\sum_{j=1}^{N} (2j_{ij} - K_{ij})$$

2.16

The sums represented by i and j run over the N occupied molecular orbitals ($\mathcal{X}_i$), and the integral is over all space ($d\tau$=$dxdydzd\xi$) i.e., with respect to the three spatial coordinates (x,y,z) and one spin coordinate (ξ) of each electron. The terms on the extreme right-hand side of **Equation (2.16)** have the following meanings.

The one-electron integrals $\langle i|\hat{h}|i\rangle$ define the kinetic energy of electron 1 plus the potential energy of attraction of this electron to each of the *M* nuclei represented by *A*

$$\langle i|\hat{h}|i\rangle = \int \mathcal{X}_i^{*}(1) - \left\{-\frac{1}{2}\nabla_1^2 - \sum_{A}^{M} \frac{Z_A}{\boldsymbol{r}_{iA}}\right\} \mathcal{X}_i(1) d\tau_1$$

2.17

The two-electron integrals represented by $\boldsymbol{J_{ij}}$ are called *Coulomb integrals*. They define the electrostatic or coulombic repulsion between the electron in $\mathcal{X}_i$ and that in $\mathcal{X}_j$

$$j_{ij} = \iint \mathcal{X}_i(1)\, \mathcal{X}_i^{*}(1) \frac{1}{\boldsymbol{r}_{ij}} \mathcal{X}_j(2) \mathcal{X}_j^{*}(2) d\tau_1 d\tau_2$$

2.1 8

The two-electron integrals represented by $\boldsymbol{K_{ij}}$ are called *exchange integrals*. The name *exchange integral* comes from the fact that the two electrons exchange their positions from the left to the right of the integrand. Although K_{ij} is often said to have no simple physical interpretation, the exchange integrals "correct" the Coulomb integrals in order to maintain the antisymmetry of the wave function [157]. It should be noted that the Coulomb "self-interaction" term J_{ii} is exactly cancelled by the corresponding "exchange" term K_{ii} [155]

$$K_{ij} = \iint \mathcal{X}_i^{*}(1) \mathcal{X}_j^{*}(2) \frac{1}{\boldsymbol{r}_{ij}} \mathcal{X}_i(1) \mathcal{X}_j(2) d\tau_1 d\tau_2 \qquad 2.19$$

2.1.6 Hartree–Fock equations

The objective now is to find the set of MOs or spin-orbitals ($\mathcal{X}_i$) that makes the HF energy E_{HF} a minimum, or at least stationary with respect to a change in the orbitals. This variation must be carried out in such a way that the MOs remain orthogonal and normalized (i.e., othornormal). This constrained minimization can be accomplished by employing the

Lagrange's method of undetermined multipliers, which introduces the *Lagrangian multipliers* ε_i in the resulting expressions known as the HF equations [155, 157]

$$\hat{f}_i \emptyset_i = \varepsilon_i \emptyset_i \qquad 2.20$$

where $\hat{f}_i$ is called the *Fock operator* and the Lagrangian multipliers ε_i are the eigenvalues of the operator. The ε_i values have the physical interpretation of orbital energies. The unique set of MOs (ϕ_i) obtained from a solution of these equations is called a set of *canonical molecular orbitals*. The Fock operator $\hat{f}_i$ is an effective one-electron operator, which has the form

$$\hat{f}_i = \frac{1}{2}\nabla_i^2 - \sum_A^M \frac{Z_A}{\boldsymbol{r}_{iA}} + V_{HF}(i) \qquad 2.21$$

In Equation **(2.21)**, the first two terms on the right represent the kinetic energy and the potential energy due to electrons-nuclei attractions, respectively. $V_{\mathrm{HF}}(i)$ is the Hartree–Fock potential, or equivalently the average repulsive potential experienced by the ith electron due to the other $2N$-1 electrons. $V_{\mathrm{HF}}(i)$ replaces the more complex $1/\mathbf{r}_{ij}$ repulsion operator, which is too complex to be solved easily. Explicitly, $V_{\mathrm{HF}}(i)$ comprises the following two terms:

$$V_{HF}(1) = \sum_{j=1}^{N}\left(\hat{J}_j(1) - \hat{K}_j(1)\right) \qquad 2.22$$

The potential $V_{\mathrm{HF}}(i)$ contains Coulombic interactions defined by the Coulomb operator $\hat{J}$ and exchange interactions described by the exchange operator $\hat{K}$. The Coulomb operator describes the electrostatic repulsion between each electron and the average field of the other electrons, whereas the exchange operator defines the exchange contribution to the HF potential, $V_{\mathrm{HF}}(i)$. Note that $\hat{K}$ has no simple physical interpretation, but arises from the antisymmetry requirement of the wave function [158]. The Fock operator $\hat{f}_i$ depends on its eigen functions, since the $V_{\mathrm{HF}}(i)$ seen by the ith electron depends on all the occupied MOs (via the Coulomb and exchange operators). Hence, the HF equations (**2.20**) are pseudo-eigenvalue equations that must be solved iteratively by the *self-consistent-field* or SCF process. The SCF procedure begins with the selection of an initial guess of the MOs, followed by the calculation of the average field $V_{\mathrm{HF}}(i)$ seen by each electron. Then, the pseudo-eigenvalue equation **(2.20)** is solved to obtain a new set of MOs. Using these new MOs, one can obtain a new average field $V_{\mathrm{HF}}(i)$ and then the procedure is repeated until self-consistency is reached, i.e., until the average field no longer changes and the MOs used to construct the Fock operator are the same as their eigen functions [161].

2.1.7 Roothaan-Hall equations

The HF equations might be solved numerically using integration over a grid for atomic systems. Practical procedures for obtaining numerical solutions for molecules are presently unavailable. An alternative approach has been introduced by Roothaan and Hall, which requires that the MOs (ϕ_i) of the system be expressed as linear combinations of a finite set $\{\varphi_\nu\}$ (called a basis set) of K known functions φ called basis functions [162]. A later section of this chapter is devoted to the types of basis sets.

$$\emptyset_i = \varepsilon_i \sum_{\nu}^{K} c_{\nu i}\, \varphi_\nu \qquad i = 1,2,\dots,K \tag{2.21}$$

where $c_{\nu i}$ is the expansion coefficient of the νth basis function (φ_ν) of the ith MO (ϕ_i). The basis functions φ are conventionally called atomic orbitals because they are usually (but not necessarily) centered at the nuclear positions. Hence, this linear combination of basis functions approach is commonly called Linear Combination of Atomic Orbitals (LCAO) approximation [155]. It should be noted that at least N MOs are required to accommodate all $2N$-electrons of the closed-shell molecule. As basis sets become more and more complete, the LCAO approximation generates more and more accurate representations of the "exact" MOs [161]. By substituting the expansion **(2.21)** for the MOs, the HF equations (**2.20**) become

$$\hat{f}_i \sum_{\nu}^{K} c_{\nu i}\, \varphi_\nu = \varepsilon_i \sum_{\nu}^{K} c_{\nu i}\, \varphi_\nu \tag{2.22}$$

Multiplying each term in **Equation (2.22)** on the left by φ_μ (or φ_μ^*in the case of a complex function), and integrating over all space yields:

$$\sum_{\nu}^{K} c_{\nu i}\, \mathrm{F}_{\mu\nu} = \varepsilon_i \sum_{\nu}^{K} c_{\nu i}\, \mathrm{S}_{\mu\nu} \tag{2.23}$$

where $F_{\mu\nu}$ and $S_{\mu\nu}$ are the *Fock matrix* (generally denoted as F) and the *overlap matrix* (generally denoted as S), with elements given by

$$\begin{aligned} \mathrm{F}_{\mu\nu} &= \int \varphi_\mu \hat{f} \varphi_\nu \\ S &= \int \varphi_\mu\, \varphi_\nu d\tau \end{aligned} \tag{2.24}$$

$F_{\mu\nu}$ is analogous to the Hamiltonian in the Schrödinger equation, and $S_{\mu\nu}$ is a measure of the extent to which the basis functions overlap with each other. The Equations given by equation **(2.23)** are known as the Roothaan-Hall equations, which are sometimes also called the Hartree–

Fock-Roothaan equations. The Roothaan–Hall equations are often written in a matrix form as follows:

$$\boldsymbol{FC} = \boldsymbol{SC\varepsilon} \qquad 2.25$$

where $\boldsymbol{C}$ is a matrix of expansion coefficients and $\boldsymbol{\varepsilon}$ is a diagonal matrix containing the orbital energies. The Roothaan-Hall equations **(2.23)** can be likened to eigenvalue equations, except for the overlap matrix $\boldsymbol{S}$. However, these equations are usually transformed into proper eigenvalue equations by orthogonalization of the basis functions, so that $\boldsymbol{S}$ vanishes. Then, the Roothaan-Hall equations are solved by the SCF procedure [161].

2.1.8 Restricted and unrestricted Hartree–Fock models

A closed-shell system is one containing an even number of electrons, which are all paired giving an overall singlet state. A vast majority of molecules belong to this class. Hartree–Fock calculations on closed-shell systems are known as *Restricted Hartree–Fock* (RHF) [155]. The restriction is that each spatial orbital must contain two electrons, one described by the α spin-function and the other by the β spin-function, both of which possess the same orbital energy. Hartree–Fock calculations on open-shell systems (either systems containing an odd number of electrons or systems with an even number of electrons, but not all of these electrons occupy pair-wise one spatial orbital) require more CPU time to execute. In dealing with open-shell systems, there are two common approaches namely; *Unrestricted Hartree–Fock* (UHF) and *Restricted Open-Shell Hartree–Fock* (ROHF). For the UHF approach, two different spatial orbitals are used for each pair of α and β electrons [157, 163]. This introduces an error into the calculation, called *spin contamination* [164]. In the case of ROHF, the paired electrons share the same spatial orbital, thus, there is no spin contamination. For the ROHF approach, MOs are occupied in the same manner as for RHF, except the unpaired electrons [165]. *Restricted Hartree–Fock* (RHF) is exploited in this work.

2.1.9 Electron correlation

The neglect or incomplete description of the correlation between electrons is inherent in the HF independent particle approximation, since it only accounts for electron–electron interactions in an average manner. Consequently, electrons often get too close to each other in the HF scheme. Electron correlation refers to the adjustments in the motion of an electron relative to the instantaneous positions of all other electrons in a molecule. In other words, it is the way in which the motion of one electron affects the motions of all other electrons [162].

The neglect or poor treatment of electron correlation causes the total energy of a given system calculated by the HF method to be overestimated with respect to the exact energy (E_{exact}). The energy error associated with the HF approximation is called *correlation energy* (E_{corr}), defined as the energy difference between the HF energy and the exact energy of a system as shown in Equation **(2.26)**. This energy is so named because it arises from the correlated movement of electrons seeking to become as far from each other as possible.

$$E_{corr} = E_{exact} - E_{HF} \tag{2.26}$$

Since the HF energy is an upper bound to the exact energy, Ecorr is always negative. To correct the electron correlation problem, correlated or Post-HF methods have been devised in the past decades, of which Configuration Interaction (CI), Coupled Cluster (CC) and the Møller-Plesset (MPn) perturbation theory are the most widely used. Since these methods aren't exploited in work, we would not delve into them.

2.2 Density functional theory (DFT)

The DFT has revolutionized quantum physics during the past two decades by providing a sound basis for predicting, modeling, designing and understanding the ground-state properties of molecules, clusters, solids and complex chemical problems, with an accuracy not easily obtainable by other approaches [166,167]. Indeed, the DFT has evolved to a powerful and very reliable tool that is routinely used for the determination of various molecular properties in organic, inorganic, material and solid-state physics, as well as in biochemistry and condensed matter physics. Furthermore, the DFT is computationally simple and faster than other methods with similar accuracy [164, 168, 169]. It is one of the most popular methods for treating large systems, including those containing metal, which is the case with the present work. Besides providing an excellent compromise between accuracy and computational time the DFT has shown itself to be a cost-effective method for incorporating electron correlation in quantum physical calculations. DFT models compute electron correlation via the so-called exchange-correlation density functionals. The DFT became a full-fledged theory only after the formulation of the Hohenberg and Kohn theorems in 1964. Unlike the wave function methods such as Hartree–Fock, Møller–Plesset, configuration interaction and coupled cluster theory, the DFT allows the computation of the energies, structures and molecular properties of various systems via their electron densities [157]. The simplicity of such computations has made the DFT a computationally attractive alternative to the wave function methods or the so called ab initio methods.

2.2.1 Electron density

DFT describes the electronic states of atoms, molecules and materials in terms of the three-dimensional electron density (also known as charge density or electron probability density) of the system. As such, the basic quantity in DFT is the electron density $\rho(\mathbf{r})$, which is the probability of finding an electron at a point **r** with coordinates (x, y, z) in a rectangular volume element $dxdydz$ within a molecular space. Shortly after the discovery of the Schrödinger equation, Max Born postulated that the square of a wavefunction Ψ times the volume element $dxdydz$ (i.e., $|\Psi|^2 dxdydz$) gives the probability of finding an electron in the volume element at the point (x,y,z). For an N-electron system with electronic wave function ψ, $|\psi(x_1,y_1,z_1,\ldots,x_N,y_N,z_N,m_{s1},\ldots,m_{sN})|^2 dx_1dy_1dz_1,\ldots,dx_Ndy_Ndz_N$ is the probability of simultaneously finding electron 1 with spin m_{s1} in the volume element $dx_1dy_1dz_1$ at (x_1,$_1$,z_1), electron 2 with spin m_{s2} in the volume element $dx_2dy_2dz_2$ at (x_2,y_2,z_2), and so on, until electron N with spin m_{sN} in the volume element $dx_Ndy_Ndz_N$ at (x_N,y_N,z_N). Multiplying the integral of this probability by the total number of electrons N gives the total electron probability density, simply known as electron density $\rho(\mathbf{r})$, for finding an electron in the neighborhood of the point **r**. The integral is over the coordinates of the other N-1 electrons, and is summed over all possible spins of all electrons.

$$\rho(\boldsymbol{r}) = N \sum_{all\ m_s} \int \ldots \int \left|\psi(x_1, y_{1,} z_1, \ldots x_N, y_{N,} z_{N,} m_{s1}, m_{sN}\right|^2 dx_1 \ldots dz_N \qquad 2.27$$

Since the integral in Equation **(2.27)** is summed over the possible spin states of all electrons, $\rho(\mathbf{r})$, is the total electron probability density of simultaneously finding each electron in the neighborhood of the point **r** with no regard for spin. Hence, $\rho(\mathbf{r})$, is a function of position only, i.e., of just the three variables (x, y, z). Clearly, the electron density of any system is a non-negative function [$\rho(r) \geq 0$] that vanishes at infinity [$(\mathbf{r}\rightarrow\infty) = 0$] and integrates over all space to give the total number of electrons N [$\int \rho(\boldsymbol{r})dr = N$]. Unlike the wave function, electron density is a physical observable that can be measured both computationally and experimentally by X-ray or electron diffraction methods.

2.2.2 The Hohenberg–Kohn (H – K) theorems

The approach developed by Hohenberg-Kohn was to reformulate the DFT proposed by Thomas-Fermi by an exact theory of the many body system. The advantage of DFT is that it is not necessary to calculate the complicated N-electron wave function. Instead, one can restrict himself in calculating the much simpler electron density $\rho(\boldsymbol{r})$, a fact that was first proven by

Hohenberg and Kohn [170]. The first H – K theorem demonstrates that the ground state properties of a many-electron system are uniquely determined by an electron density which depends on only 3 spatial coordinates. It laid the ground work for reducing the many-body problem of N electrons with 3N spatial coordinates to only 3 spatial coordinates, through the use of functional of the electron density. This theorem has been extended to the time – dependent domain to develop Time – Dependent Density Functional Theory (TDDFT), which can be used to describe excited state. The second H – K theorem defines the energy functional of a system and proves that the correct ground state electron density minimizes this energy functional. This is the analogue of the variational principle for wave functions. This means that the exact ground state energy can be found by minimization of the energy functional.

2.2.3 Kohn-Sham (KS) approach

The second significant advancement in DFT was made in 1965, when Kohn and Sham devised a practical method for finding the Hohenberg–Kohn functional $F_{\mathrm{HK}}[\,\rho_0]$. Kohn and Sham considered a reference system (herein denoted by the subscript s) with N non-interacting electrons, and which experiences the same external potential as the real system with interacting electrons. As such, the ground-state electron density of the reference system $\rho_s(\mathbf{r})$ is exactly the same as that of the real system $\rho_0(\mathbf{r})$, i.e., $\rho_s(\mathbf{r})= \rho_0(\mathbf{r})$ [158, 171]. Furthermore, the reference system is constructed from a set of one-electron functions called Kohn–Sham orbitals, ψi^{KS} so that a major part of the system's kinetic energy can be computed with good accuracy. Based on this premise, Kohn and Sham expressed the Hohenberg–Kohn functional $F_{\mathrm{HK}}[\,\rho_0]$ as:

$$F_{HK}[\rho_0] = T_S[\rho_0] + J[\rho_0] + E_{XC}[\rho_0] \qquad 2.28$$

Here, $T_S[\rho_0]$ represents the kinetic energy functional of the reference system, given by

$$T_S[\rho_0] = \sum_i^N \left\langle \psi_i^{KS} \middle| -\frac{1}{2}\nabla_i^2 \middle| \psi_i^{KS} \right\rangle \qquad 2.29$$

$J[\rho_0]$ represents the classical columbic energy due to electron-electron interaction, given

$$J[\rho_0] = \frac{1}{2}\iint \frac{\rho_0(\boldsymbol{r}_1)\rho_0(\boldsymbol{r}_2)}{\boldsymbol{r}_{12}}\, d\boldsymbol{r}_1 d\boldsymbol{r}_2 \qquad 2.30$$

The remaining and unknown energy components of $F_{\mathrm{HK}}[\rho_0]$ are assembled in the functional $E_{XC}[\rho_0]$, which computes the so-called *exchange-correlation energy*. $E_{XC}[\rho_0]$ functional comprises the following functionals: $T_{\mathrm{C}}[\rho_0]$ which represents the difference between the exact

kinetic energy T and Ts; $E_{\text{ncl}}[\rho_0]$ which is the non-classical part (comprising the Fermi and Coulomb correlation) of $E_{\text{ee}}[\rho_0]$ and finally, the non-classical self-interaction correction [172]

$$E_{XC}[\rho_0] = \{T[\rho_0] - T_S[\rho_0]\} + \{E_{ee}[\rho_0] - J[\rho_0]\} \equiv T_C[\rho_0] + E_{ncl}[\rho_0] \quad 2.31$$

From Equations **(2.28)**, the total Kohn–Sham true ground energy of the real system containing N interacting electrons and M nuclei is given by [173]

$$E_0 = \int \rho_0(\boldsymbol{r}_1) v_{Ne}\, d\boldsymbol{r} + T_S[\rho_0] + J[\rho_0] + E_{XC}[\rho_0]$$

$$= \int \rho_0(\boldsymbol{r}_1) v_{Ne}\, d\boldsymbol{r} + \sum_i^N \left\langle \psi_i^{KS} \middle| -\frac{1}{2}\nabla_i^2 \middle| \psi_i^{KS} \right\rangle + \frac{1}{2}\iint \frac{\rho_0(\boldsymbol{r}_1)\rho_0(\boldsymbol{r}_2)}{\boldsymbol{r}_{12}} d\boldsymbol{r}_1 d\boldsymbol{r}_2 + E_{XC}[\rho_0] \quad 2.32$$

Before evaluating the terms in Equation **(2.32)**, the ground-state electron density $\rho_0(\mathbf{r})$ needs to be found. Using the KS orbitals ψ_i^{KS}, $\rho_0(\mathbf{r})$ is calculated as follows

$$\rho_0(\boldsymbol{r}) = \rho_s(\boldsymbol{r}) = \sum_{i=1}^N \left|\psi_i^{KS}(\boldsymbol{r})\right|^2 \quad 2.33$$

Hence, the Kohn–Sham energy equation **(2.32)** can be rewritten as

$$E_0 = -\sum_i^N \int \sum_A^M \frac{Z_A}{\boldsymbol{r}_{1A}} \left|\psi_i^{KS}(\boldsymbol{r}_1)\right|^2 d\boldsymbol{r}_1 - \frac{1}{2}\sum_i^N \left\langle \psi_i^{KS} \middle| \nabla_i^2 \middle| \psi_i^{KS} \right\rangle +$$

$$\frac{1}{2}\sum_i^N \sum_j^N \iint \left|\psi_i^{KS}(\boldsymbol{r}_1)\right|^2 \frac{1}{\boldsymbol{r}_{12}} \left|\psi_i^{KS}(\boldsymbol{r}_2)\right|^2 d\boldsymbol{r}_1 d\boldsymbol{r}_2 + E_{XC}[\rho_0] \quad 2.34$$

The only term in the Kohn–Sham energy expression for which no explicit form can be given is the functional $E_{XC}[\rho_0]$. According to Equation **(2.34)**, it is possible to obtain the ground-state energy E_0 from the ground-state electron density $\rho_0(\mathbf{r})$ if the KS orbitals ψ_i^{KS} and the functional $E_{XC}[\rho_0]$ were known. The KS orbitals can be obtained by solving the Kohn–Sham equations

2.2.4 The Kohn–Sham equations

The KS equations **(2.35)** are derived by applying the Hohenberg–Kohn (HK) variational theorem (i.e., the second HK theorem), whereby the KS energy given by Equation **(2.34)** is minimized with respect to the KS orbitals ψ_i^{KS} subject to the constraint that the orbitals remain orthonormal, i.e., $\langle \psi_i^{KS} | \psi_j^{KS} \rangle = \delta_{ij}$ [158, 165] The resulting equation is (for detailed derivation, see [174])

$$\left(-\frac{1}{2}\nabla_i^2 - \sum_A^M \frac{Z_A}{\boldsymbol{r}_{1A}} + \int \frac{\rho(\boldsymbol{r}_2)}{\boldsymbol{r}_{12}} d\boldsymbol{r}_2 + V_{XC}(1)\right)\psi_i^{KS}(1) = \varepsilon_i^{KS}\psi_i^{KS}(1) \quad 2.35$$

where ε_i^{KS} are the Kohn–Sham energy levels, and $V_{XC}(1)$ is the exchange-correlation potential due to the exchange-correlation energy E_{XC}. Actually, $V_{\mathrm{XC}}(1)$ is the functional derivative of $E_{\mathrm{XC}}[\rho(\mathbf{r})]$ as shown in Equation **(2.36)**

$$V_{XC}(\boldsymbol{r}) = \frac{\delta E_{XC}[\rho(\boldsymbol{r})]}{\delta \rho(\boldsymbol{r})} \qquad 2.36$$

The quantity $-\frac{1}{2}\nabla_i^2 - \sum_A^M \frac{Z_A}{\boldsymbol{r}_{1A}} + \int \frac{\rho(\boldsymbol{r}_2)}{\boldsymbol{r}_{12}} d\boldsymbol{r}_2 + V_{XC}(1)$ in Equation **(2.35)** is the one-electron Kohn–Sham operator, which is often denoted as $\hat{h}_i^{KS}$. Using this notation, the Kohn–Sham equations can be rewritten as

$$\hat{h}_i^{KS}\psi_i^{KS}(1) = \varepsilon_i^{KS}\psi_i^{KS}(1) \qquad 2.37$$

The Kohn–Sham one-electron equations **(2.37)** can be solved iteratively to obtain the KS orbitals ψ_i^{KS} and the KS energies ε_i^{KS}. It should be noted that the KS orbitals are the orbitals of the fictitious reference system of non-interacting electrons, so, strictly speaking, KS orbitals have no physical significance other than that they allow the exact molecular ground-state electron density $\rho_0(\mathbf{r})$ to be calculated from equation **(2.33).** However, the occupied KS orbitals resemble the Hartree–Fock MOs, and can be used (just as Hartree–Fock MOs are used) for the qualitative interpretation and rationalization of molecular properties and reactivities [158,175]. DFT is an exact theory in principle, but approximate exchange-correlation functionals are used, since the exact forms of E_{XC} and V_{XC} are unknown. In practice, approximations are made to decide on the explicit form of the unknown exchange-correlation functional that computes the exchange-correlation energy E_{XC} and V_{XC}. Obviously, the approximate variants of the DFT currently in use are far from being fail-safe. Nevertheless, the key to accurate KS-DFT calculations of molecular properties is to get a good approximation to the exchange-correlation functional

2.2.5 Approximations to the exchange-correlation energy functionals

The exchange-correlation energy E_{XC} contains non-classical contributions to the potential energy, as well as the difference between the kinetic energy of the non-interacting reference system and that of the real interacting system. Various approximate exchange-correlation functionals $E_{\mathrm{XC}}[\rho]$ are used in molecular DFT calculations. To study the accuracy of an approximate $E_{\mathrm{XC}}[\rho]$, it should be used in KS-DFT calculations and the calculated molecular properties are then compared with the experimental counterparts [158]. The most commonly

used approximate exchange-correlation density functionals within the framework of the Kohn–Sham method include:

• Local density approximation (LDA) functionals

The LDA is the simplest approximation to $E_{\mathrm{XC}}[\rho]$ whereby, only the electrons at a given point in a system are used for determining the point's contribution to the total E_{XC} of the system [175]. In the LDA, electron density $\rho(\mathbf{r})$ is treated locally as a uniform electron gas [155]. A uniform electron gas is a hypothetical system of free electrons in which $\rho(\mathbf{r})$ varies very slowly with position $\mathbf{r}$ and, as such, its value is fairly constant everywhere. Hohenberg and Kohn showed that if $\rho(\mathbf{r})$ varies (differentiates) extremely slowly with position, then $E_{\mathrm{XC}}[\rho]$ is accurately given by Equation **(2.38)**.

$$E_{XC}^{LDA}[\rho] = \int \rho(\boldsymbol{r})\varepsilon_{XC}(\rho)d\boldsymbol{r} \qquad 2.38$$

The integral is over all space, and $\varepsilon_{XC}(\rho)$ is the exchange plus correlation energy per electron in the uniform electron gas with electron density $\rho(\mathbf{r})$. The most common form of the LDA assumes the Slater exchange term (S) together with the Vosko, Wilk and Nussair parameterization (VWN) of the exact uniform electron gas model for the correlation part, both of which constitute the SVWN Model [162]. It should be noted that the LDA is not accurate enough for chemical applications [173].

- **Local spin density approximation (LSDA) functionals**

For open-shell systems, the LSDA gives better results than the LDA. In the case of the LDA, electrons with opposite spins are paired in the same KS orbital, whereas the LSDA assigns electrons with α and β spins to different spatial KS orbitals $\psi_{i\alpha}^{KS}$ and $\psi_{i\beta}^{KS}$, from which the electron densities $\rho^{\alpha}(\mathbf{r})$ due to spin–α electrons and $\rho^{\beta}(\mathbf{r})$ due to spin–β electrons are computed, respectively. The LSDA is generally of the form

$$E_{XC}^{LSDA}[\rho] = \int \rho(\boldsymbol{r})\varepsilon_{XC}\left(\rho^{\alpha}, \rho^{\beta}\right)d\boldsymbol{r} \qquad 2.39$$

The LSDA, like the LDA is based on the uniform electron gas model [158, 165], but unlike the LDA, the LSDA works surprisingly well for calculating molecular geometries, vibrational frequencies and dipole moments and for metal-containing compounds. However, molecular atomization energies calculated with the LSDA are not very accurate. More accurate results can be obtained with functionals that go beyond the LSDA [175].

• Generalized gradient approximation (GGA) density functional

This is an improvement over the LSDA by making the exchange and correlation energies dependent not only on the electron density, but also on its gradient [155]. The GGA functional are typically obtained by including the gradients of $\rho^{\alpha}(\mathbf{r})$ and $\rho^{\beta}(\mathbf{r})$ in the integrand of Equation **(2.39)**. As a result, the GGA is said to be gradient-corrected. The GGA is generally of the form

$$E_{XC}^{GGA}[\rho] = \int f(\rho^{\alpha}(\boldsymbol{r}), \rho^{\beta}(\boldsymbol{r}), \nabla\rho^{\alpha}, \nabla\rho^{\beta}) d\boldsymbol{r} \qquad 2.40$$

where f is some function of the spin densities and their gradients. The gradient-corrected functionals were initially called "non-local" functionals because some non-local effects are incorporated via the gradient of the electron density, in the determination of any point's contribution to the total exchange correlation energy [175]. Three of the most popular GGA functionals are; **BLYP** (comprising the Becke's 1988 exchange functional [176] and the correlation functional of Lee, Yang and Parr [177]), **BP86** (comprising the Becke's 1988 exchange functional and the Perdew's 1986 correlation functional [178]), and **PBE** (the Pewdew, Burke and Ernzerhof GGA [179]).

• Meta-GGA (MGGA) density functionals

The *meta*-GGA functionals depend on the electron density ($\mathbf{r}$), its gradient $\nabla(\mathbf{r})$, its Laplacian $\nabla^2\rho(\mathbf{r})$ and/or the orbital kinetic energy density τ (semi-local interactions) [175]. Generally, the inclusion of the Laplacian and/or the orbital kinetic energy density as a variable into GGA functionals leads to the so-called *meta*-GGA functionals. The typical form of MGGA functionals is

$$E_{XC}^{MGGA}[\rho] = \int f(\rho^{\alpha}(\boldsymbol{r}), \rho^{\beta}(\boldsymbol{r}), \nabla\rho^{\alpha}, \nabla\rho^{\beta}, \nabla^2\rho^{\alpha}, \nabla^2\rho^{\beta}, \tau^{\alpha}, \tau^{\beta}) d\boldsymbol{r} \qquad 2.41$$

The orbital kinetic energy density τ is given by **Equation (2.42)**, in which σ stands for α or β, and $\psi_{i\alpha}^{KS}$ are self-consistently determined Kohn–Sham orbitals

$$\tau^{\alpha} = \frac{1}{2}\sum_{i}^{N}\left|\nabla\psi_{i\alpha}^{KS}\right|^2 \qquad 2.42$$

It is worth noting that the calculation of the orbital kinetic energy density is numerically more stable than the calculation of the Laplacian of the electron density. As a result of such numerical instabilities linked to the use of the Laplacian in functional approximations, the orbital kinetic energy density is a common component of *meta*-GGA functionals. The commonly used *meta*-

GGA fucntionals are; the Minnesota functional **M06-L** [180] and the Tao–Perdew–Staroverov–Scuseria functional **TPSS** [181].

The LDA, LSDA, GGA and *Meta*-GGA functionals are generally classified as *local functionals* because they are defined in terms of spin-densities (ρ^{α},ρ^{β}), their gradients ($\nabla\rho^{\alpha}$,$\nabla\rho^{\beta}$) and their Laplacian ($\nabla^2\rho^{\alpha}, \nabla^2\rho^{\beta}$) or orbital kinetic energy densities (τ^{α},τ^{β}), all of which only depend on the local values of these variables at a given point in space. When non-local effects are incorporated into these functionals by inclusion of some exact Hartree–Fock (HF) exchange, hybrid functionals are formed.

• Hybrid density functionals

Hybrid density functionals are usually GGA or *meta*-GGA functionals wherein part of the DFT exchange is substituted with non-local exact exchange calculated by the HF theory [165, 175]. Here, it is noteworthy that in the calculation of the HF exchange energy, KS orbitals are used in place of HF orbitals. The percentage of HF exchange used is the main distinguishing factor of the various hybrid functionals. The first popular and successful hybrid functional was the Becke's three-parameter Lee-Yang-Parr (**B3LYP**) (Becke, 1988; Lee, 1988) comprising 20% HF exchange. It has been used as a standard hybrid functional, although specific limitations and failures have also been identified [160]. Other commonly used hybrid functionals in recent times are; the Minnesota functionals **M06** and **M06-2X** comprising 27% and 54% HF exchange respectively, the **PBE0** functional (also denoted PBE1PBE in the literature) obtained by adding about 25% HF exchange to the GGA functional PBE, the **TPSSh** functional obtained by augmenting the *meta*-GGA functional TPSS with about 10% HF exchange. The TPSSh functional is emerging as a potential new standard for hybrid DFT calculations [160]. **B3LYP** and **PBE** have been exploited in this research work

Hybrid functionals perform better than local functionals for general-purpose applications in physics [182]. At least part of this improvement may arise from the reduction of self-interaction error via the inclusion of exact HF exchange, since the HF theory is completely self-interaction free due to the fact that the coulomb term (J_{ij}) is exactly cancelled by the exchange term (K_{ij}) for a one-electron system [155]. Generally, approximate DFT functionals describe an artificial interaction term of one electron with itself, leading to the so-called *self-interaction error*. The error arises because the exchange contributions are usually significantly larger in absolute numbers than the corresponding correlation effects, caused by the approximations made to the

exchange-correlation functional [173]. In particular, the local and semi-local functionals suffer from severe self-interaction error.

• Range-separated density functionals

It has been recently suggested that range-separation can fix errors caused by the absence of dispersion corrections in standard density functionals [183]. Range-separated density functionals are functionals in which electron–electron interaction is separated into a short-range and a long-range part, or even into three parts (short-, middle- and long-range), and then one part of the exchange energy is treated by the HF method and the other part or parts by a local exchange functional [171]. One way of constructing a range-separated functional is by treating the short-range exchange using a local functional, while the long-range exchange is mainly treated using exact HF exchange [175]. Two popular range-separated functionals are; the Coulomb-attenuating method B3LYP (**CAM-B3LYP**) [184] and ***ω*B97X** [185], together with its dispersion-corrected variant. ***ω*B97X-D**.

2.3 Basis sets

The first step in any theoretical calculation on atoms and molecules is the determination of atomic and molecular wave functions respectively, which are usually constructed from a set (called basis set) of one-electron one-center functions known as basis functions [186]. In electronic structure theory, a *basis set* is a set of nonorthogonal one-electron functions whose linear combinations yield the molecular orbitals (MOs) of a chemical system. As mentioned earlier, the approximation of MOs as linear combinations of basis functions is referred to as the *Linear Combination of Atomic Orbitals* (LCAO), although the basis functions are not necessarily conventional atomic orbitals. The goal of any basis set is to provide the best representation of MOs (or the electron density) with as small a computational cost as possible [155]. A basis set that describes the actual wave function well enough gives chemically useful results. Calculations with larger basis sets (i.e., more complete basis sets) are more reliable because the atomic or molecular orbitals of the system are more accurately approximated by such basis sets, which impose fewer restrictions on the locations of the electrons in space. However, calculations with larger basis sets are more computationally expensive, since more integrals are computed. It should be noted that in quantum physics, an N-electron basis set refers to a set of Slater determinants.

There exist different types of basis functions, among which the Slater-Type Orbitals (STOs) and Gaussian-Type Orbitals (GTOs) are the most prominent and commonly used in electronic structure theory calculations [155].

2.3.1 Slater-type orbitals (STOs)

The STOs are described by functions that depend on spherical coordinates as shown in

$$\varphi_{\zeta,n,l,m}(r,\theta,\emptyset) = \mathcal{N}Y_{l,m}(\theta,\emptyset)r^{n-1}e^{-\zeta r} \quad 2.43$$

where r,θ and ϕ are spherical coordinates, $\mathcal{N}$ is the normalization constant, $Y_{l,m}$ controls angular momentum (it describes the "shape"), r is the orbital radius in angstroms and ζ (zeta) is the orbital exponent, which controls the width of the orbital (a larger ζ gives a tighter function, while a smaller ζ gives a more diffuse function). The letters , and m represent the principal, angular momentum and magnetic quantum numbers, respectively.

2.3.2 Gaussian-type orbitals (GTOs)

The GTOs can be expressed in terms of either polar or Cartesian coordinates as shown

$$\varphi_{\zeta,n,l,m}(r,\theta,\emptyset) = \mathcal{N}Y_{l,m}(\theta,\emptyset)r^{2n-2-l}e^{-\zeta r^2} \quad 2.44$$

$$\varphi_{\zeta,a,b,c}(x,y,z) = \mathcal{N}x^a y^b z^c e^{-\zeta r^2} \quad 2.45$$

where N is the normalization constant, $Y_{l,m}$ controls angular momentum, r is the orbital radius in angstroms, ζ controls the width of the orbital, the letters a, b and c are non-negative integers that control angular momentum. The sum of a, b and c determines the type of orbital, for example, if a+b+c=0, the GTO is an s-type function and if a+b+c=1, the GTO is a p-type function

The exponential $e^{-\zeta r2}$ of the GTOs in contrast to $e^{-\zeta r}$ of the STOs has made the GTOs inferior to the STOs in the following two respects

• The GTOs are not hydrogen-like functions even for the 1s orbital. Hence, a GTO is a poor approximation of an atomic orbital compared to the nearly ideal description that an STO provides

•A GTO decays somewhat faster than an STO at large r i.e., the GTO falls off too rapidly far from the nucleus as compared to an STO. Hence, unlike the GTOs, STOs have the correct asymptotic long-range behavior.

Despite the accuracy of the STOs, it takes longer to compute the two-electron STO-based integrals. In terms of computational efficiency, the GTOs are preferred over the STOs and are used almost universally as basis functions in theoretical calculations, since the integrals based on them are easier to evaluate [155, 157].

2.3.3 Contracted Gaussian-type orbitals (CGTOs)

The deficiencies of the GTOs as compared to STOs are usually mitigated by using a linear combination of enough GTOs to mimic an STO. A basis function composed of a linear combination of GTOs is referred to as a *contracted Gaussian type orbital* (CGTO), and the component of CGTOs are known as *primitive* GTOs, which are usually centered on the same nucleus [186]. A basis function consisting of a single GTO is termed *uncontracted*. A CGTO comprising n Gaussians to mimic an STO is dubbed "STO-nG", where n is an integer that can take the values 2, 3, 4, 5 or 6, for example, STO-3G denotes a "Slater-type orbital approximated by three Gaussians".

2.3.4 Basis set families

There are eight families of basis sets available in several quality levels, and defined for a reasonable number of elements in the periodic table.

(i) The Pople-style k-lmnG basis sets.
(ii) The Ahlrichs or Karlsruhe SVP, TZP, QZP basis sets and their Def2 versions.
(iii) The XZP basis sets developed by Jorge and coworkers.
(iv) The Sapporo basis sets developed by Koga and coworkers.
(v) The atomic natural orbital (ANO) basis sets developed by Roos and coworkers.
(vi) The correlation-consistent basis sets (cc-pVXZ) basis sets developed by Dunning, and Peterson and coworkers.
(vii) The nZaP basis sets developed by Petersson and coworkers.
(viii) The polarization-consistent basis sets (pc-n) developed by Jensen and coworkers

Throughout the rest of this thesis, much attention we will be focused on the Pople-style

2.3.5 Basis set classification

Based on the number of contracted functions, basis sets have been classified as follows

• Minimal or single-zeta (SZ) basis sets

Minimal or SZ basis sets (the STO-nG) contain the minimum number of basis functions (CGTOs) needed for each atom, and each occupied orbital is described by one basis function. Minimal basis sets are used for very large molecules and for exploratory purposes only. They generally provide poor results for molecules, since they are inadequate to describe the deviations from the spherical symmetry of atoms and the process of bond formation.

• Double-, triple- and quadruple-zeta basis sets

The double-zeta (DZ), triple-zeta (TZ) and quadruple-zeta (QZ) basis sets use two, three and four basis functions respectively, per atomic orbital, and both the valence and core orbitals are split. The DZ, TZ and QZ basis sets are much better than the SZ basis sets at describing bond formation, since they employ different ratios of basis functions with different exponents to describe the various bonding characteristics in different directions.

•Split-, triple split- and quadruple split-valence basis sets

A split-valence basis set represents the core atomic orbitals by one set of basis functions (contracted) and the valence atomic orbitals by two sets of basis functions. In this case, hydrogen is provided two s-type functions and the main-group elements are provided two sets each of valence s-type and valence p-type functions. In the case of triple split- and quadruple split-valence basis sets, the valence atomic orbitals are split into three and four parts respectively. The Pople-style basis sets are generally of the form k-nlmG, where the k in front of the dash indicates the number of GTOs used for representing the core orbitals, while the letters nlm after the dash indicate both the number of functions the valence orbitals are split into and how many GTOs are used for their representation. Two values (nl) indicate a split-valence basis set e.g., 6-31G, while three values (nlm) indicate a triple split-valence basis set e.g., 6-311G. For the Ahlrichs or Karlsruhe basis set family, there exist split-valence (e.g., def2-SVP), triple-zeta valence (e.g., def2-TZVP) and quadruple-zeta valence (e.g., def2-QZVP) basis sets. Note that the "P" in these basis sets indicates the presence of polarization functions as discussed below

2.3.6 Adding polarization functions to basis sets

One drawback of the SZ, DZ, TZ and QZ, as well as the Split-, triple split- and quadruple split-valence basis sets is that their basis functions are atom centered, which restricts their flexibility in describing electron distributions or the bonds between nuclei. This shortcoming may be

addressed by providing d-type functions for the "heavy atoms" (atoms beyond helium in the periodic table), which contain s and p-type valence orbitals. Optionally, p-type functions may be also provided for hydrogen and helium, which contain s-type valence orbitals. These additional p and d-type functions are called *polarization functions*, which account for orbital polarization that occurs when bonds are formed in molecules to provide optimal bonding. The polarization functions allow displacement of electron distributions away from the nuclear positions as shown in **Figure 2.1**, by enabling orbitals to change not only their sizes, but also their shapes.

Generally, a polarized basis set incorporates basis functions of higher angular momentum quantum number beyond what is required by the atom in its electronic ground-state. Therefore, to polarize a basis function with angular momentum quantum number l, it is mixed with a polarization function of angular momentum quantum number l+1. Examples of polarized Pople-style basis sets are 6-31G(d) or 6-31G* and 6-311G(d,p) or 6-311G**, where d and d,p in parenthesis or the asterisk(s) indicate the presence of polarization function.

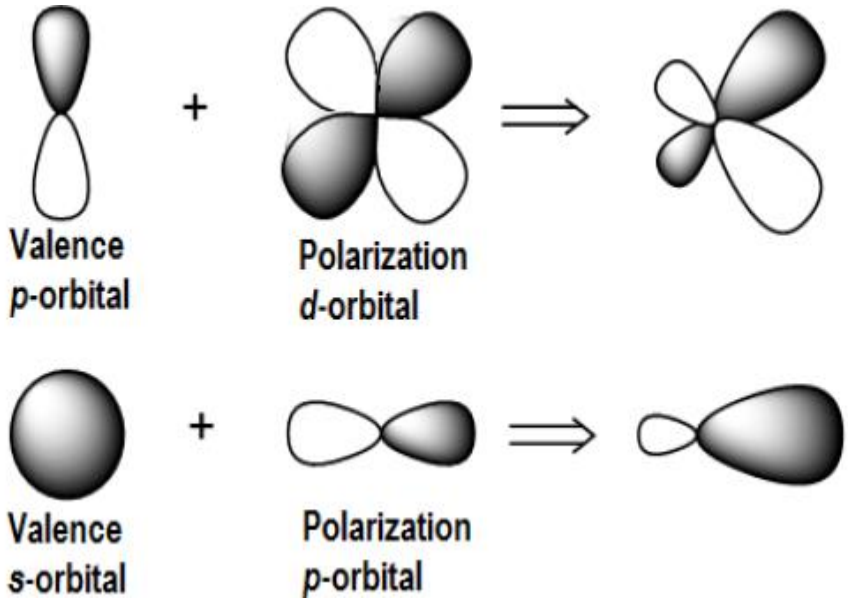

Figure 2.1 Effects of polarization functions on electron distribution

2.3.7 Adding diffuse functions to basis sets

For some applications, diffuse functions (i.e., functions with smaller ζ exponents) must be added to obtain accurate (or even meaningful) results. Diffuse functions enable a proper description of electron distributions far away from the nucleus, and are thus required for anions, polar bonds, weak intermolecular interactions, Rydberg orbitals and systems in their excited

states. In these situations, basis sets may be supplemented with diffuse s and p-type functions for the heavy atoms. For the Pople-style basis sets, diffuse functions are designated by "+" as in 6-311+G**. It is also possible to add diffuse functions to both the heavy and hydrogen atoms, designated by "++" as in 6-311++G**. For the Ahlrichs basis sets, diffuse functions may be added according to [187], designated by "D" as in def2-TZVPD. Also, the Ahlrichs basis sets may be minimally augmented with diffuse s and p functions according to [188], denoted "ma" as in ma-def2-TZVP.

2.4 Gaussian Package

It is a computational Physics and Chemistry program. It name comes from the fact that it uses Gaussian type basis functions. Starting from the fundamental laws of quantum mechanics, the Gaussian 09 [189] can predict the electronic and geometric structure optimization (single point calculation, geometry optimization, transition states and reaction path modeling); and molecular properties and vibrational analysis (IR, Raman, NMR vibrational frequencies and normal modes; electrostatic potential, electron density, multipole moments, population analysis, natural orbital analysis, magnetic shielding induced current densities, static and frequency-dependent polarizabilities and hyperpolarizabilities) using both DFT and ab initio methods. Gauss View 5.0 is employed for realizing data and displaying the outcomes of the output [190]. Optimization of geometry and vibrational frequencies by the Gaussian are shown below.

Geometry optimization is done by locating both the minima and transition states on the potential surface. It can be optimized in Cartesian coordinates that are generated automatically from the input Cartesian coordinates. It also handles fixed constraints on distances bond angles and dihedral angles in Cartesian or (where appropriate) internal coordinates. The process is iterative, with repeated calculations of energies and gradients and calculations or estimations of the Hessian matrix in every optimization cycle until convergence is attained (see scheme in figure 2.2). The whole art of geometry optimization lies in the calculation of the step h so as to converge in a few such cycles as possible.

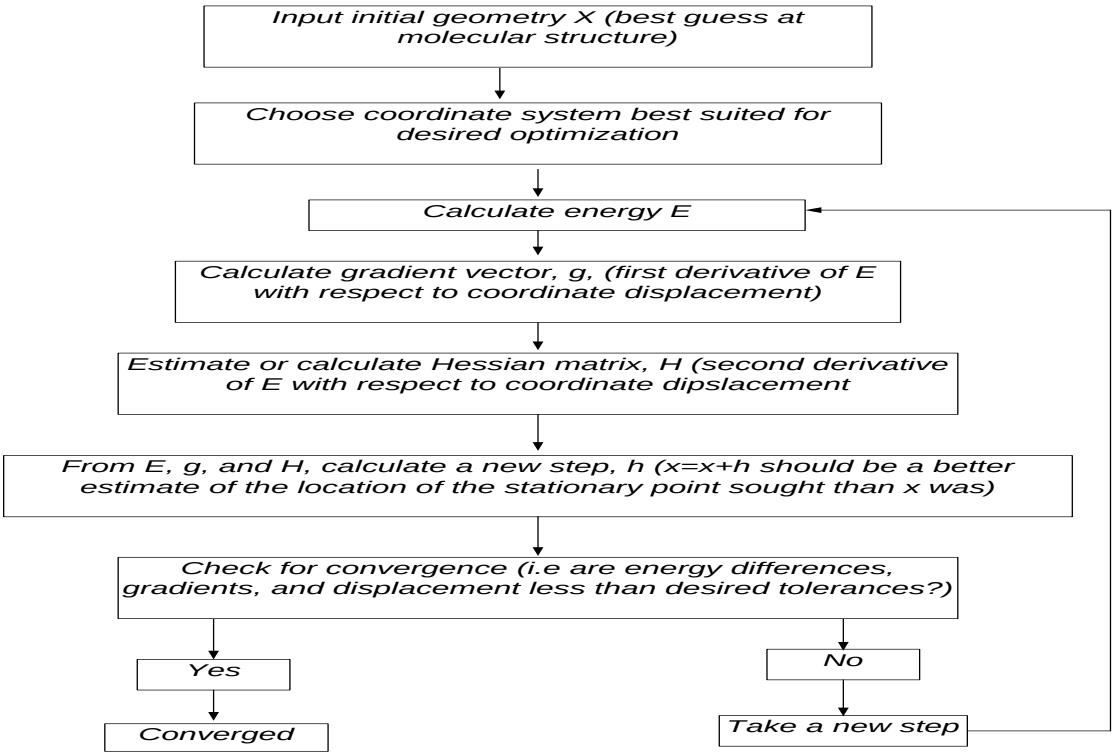

Figure 2.2 schematic for geometric optimization by the Gaussian program.

2.5 Methodology

In this chapter, the methodology employed in this research is described, which comprises the DFT as the main quantum chemical method used, along with other computational techniques based on topological analysis of the electron density

2.5.1 Methodology of the determination of the NLO

The nonlinearity at the microscopic scale can be defined by the dipole moment induces in non-linear optical material. So, as we mentioned in chapter 1, the induced dipole moment is written as a series expansion of the electric field E as follows

$$\mu_i(\mathbf{E}) = \mu_0 + \sum_j \alpha_{ij} E_j + \sum_{j\leq k} \beta_{ijk} E_j E_k + \sum_{j\leq k\leq l} \gamma_{ijkl} E_j E_k E_l + \cdots \quad 2.45$$

μ_0 is the permanent dipole moment of the molecule, α_{ij}, β_{ijk} and γ_{ijkl} are tensors representing the polarizability, the first order hyperpolarizability and the second order hyperpolarizability respectively. Within the limits of a weak polarization introduced by relatively non-intense field, the energy E of a system can also be written as an expansion in Taylor series induced by the electric field **E** as follows [191]

$$E_i(\boldsymbol{E}) = E_0 - \sum_j \mu_i \boldsymbol{E}_j - \frac{1}{2}\sum_{i,j} \alpha_{ij} \boldsymbol{E}_j \boldsymbol{E}_k - \frac{1}{6}\sum_{i,j,k} \beta_{ijk} \boldsymbol{E}_i \boldsymbol{E}_j \boldsymbol{E}_k + \cdots \quad 2.46$$

E_0 is the total energy of the system in the absence of an electric field. The tensors α and β are defined [192] by the first and second derivations of the induced dipole moment with respect to the field **E** or by the second and third derivations of the total energy with respect to the field **E**

$$\alpha = \left(\frac{\partial \mu_i}{\partial \boldsymbol{E}}\right)_0 \; and \; \beta = \left(\frac{\partial^2 \mu_i}{\partial \boldsymbol{E}^2}\right)_0 \qquad 2.47$$

$$\alpha = \left(\frac{\partial^2 E}{\partial \boldsymbol{E}^2}\right)_0 \text{and} \;\; \beta = \left(\frac{\partial^3 E}{\partial \boldsymbol{E}^3}\right)_0 \qquad 2.48$$

The nonlinear properties (polarizability and hyperpolarizability) are generally determined by the finite field method. The finite field method was introduced for the first time by Cohen and Roothaan [193]. The principle of the method is to obtain the components of polarizability tensor (α_{ij}) and the hyperpolarizability tensor (β_{ijk}) by successive numerical derivations of the dipole moment or of the total energy with respect to components of the electric field within the limit of a zero field. The mean polarizability α_0 and the first order static hyperpolarizability β_0 are determined from the components calculated with the Gaussian program by the following formulas [193, 195]

$$\alpha_0 = \frac{\alpha_{xx}+\alpha_{yy}+\alpha_{yy}}{3} \qquad 2.49$$

$$\Delta\alpha = [\frac{1}{2}\left(\left(\alpha_{xx}-\alpha_{yy}\right)^2 + (\alpha_{xx}-\alpha_{zz})^2 + \left(\alpha_{yy}-\alpha_{zz}\right)^2 + 6\left(\alpha_{xy}+\alpha_{xz}+\alpha_{yz}\right)^2\right)]^{\frac{1}{2}} \qquad 2.50$$

$$\beta_0 = \left(\left(\beta_{xxx}+\beta_{xyy}+\beta_{xzz}\right)^2 + \left(\beta_{yyy}+\beta_{yxx}+\beta_{yzz}\right)^2 + \left(\beta_{zzz}+\beta_{zxx}+\beta_{zyy}\right)^2\right)^{1/2} \qquad 2.51$$

2.5.2 Methodology of the determination of the electronic properties

In an isolated atom, the energy of electrons can have only well-defined discrete values in contrast to the continuum energy in the case of a free electron. In a solid, the situation is intermediate: the electron can have any energy value within certain intervals. So the solid has bands of permitted energies, separated by forbidden bands. This representation in energy bands is a simplified and partial representation of the density of electronic states. The electrons of the solid are distributed in the permitted energy levels; this distribution depends on the temperature and obeys the statistics by Fermi-Dirac [196]. Two permitted energy bands play a special role. The last completely filled band is called "valence band". The allowed energy band which

follows it is called the "conduction band". It can be empty or partially filled. The energy that separates the valence band from the conduction band is called the "gap" (band gap).

The electrons of the valence band contribute to the local cohesion of the solid (between neighboring atoms) and are in localized states. They cannot participate in the phenomena of electrical conduction. Conversely, the electrons of the conduction band are delocalized. It is these electrons which participate in electrical conduction. Electronic properties of the solid therefore depend essentially on the distribution of electrons in these two bands as well as the value of the gap: in the case of insulators, the two bands are separated by a significant gap. For conductors, the conduction band is partially occupied, which allows electrons in this band to move to higher energy levels, without violating the Pauli Exclusion Principle, and thus participate in the conduction. Semiconductors have a sufficiently low gap and electrons have small probability to cross it by simple thermal excitation during an increase in temperature.

The valence and conduction bands play identical roles to those of the molecular orbitals HOMO (highest occupied molecular orbital) and LUMO (lowest unoccupied molecular orbital) in the theory of frontier molecular orbitals developed by Kenichi Fukui [197,198]. The difference between the energy of the HOMO orbital (E_H) and the energy of the LUMO orbital (E_L) corresponds to the HOMO-LUMO energy gap and generally represents the lowest possible excitation energy in a molecule. The energy of the HOMO-LUMO gap can tell us what wavelengths the compound can absorb. Conversely, the laboratory measurement of wavelengths absorbed by a compound can be used as a measure of the energy of the HOMO-LUMO gap. The energy of the HOMO-LUMO gap is calculated from the difference in the energies of the boundary orbitals as follows

$$E_{gap} = E_L - E_H \qquad 2.52$$

The occupation of different energy states by electrons follows the Fermi-Dirac distribution [196]. There is a characteristic energy, the Fermi level, is the energy level of the highest occupied level when the material is at a temperature of zero Kelvin. The Fermi level represents the chemical potential of organic systems. In the theory of boundary molecular orbitals, the Fermi level E_{FL}, which corresponds to the chemical potential μ, can be approximated by the relation [199]

$$E_{FL} = \frac{1}{2}(E_H + E_L) \qquad 2.53$$

The Fermi level of a material expresses the work required to add an electron to it, or also the work obtained by removing an electron from the material. Thus, the Fermi level is related to the work function which is defined as the minimum energy required to extract an electron from the Fermi level of a metal up to a point located at infinity outside the metal.

Parameters like the chemical potential, electronegativity, the hardness, softness and the electrophilicity index were determined through Koopman's Theory [200] and are defined and calculated by formulae found in literature [200-204]. According to this theory the ionization potential IP and electron affinity EA of the molecule are calculated using the following equations: IP = − E_H and EA = − E_L. The electronic chemical potential show the escaping tendency of electron from a stable system denoted

$$\mu = (IP + EA)/2 \qquad 2.54$$

The electronegativity calculated as the negative of chemical potential, $\chi = -\mu$ gives the power of molecule or atom to attract electrons. The global hardness, denotes resistance of an atom to a charge transfer and is calculated by

$$\eta = (IP - EA)/2 \qquad 2.55$$

The global softness is the reciprocal of the hardness, measures the tendency of an atom or molecule to receive electron. The global electrophilicity index is computed using hardness and chemical potential to quantify the accepting capacity of electrons by chemical species

$$\omega = \mu^2/2\eta \qquad 2.56$$

Good electrophilic species have high value of μ and ω, while nucleophilic species have small value

2.5.3 Methodology of the determination of the reorganization energy

A key parameters used in calculating the rate at which charge hop's or charge mobility is the reorganization energy λ, split into the internal reorganization energy λ_{int} which gives the structural change linking the ionic and neutral states of a molecule and external reorganization energy λ_{ext} gives the measure of the surrounding medium on charge transfer [205], λ_{int} by far exceeds λ_{ext} [206]. We therefore base our calculations on λ_{int}. λ_{int} for electron λ_e and hole λ_h transport can be calculated from the following equations. The electron and hole reorganization energies according to the Marcus model [207], are evaluated by the adiabatic potential-energy surface method

$$\lambda_e = (E_0^- - E_-^-) + (E_-^0 - E_0^0) \quad 2.57$$

$$\lambda_h = (E_0^+ - E_+^+) + (E_+^0 - E_0^0) \quad 2.58$$

E_+^0 and E_-^0 represent neutral species energy computed at the optimized geometries of its cationic and anionic forms respectively. E_-^- and E_+^+ are the energies of the anionic and cationic structures respectively, calculated with the optimized geometries of the cation and anion. E_0^0 E_0^+ and E_0^- are correspondingly the energies of the neutral, cationic and anionic species at the optimized neutral structure. Another key parameter decisive in charge transfer rate in organic semiconductors at the microscopic level is the transfer integral, V [208], which shows the ease of charge transfer between two interacting chains. V is linked with a given electronic level is associated to the energetic splitting of that level and goes from an isolated chain to a system of interacting chains. In organic polymers, the splitting of the HOMO and LUMO level ensuing from the interaction of adjacent chains in given directions gives the transfer integral used in describing electron and hole transport in these directions. In the weak-coupling regime the charge transfer rate K^{CT} is approximated by

$$K^{CT} = \frac{V^2}{\hbar}\left(\frac{\pi}{\lambda K_B T}\right)\exp(-\frac{\lambda}{4K_B T}) \quad 2.59$$

V is the transfer integral and the hole transfer integral given by $V_h = E_{homo} - E_{homo-1}$,and the electron transfer integral by $V_e = E_{lumo+1} - E_{lumo}$, $\hbar$ and K_B are fundamental constant, λ is the reorganization energy T is the temperature.

2.5.4 Methodology of the determination of the photovoltaic properties

In order to maximize OPVC device performance, it is crucial to understand the parameters that determine its operational capability. These parameters include, band gap E_g, open circuit V_{oc}, driving force ΔE_{LL}, reorganization energy λ, the isotropic polarizability α, first order hyperpolarizability β and anisotropy $\Delta\alpha$ of the organic material [, 138, 209, 210]

The power conversion efficiency (PCE) is a key quantity used to characterize the cell performance of solar cell and depends on the band gap E_g, the open circuit voltage V_{oc}, current density J_{sc}, and fill factor FF. The PCE indicates the ratio of the electrical power produced by the solar cell per unit area measured in watts, divided by the watts of incident light under certain specified conditions called “standard test conditions [211]. The open circuit voltage will be calculated using the Scharber model [212-215]

$$V_{oc} = \frac{1}{e}|E_H^D - E_L^A| - E_b \qquad 2.60$$

Where e is the elementary charge, E_H^D is the HOMO energy of the donor, E_L^A is the LUMO energy of the acceptor and customary to agreed experimental laboratory value E_L^A = -4:026 eV for the acceptor PCBM [216], E_b the exciton binding energy for the electron and hole with a value ranging from 0.1 to 1V, we take the value of 0.3V as reported in other literature as the value is the loss factor associated to the heterojunction design [217].

The energy difference between the LUMO of the donor and acceptor ΔE_{LL}, called the driving force is an important factor that enhances the PCE of OPVCs, it is expressed as in [218]. The driving force is a determining factor for exciton dissociation to free charges at the D-A heterojunction.

$$\Delta E_{LL} = E_L^D - E_L^A \qquad 2.61$$

The free charges produced by exciton dissociation at the D-A heterojunction must travel through the active layer to reach the electrodes where they are collected to produce photocurrent. Charge carrier mobility estimated through the reorganization energy is therefore important in determining device efficiency and method to calculate it shown in **section 2.4.2.** The nonlinear optical properties viz; the isotropic polarizability α, first order hyperpolarizability β and anisotropy of the polarizability $\Delta\alpha$ are computed as shown in **section 2.4.1** and give the extent of the delocalization of intramolecular charge of donor electrons in the OPVC [210].

2.6 Conclusion

In this chapter, we presented the modeling methods based on quantum mechanics used in the study of the desired properties of the GNRs. These methodologies which includes the RHF, ab initio method and the B3LYP, and BPBE DFT methods in modelling the properties of the GNRs were well explicated using the 6−31+G(d, p) base set. This modeling methods were used to determine the nonlinear optical, photovoltaic, thermodynamic and electronic properties of the GNRs. In the next chapter, we present the modeled systems and analyze the molecular simulation results obtained.

CHAPTER 3
RESULTS AND DISCUSSION

3.0 Introduction

In this chapter, the results obtained from the computations carried out in the course of this research are scrutinized. The results and their discussion are presented according to the various partitions of this work, for better comprehension. We will in particular present and analyze the properties of GNRs. We exploit the DFT and ab initio molecular modelling methods to predict the properties of the system using a common basis set 6-31+g(d,p). We will present, analyze and contrast the numerical simulated results of the nonlinear optical, charge transport and photovoltaic properties of some selected graphene nanoribbons and their metalated counterparts, namely: phenanthrene, azulene and perylene. This chapter is divided into eight sub sections; section one looks at the optimized structures of the GNRs, while section two, three and four will present the effects of metalating GNRs on their nonlinear optical properties, electronic properties and quantum descriptors respectively, while section five will study the effects of metalating GNRs on the organic photovoltaic properties then section six and seven will analyze the mechanical stability of the studied molecules and its thermodynamic properties respectively and lastly section eight will analyze the vibrational spectra of the GNRs and their metal derivatives. We culminate with a last section dedicated to the conclusion.

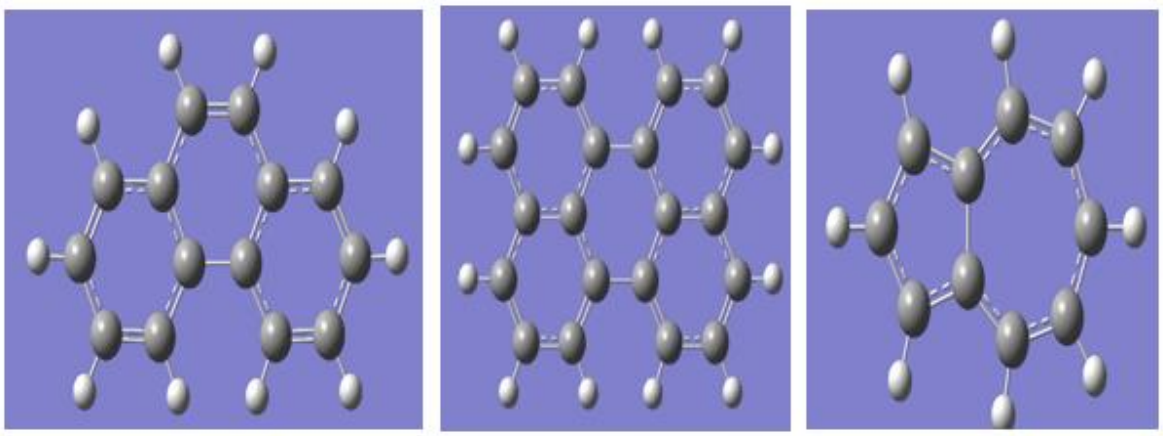

Fig 3.1 Optimized structures of phenanthrene, perylene, azulene respectively, using RHF, B3LYP and BPBE methods together with the 6-31+g(d,p) basis

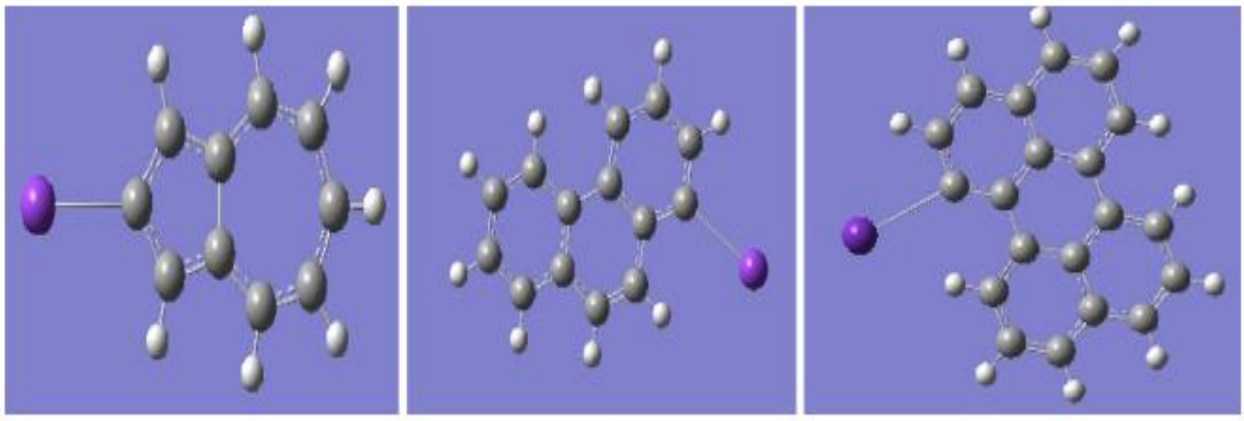

Fig 3.2 Optimized structures of metalated azulene, phenanthrene and perylene respectively, using RHF, B3LYPand BPBE methods together with the 6-31+g(d,p) basis

3.1 Optimized structure of the studied GNRs

The optimized geometric structure obtained from calculations are shown in fig. 3.1. and fig. 3.2 above. As can be observed, the optimized structure of the metalated GNRs are planar. The GNRs as well as their metalated counterpart are shown. In calculation, absence of results for perylene at the B3LYP and BPBE method was due to non-convergence of the simulation due to the high symmetry of perylene.

3.2 Effect of metalation on the nonlinear optical properties of GNRs

The calculated values of the average Polarizability, hyperpolarizability, total dipole moment and anisotropy are depicted in table 3.1, are important parameters that aid to appreciate the Non-Linear Optical (NLO) behavior of a molecule have been evaluated by numerous researchers, we have also calculated these properties in this work. Their NLO behavior is an important parameter in drug design, pharmacology where they serve in depiction of quantitative structural analysis relationship (QSAR) [219]. The parameters are useful in shaping the structure, dynamical orientation thermodynamics properties of materials and are therefore of real experimental importance. The values of the total dipole moment, average polarizability and anisotropy in all the studied GNRs are greater in all the GNRs metalated molecules than in the starting molecule at all level of theory. All GNRs metal derivatives have dipole moment which are greater than that of urea 1.5256D obtained in literature [200, 220]. Urea is a prototypic molecule used in comparative analysis in nonlinear optics. This shows that metalation could be of future relevance in the design of nonlinear optical devices. The dipolarity induced by strong alkali metal donor on the highly delocalized pi electron system

has heighten the hyperpolarizability; a determining factor for NLO activity of the system which is of essence in shaping a system's properties. The metal donor atom induces polarizability through intramolecular charge transfer which increases the hyperpolarizability. Comparing our hyperpolaribility with the prototypic push-pull molecules, *para*-nitroaniline (p-NA) and urea with hyperpolarizabilities respectively, $5.01\times10^{-50}c^3m^2/J^2$, and $1.38\times 10^{-51}c^3m^2/J^2$ [200, 220, 221], it is observed that all the studied metal GNR have hyperpolarizabilities greater than the two prototypic molecules. The metalated counterparts could therefore suggest potential applications of these molecular systems in the development of nonlinear optical materials. The result obtained at the B3LYP/6-31+g(d,p) level of theory for azulene confirms the experimental value of the dipole moment for this molecule already obtained in literature [222]. The values of the average polarizability, and anisotropy for both the starting GNR and the metal derivative are higher in the two DFT methods than that of the ab initio method; RHF but for some few cases. This can be attributed to the absence of electron correlations effect. The dipole moment follows the reverse trend. The value of the hyperpolarizability for the ab initio method is greater than the two DFT methods or functional for all the starting molecules but follows the reverse trend for all the metalated GNR, so the same cause doesn't necessarily produce the same effect.

Table 3.1a Nonlinear optical properties of the virgin GNRs obtained using RHF, B3LYP and BPBE methods together with the 6-31+g(d,p) basis

Properties	phenanthrene			Azulene			Perylene
	RHF	B3LYP	BPBE	RHF	B3LYP	BPBE	RHF
$\mu(D)$	0.0118	0.0142	0.0225	1.60	1.09	0.99	0.00
$\alpha\ (c^2m^2/J)\times 10^{-39}$	2.57	2.80	2.86	2.03	2.11	2.14	3.81
$\Delta\alpha(c^2m^2/J)\times 10^{-40}$	14.8	17.5	18.6	1.28	13.07	1.35	1.70
$\beta(c^3m^2/J))\times 10^{-52}$	11.3	5.40	1.94	146.17	80.82	66.85	00.0006

Table 3.1b Nonlinear optical properties of the GNRs metal derivatives obtained using RHF, B3LYP and BPBE methods together with the 6-31+g(d,p) basis

Properties	k-phenanthrene			k-azulene			Rb-perylene		
	RHF	B3LYP	BPBE	RHF	B3LYP	BPBE	RHF	B3LYP	BPBE
$\mu(D)$	12.08	10.48	10.34	11.23	10.18	10.08	13.52	11.99	9.75
$\alpha\ (c^2m^2/J) \times 10^{-39}$	2.97	3.71	3.93	2.45	3.01	3.13	4.18	5.21	5.21
$\Delta\alpha(c^2m^2/J) \times 10^{-40}$	16.4	24.2	26.9	3.27	24.26	1.84	3.21	2.22	9.33
$\beta(c^3m^2/J)) \times 10^{-52}$	8.32	58.45	80.66	950.98	5594.9	7318.72	752.29	8738.29	6756.00

3.3 Energy and density of states (DOS) analysis on the effect of metalation on GNRs

Frontier molecular orbitals (FMOs), which are the highest occupied molecular orbital (HOMO) and the lowest unoccupied molecular orbital (LUMO), are very important quantum chemical parameters because they play a key role in the electric, chemical and optical properties of compounds. The values of the highest occupied molecular orbital (HOMO) and lowest unoccupied molecular orbital (LUMO) were determined directly.

The gap energy indicates that the phenanthrene, azulene and perylene are dielectric as they have a band gap greater than 3eV at all level of theory [98, 223]. The RHF method produces the greatest gap energy for any of the GNR be it metalated or not, this is due to the absence of electron correlation that isn't incorporated in the ab initio method. The metalated GNRs at the BPBE method produces the lowest gap energy amongst all the molecules. When all the GNRs are metalated their band gap reduce, with some GNRs becoming superconductors like K-phenanthrene, Rb-perylene and K-azulene at the BPBE/6-31+g(d,p) level of theory with many industrial applications in computer circuitry and charge transfer.

The isosurfaces of the HOMO and LUMO of the GNRs and the metal derivatives are presented in fig.3.3 visualized using gauss view 5.0 [190]. For phenanthrene the LUMO and HOMO are spread out through the entire molecule. This spread explain the reason for its low dipole moment and hyperpolaribility. As its concern k-phenanthrene, the LUMO and the HOMO are mostly located on the metal moiety with the highest density of charge observed on the LUMO.

Metalation is seen to show significant charge transfer (CT) for phenanthrene as there is charge separation. Azulene shows a similar trend as phenanthrene with almost an even spread of the HOMO and LUMO, however, the HOMO of its metal derivatives is found on the metal moiety while the LUMO is found away from the metal moiety, showing very significant CT and consequently a high hyperpolarizability. The zero dipole moment obtained for perylene is well observed with a complete well spread HOMO and LUMO, CT is near zero. The HOMO of the metal derivative is located mostly on the metal moiety while its LUMO is evenly spread.

The total density of state (DOS) spectrum for the studied molecules obtained using the RHF/6-31+g(d,p), and B3LYP/6-31+G(d,p) level of theory in gas phase is presented in Fig. 3.4. The DOS spectrum shows that the band gap is large with the RHF/6-31+g(d,p) level of theory and small at the B3LYP/6-31+G(d,p) level of theory, indicating that inclusion of electron correlation effects reduces band gap. The role of the various HOMO and LUMO groups of molecular orbitals are presented: in green for HOMO orbital and red for LUMO orbital. Low-band gap organics serve myriad role of electron donors, hole transport, exciton generation, migration and recombination. The occupation of different energy states by electrons follows the Fermi-Dirac distribution [224]. There is a characteristic energy, the Fermi level, which fixes, when the material is at a temperature of zero kelvin, the energy level up to which we find the electrons, that is, the energy level of the highest occupied level. The Fermi level represents the chemical potential of organic systems. Its positioning in the diagram of bands of energy is related to how bands are busy. In the theory of boundary molecular orbitals, the Fermi level E_{FL} to which correspond the chemical potential is given by

$$E_{FL} = \frac{1}{2}(E_L + E_F) \qquad 3.1$$

The Fermi level of a material expresses the work required to add an electron to it, or also the work obtained by removing an electron. Thus, the Fermi level is related to the work output which is defined as the minimum energy required to extract an electron from the Fermi level of a metal up to a point located at infinity outside the metal.

The Fermi level is the least increased in energy when an electron is added to a material. The Fermi energy is higher for the metalated GNRs than for the virgin counterparts except at the RHF method which shows an opposite trend. The virgin GNRs have a higher value for the Fermi energy at the RHF method than at the two density functional methods at all level of theory.

3.3 Effect of metalation on the quantum molecular descriptors

Parameters like the chemical potential, electronegativity, the hardness, softness and the electrophilicity index were determined through Koopman's Theory [200] and are defined and calculated by formulae found in literature [200-204]. The electronic chemical potential show the escaping tendency of electron from a stable system as given in equation (2.54). The electronegativity calculated as the negative of chemical potential gives the power of molecule or atom to attract electrons. The global hardness, denotes resistance of an atom to a charge transfer and is given equation (2.55). The global softness is the reciprocal of the hardness, is tendency of an atom or molecule to receive electron. The global electrophilicity index is computed using hardness and chemical potential to quantify the accepting capacity of electrons by chemical species denoted by equation (2.56). Good electrophilic species have high value of μ and ω, while nucleophilic species have small value. The values of the chemical potential is larger for the starting molecule than for the metal GNR except at the RHF method as the value of the chemical potential reduces with metal substitution. The largest values for the chemical potential are obtained at the RHF than for the two DFT methods. The chemical hardness (η) defines the chemical reactivity and stability of a molecule. The greater the chemical hardness value the more stable the chemical species. Molecule with small chemical hardness are therefore more reactive. Reactivity is seen to increase with metalation as the value of the hardness reduces when metal is added to the investigated GNR, and the starting materials are therefore more stable than their metal counterparts. The HF method has the highest value for the hardness all cases than in the two DFT methods. The electrophilicity index was considered in this research along with chemical potential, its measure the propensity of a chemical species to accept electron. Thus, a molecule with high electrophilicity index indicates good electrophilic behavior, while a low value of indicate a good nucleophile. These quantum molecular descriptors are shown in table 3.2. The electrophilic index is seen to reduce upon metalation at all level of theory except for phenanthrene at the RHF level, this indicates that metalated GNRs tend to be better nucleophile while the starting GNR are better electrophile. Electron correlation effects are seen to lower the electrophilic index evident in the two DFT methods than RHF method.

The hyperpolarizability and the energy gap is inversely proportional and corroborates earlier results found in literature [225, 226], due to significant extension of the conjugation of pi-electrons as a result of intramolecular charge transfer across the donor- acceptor bridge.

The mechanical stability of the GNRs and their metal counterparts can be visualized through the parameter of hardness seen in table 3.2. Stability is an invaluable tool in the construction of optoelectronic devices. The mechanical stability decreases with the adding of metal as seen in the decrease in value of the hardness upon metalation at all level of theory. This research work has proven metalation has a positive impact on the optoelectronic properties of GNRs but stability an invaluable tool in the production of optoelectronic device is proven counterproductive with the same process. Molecular orbitals analysis also disclose very high interaction between the carbon atom and the 3s state of potassium (K-3s), and the 5s state of Rubidium state (Rb-5s), hybridization occurring amidst the K and C atoms decreases the stability of the GNR than in the starting molecule.

Table 3.2a Gap (eV), chemical potential (μ), absolute hardness (η), softness (S), electronegativity (χ) and electrophilic index (ω) of the virgin GNRs obtained using RHF, B3LYP and BPBE methods together with the 6-31+g(d,p) basis

Properties	phenanthrene			Azulene			Perylene
	RHF	B3LYP	BPBE	RHF	B3LYP	BPBE	RHF
HOMO (eV)	-7.84	-6.02	-5.35	-7.09	-5.56	-4.86	-6.75
LUMO (eV)	1.88	-1.36	-2.01	1.05	-2.27	-2.80	1.02
Gap(eV)	9.71	4.67	3.34	8.15	3.29	2.06	7.77
E_{FL}(eV)	-2.98	-3.69	-3.68	-3.02	-3.92	-3.83	-2.87
EA(eV)	-1.88	1.36	2.01	-1.05	2.27	2.80	-1.02
IP(eV)	7.84	6.02	5.35	7.09	5.56	4.86	6.75
$\mu(eV)$	2.98	3.69	3.68	3.01	3.91	3.83	2.87
η	4.86	2.33	1.67	4.07	1.645	1.03	3.885
S	0.21	0.43	0.60	0.25	0.60	0.97	0.26
χ	-2.98	-3.69	-3.68	-3.01	-3.915	-3.83	-2.865
ω	0.913	2.92	4.05	1.11	4.65	7.12	1.06
ΔE_{int}(eV)	-	-	-	-	-	-	-

Table 3.2b Gap (eV), chemical potential (μ), absolute hardness (η), softness (S), electronegativity (χ) and electrophilic index (ω) of the metalated molecules obtained using RHF, B3LYP and BPBE methods together with the 6-31+g(d,p) basis

properties	k-phenanthrene			k-azulene			Rb-perylene		
	RHF	B3LYP	BPBE	RHF	B3LYP	BPBE	RHF	B3LYP	BPBE
HOMO (eV)	-6.45	-4.53	-3.57	-5.92	-4.31	-3.68	-5.49	-4.23	-3.26
LUMO (eV)	-0.42	-1.73	-1.69	-0.32	-1.61	-1.69	-0.48	-1.93	-2.15
Gap(eV)	6.02	2.80	1.87	5.60	2.71	1.99	5.01	2.30	1.10
E_{FL}(eV)	-3.44	-3.13	-2.63	-3.12	-2.96	-2.69	-2.99	-3.08	-2.71
EA(eV)	0.42	1.73	1.69	0.32	1.61	1.69	0.48	1.93	2.15
IP(eV)	6.45	4.53	3.57	5.92	4.31	3.68	5.49	4.23	3.26
$\mu(eV)$	3.43	3.13	2.63	3.12	2.96	2.69	2.99	3.08	2.71
η	3.02	1.4	0.94	2.8	1.35	1.00	2.51	1.15	0.56
S	0.33	0.71	1.06	0.36	0.74	1.01	0.40	0.87	1.80
χ	-3.44	-3.13	-2.63	-3.12	-2.96	-2.69	-2.99	-3.08	-2.71
ω	1.95	3.50	3.68	1.74	3.25	3.64	1.78	4.12	6.59
ΔE_{int}(eV)	-1195.9	-1197.4	-1197.2	-1196.0	-1197.4	-1197.7	-45.2	-	-

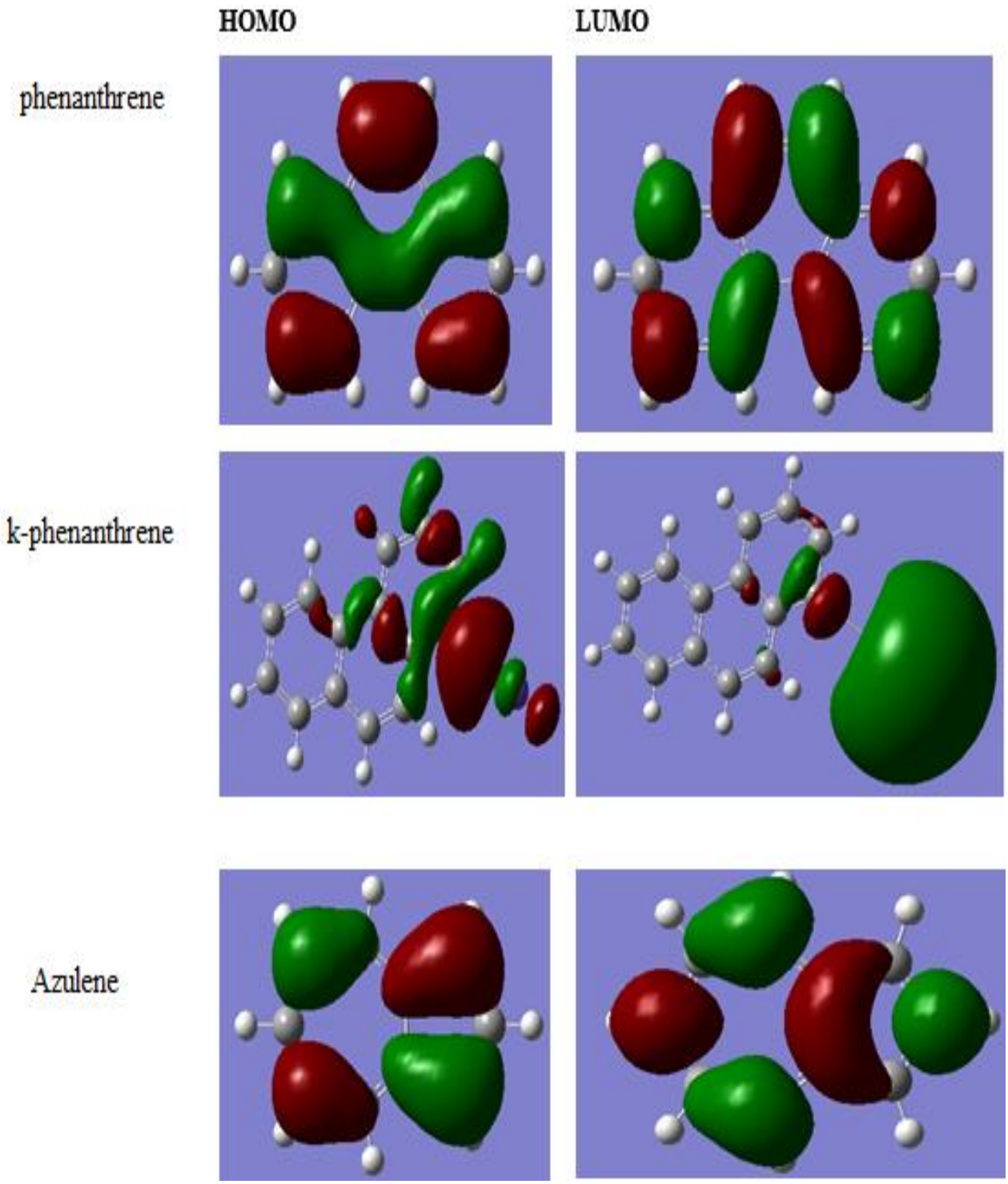
HOMO
LUMO
phenanthrene
k-phenanthrene
Azulene

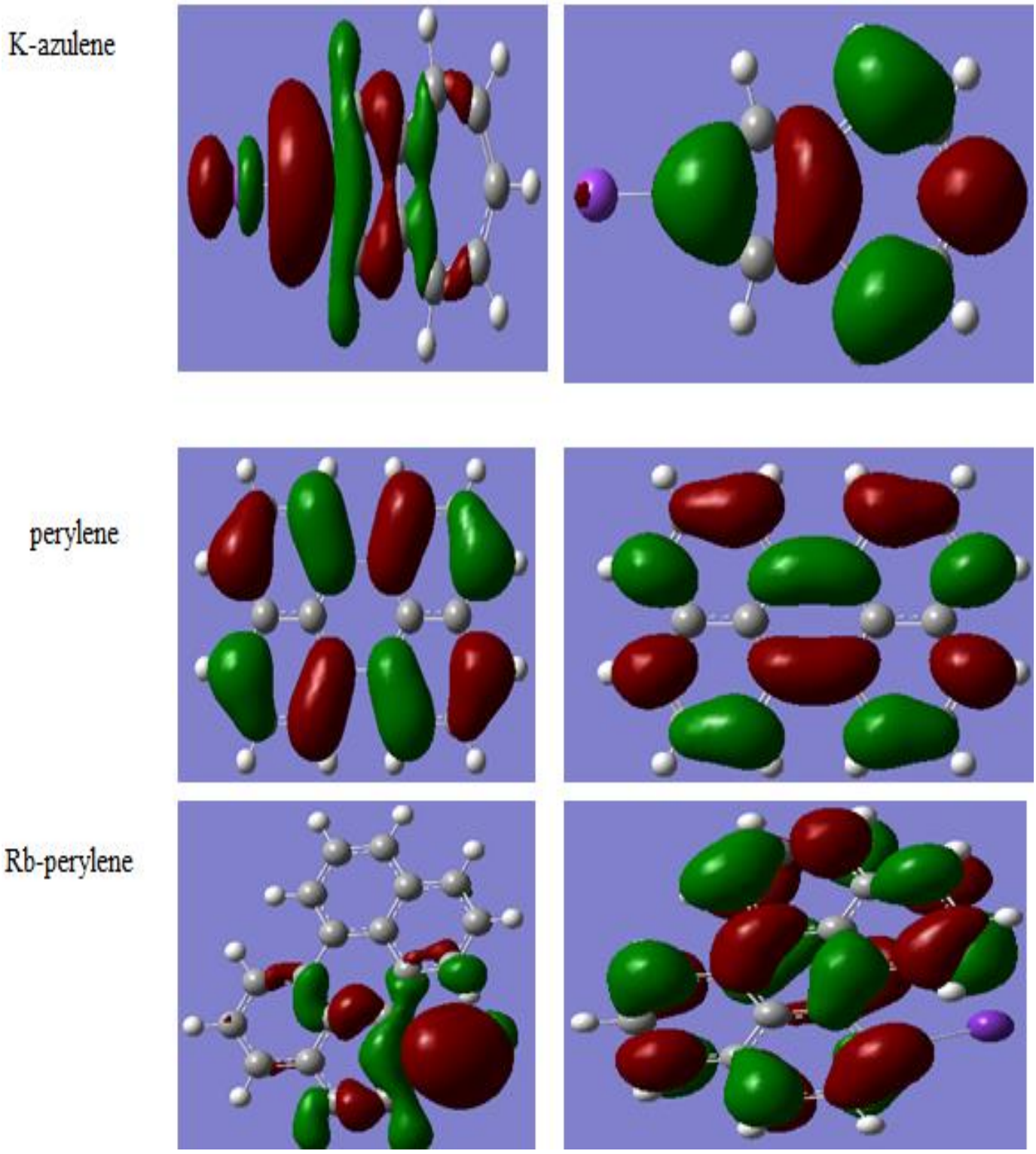

Fig 3.3 Isosurfaces of the HOMO and LUMO of GNRs and their metal derivatives

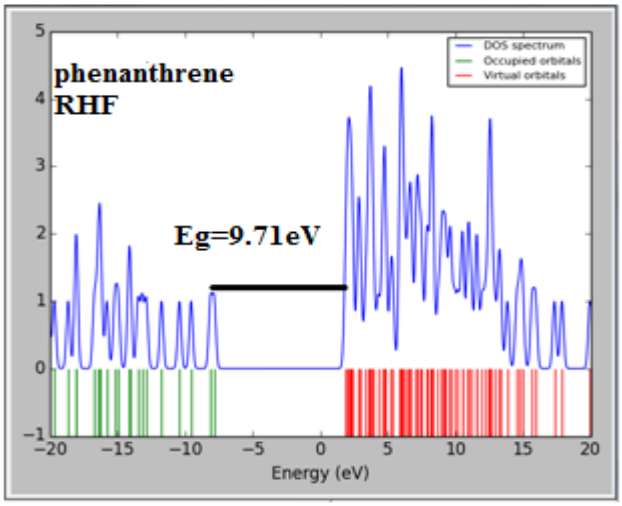
phenanthrene
RHF
Eg=9.71eV
DOS spectrum
Occupied orbitals
Virtual orbitals
Energy (eV)

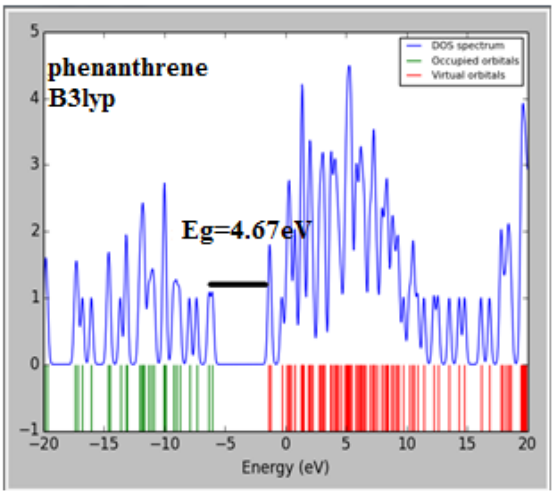
phenanthrene
B3lyp
Eg=4.67eV
DOS spectrum
Occupied orbitals
Virtual orbitals
Energy (eV)

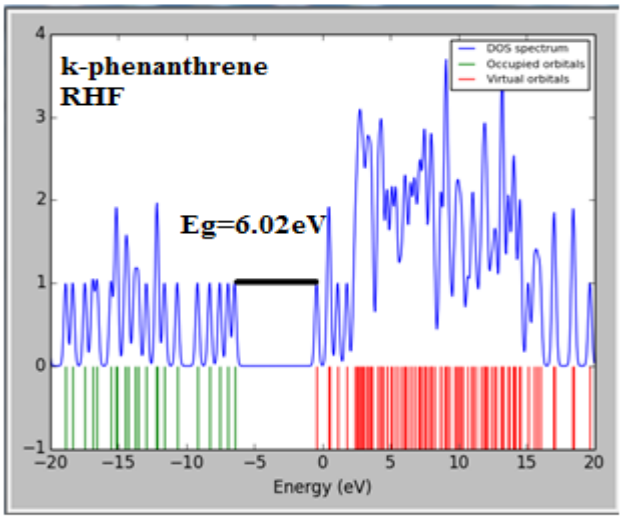
k-phenanthrene
RHF
Eg=6.02eV
DOS spectrum
Occupied orbitals
Virtual orbitals
Energy (eV)

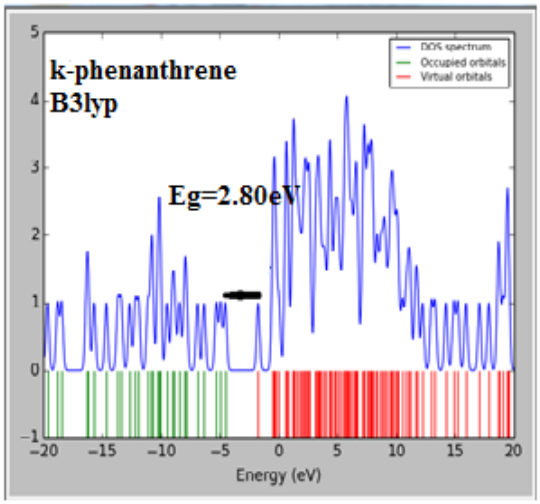
k-phenanthrene
B3lyp
Eg=2.80eV
DOS spectrum
Occupied orbitals
Virtual orbitals
Energy (eV)

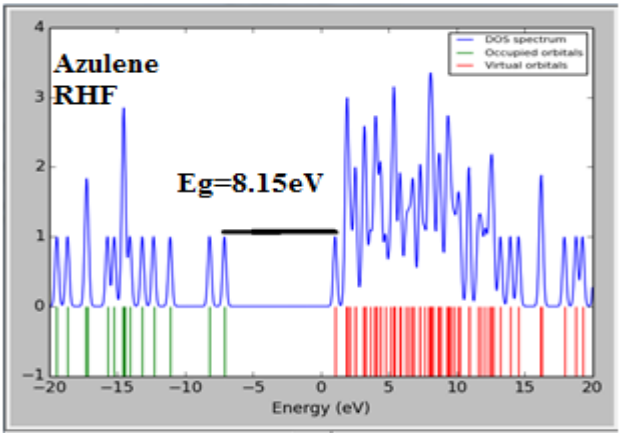
Azulene
RHF
Eg=8.15eV
DOS spectrum
Occupied orbitals
Virtual orbitals
Energy (eV)

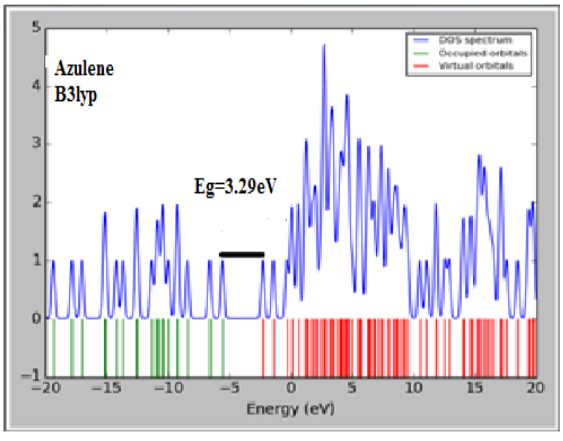
Azulene
B3lyp
Eg=3.29eV
Energy (eV)

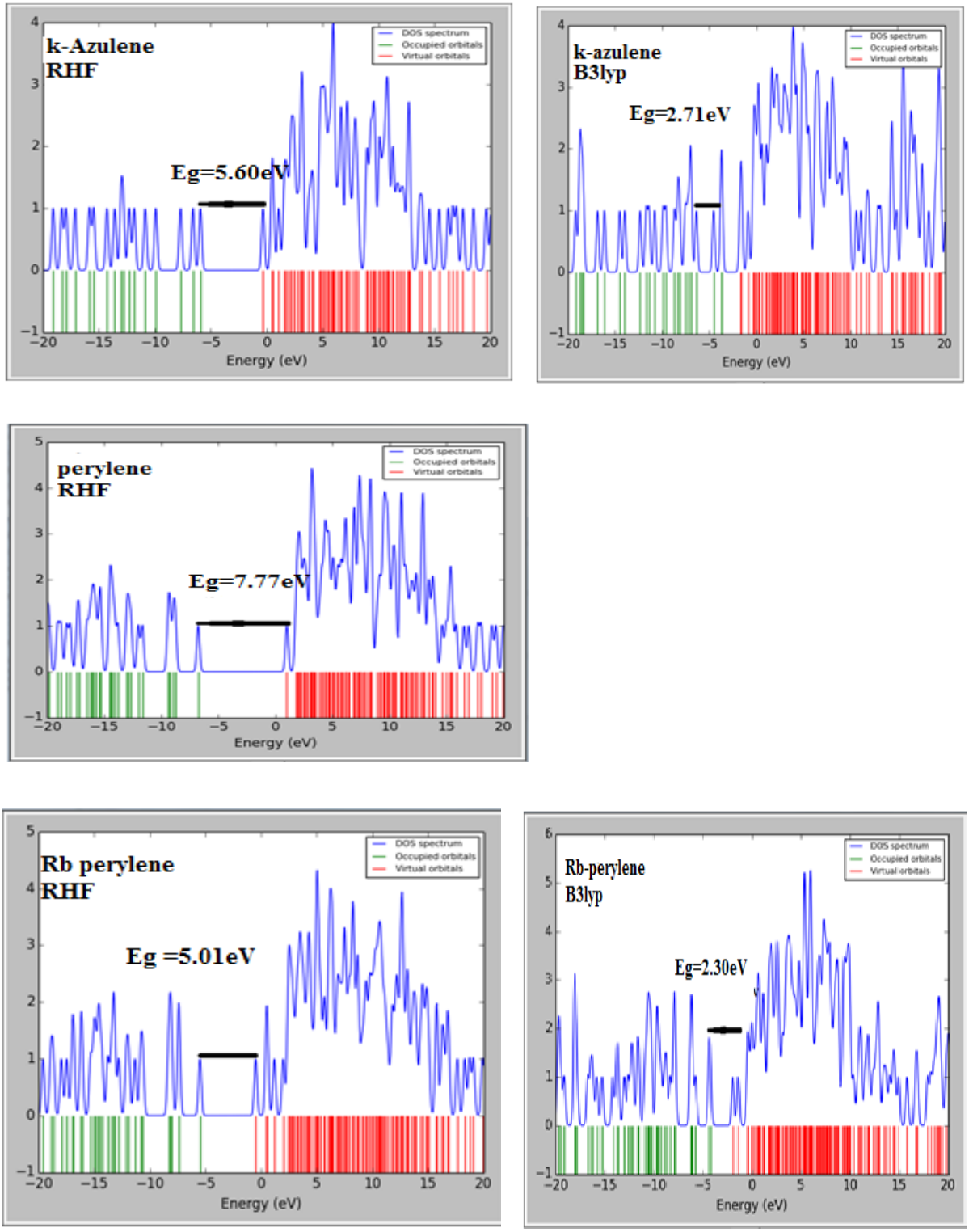

Fig 3.4 Density of states (DOS) for phenanthrene, azulene, perylene, and its metal derivatives showing band gaps obtained at the HF and at the B3LYP methods

3.4 Effect of metalation on some graphene nanoribbons for potential application as donor in bulk heterojunction (BHJ) organic photovoltaic cells with PCBM as model acceptor

3.4.1 Open circuit voltage, driving force band gap, and density of state analysis

These calculated values determining photovoltaic performance of the GNRs and their metalated counterparts obtained from optimized geometry using the RHF, B3LYPand BPBE method together with the 6-31+g(d,p) are summarized respectively in table 3.3 and 3.4 below. The dashed entries in table 3.3 show non converging results.

The open-circuit voltage V_{oc}, is the peak voltage across an OPV device. V_{oc} is obtained when the photogenerated current is balanced to zero, a state called flat band condition. The V_{oc} value is a useful parameter to indicate solar cell performance or power conversion efficiency of a solar cell device of type Bulk Heterojunction (BHJ). BHJ solar cell consist of a blend of electron donor and acceptor materials cast as a mixture as shown in fig. 1.3 above. Then acceptor chosen is the most widely used acceptor PCBM [216]. Enhancing V_{oc} is important in boosting the PCE of the solar cell.

Table 3.3 Organic photovoltaic properties of the starting GNRs obtained using the RHF, B3LYP, and BPBE method using the 6-31+g(d,p) basis

Property	Phenanthrene			Azulene			Perylene		
	RHF	B3LYP	BPBE	RHF	B3LYP	BPBE	RHF	B3LYP	BPBE
E_L^D/eV	1.88	-1.36	-2.01	1.05	-2.27	-2.80	1.02	-	-
E_H^D/eV	-7.84	-6.02	-5.35	-7.09	-5.56	-4.86	-6.75	-	-
E_{gap}^D/eV	9.71	4.67	3.34	8.15	3.29	2.06	7.77	-	-
E_L^A/eV	-4.026	-4.026	-4.026	-4.026	-4.026	-4.026	-4.026	-	-
V_{oc}/V	3.514	1.694	1.024	2.764	1.234	0.534	2.424	-	-
ΔE_{LL}/eV	5.906	2.666	2.016	5.076	1.756	1.226	5.046	-	-

All the virgin GNRs have good V_{oc} values above the 1V minimum value for the optimal performance of OPVCs [227], except for azulene at the BPBE/6-31+g(d,p) level of theory, with the highest value obtained by phenanthrene at the RHF/6-31+g(d,p) level of theory. Electron correlation effects help to lower the values of V_{oc} as the values at the B3LYP/6-

31+g(d,p) and BPBE/6-31+g(d,p) level of theory are lower than at the RHF/6-31+g(d,p) level of theory. The computed V_{oc} values except for azulene at the BPBE/6-31+g(d,p) level of theory are good for practical values for OPVCs as stated in literature for devices that have reasonable photocurrents [228].

Table 3.4 Organic photovoltaic properties of the metalated GNRs obtained using the RHF, B3LYP, and BPBE method using the 6-31+g(d,p) basis

property	k-phenanthrene			k-azulene			Rb-perylene		
	RHF	B3LYP	BPBE	RHF	B3LYP	BPBE	RHF	B3LYP	BPBE
E_L^D/eV	-0.42	-1.73	-1.69	-0.32	-1.61	-1.61	-0.48	-1.93	-2.15
E_H^D/eV	-6.45	-4.53	-3.57	-5.92	-4.31	-3.68	-5.49	-4.23	-3.26
E_{gap}^D/eV	6.02	2.80	1.87	5.60	2.71	1.99	5.01	2.30	1.10
E_L^A/eV	-4.026	-4.026	-4.026	-4.026	-4.026	-4.026	-4.026	-4.026	-4.026
V_{oc}/V	2.124	0.204	0.156	1.594	-0.016	0.046	1.164	-0.096	0.466
ΔE_{LL}/eV	3.606	2.296	2.336	3.706	2.416	2.416	3.546	2.096	1.876

The computed values of V_{oc} for the metalated GNRs at the two DFT methods are less than the 1V required minimum value required for OPVC operation [227] but attain this target at the RHF method for all the three molecules. K- Phenanthrene has the greatest value for V_{oc} at each level of theory than any of the rest two molecules except for Rb-perylene at the BPBE/6-31+g(d,p) level of theory. Careful examination indicates that V_{oc} has a near inverse relationship trend with the hyperpolarizability as indicated in fig. 3.5 for the metalated GNRs suggesting increased intramolecular charge transfer may diminish V_{oc}. The computed V_{oc} values for the metalated GNRs especially at the two DFT levels are smaller than the practical values for OPVCs stated in literature for devices that have reasonable photocurrents [228]. However, hope to improve these values could dwell on other determining factors for V_{oc}, such as: donor energy levels, chemical potential gradients, light intensity, morphology (rough or smooth surface), external fluorescence, recombination of charge-carrier, light-source, cell temperatures, charge-carrier recombination, Fermi level pinning [229, 230]. Comparatively, the virgin GNRs perform better than GNRs in the area of V_{oc}.

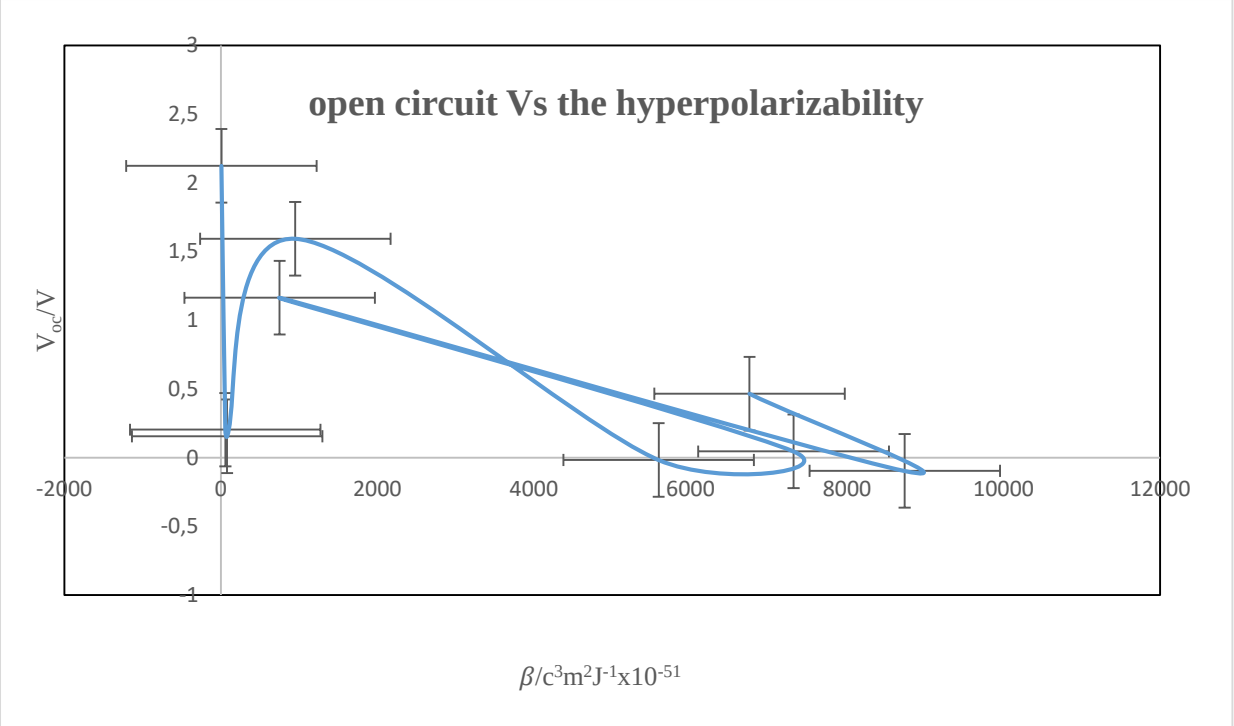

Fig.3.5 Open circuit voltage against the hyperpolarizability for K-phenanthrene, K-azulene and Rb-perylene

A salient factor limiting the PCE of OPVCs is large energy loss, largely ascribed to the relatively large non-radiative recombination loss caused by the significant energy-level offset between the donor and acceptor as well as the extremely low electroluminescence quantum efficiency of organic photovoltaic materials. The energy-level offset between D-A interface cause exciton dissociation and is a vital step in OPVC functioning. This is measured through the driving force ΔE_{LL} and should be greater than 0.30 eV in order to provide sufficient exciton dissociation [138, 218]. The driving force sets up electrostatic forces at the D-A interface, and when appropriately chosen, the electric field generated, can split the excitons into holes and electrons efficiently. From table 3.3, it is observed that all the virgin GNRs have ΔE_{LL} greater than the required 0.3V minimum, with the greatest value shown by phenanthrene at the 6-31+g(d,p) level of theory. In general the absence of electron correlation effects heightens the value of driving force for the virgin GNRs. From table 3.4 we remark that all the metalated GNRs have a ΔE_{LL} value that is above the 0.3eV requirement, with k-azulene having the highest value of 3.706eV. k-azulene equally shows the best results in exciton dissociation than the other two GNRs metal derivatives at any level of theory. Inclusion of electron correlation effects are seen to diminish the driving force for exciton dissociation for the metal GNRs, a similar trend is shown by the virgin GNRs. The virgin GNRs in consideration of the driving

force show a better performance than the metalated GNRs. After exciton dissociation the electrons are conveyed by the acceptor material with higher electron affinity in the BHJ and the hole by the donor material with lower ionization potential [216, 231,232]. However, the efficiency of this process is greatly hampered by recombination of charges and organic imperfections trapping.

One of the major impediments to get high PCE is the limited spectral overlap between the solar spectrum and its absorption by the photoactive donor material, consequently giving a small valued photocurrent. Actually, the total solar photon flux of approximately 62% is at wavelengths $\lambda > 600$ nm with almost 40% in the red and near-infrared (NIR) spectrum at $600 < \lambda < 1{,}000$ nm. Nonetheless, the optical band gap of most organic photoactive materials is not optimized with respect to the solar spectrum, in which only 20–30% of solar spectrum can be absorbed [,127, 211]. This indicate that we need to research new materials that will absorb NIR radiation, and efficiently transform the absorbed photons into electricity, such materials are those with band gap below 1.9eV [21, 211]. All the studied virgin GNRs have band gaps far greater than the 1.9eV below requirement with the greatest value shown at the ab initio method than for the DFT methods for each molecule. They therefore show poor performance in this area.

The band gap, a representative signature in photovoltaic materials, for the studied metalated GNRs stands at value of below 1.9eV only at the BPBE/6-31+g(d,p) level of theory for all three metal GNRs, with the least value obtained with Rb-perylene of 1.10eV which could in theory guarantee the highest sunlight harvest efficiency as it has the greatest overlap with the sun spectrum. Rb-perylene also give the smallest band gap than any of the molecules at all level of theory. The RHF and the B3LYP method gives a band gap greater than the 1.9eV required value for the operation of OPVCs. Non-inclusion of electron correlation effects in the RHF method widens the band gap. Small band gap OPVC materials optimize photon harvesting as they have great overlap with the sun spectrum. On comparing the band gap of these molecules with their inorganic counterparts, bearing in mind that functional inorganic photovoltaic devices operate within a band gap range of 0.7 eV to 2.5 eV [216], we observe they can be classified as small band gap material. The metal GNRs perform better than virgin GNRs in OPVCs functioning in the domain of band gap. The DOS shown in fig 3.4 show the relative large band gap for the virgin GNRs than the metalated GNRs. In BHJ type of OPVC, low-band gap organics serve myriad role of electron donors, hole transport, exciton generation, migration and recombination.

According to the criteria set to approximate the value of the PCE of an OPV by Scharber, in literature [232, 233], by matching the band gap with the LUMO level of the donor, accordingly a material having band gap smaller than 1.74 eV together with a $E_{Lumo} < -3.92\ eV$, should generate a PCE of greater than 10%. Therefore Rb-perylene at the BPBE/6-31+g(d,p) level of theory, with a theoretical band gap of 1.10eV and E_{Lumo} =-2.15eV could on such criteria enjoy a PCE of about 10%. Such efficiency realized in this research could in theory, get this organic polymer a step closer to commercialization, and is a benchmark research finding and motivation for experimental consolidation of our theoretical work.

The band gap and the hyperpolarizability as shown in fig.3.6 for the metal derivative, show also a near inverse relationship, interestingly giving a similar shape to that portrayed by the V_{oc} and β. This inverse proportionality corroborates earlier results found in literature [225], due to significant extension of the conjugation of pi-electrons as a result of intramolecular charge transfer across the donor- acceptor bridge. The functioning of the OPVC has a stage by stage associated energy loss mechanism, such as non-absorbed photons, exciton decay as it diffuses to the D-A interface, geminate recombination of the bound electron hole pair as it disassociates into free carriers, and bimolecular recombination as the free carriers transport towards the electrodes for collection. The interrelatedness of these stages can't be underestimated. Improving a single stage could but not necessarily lead to the overall improvement of its functionality.

3.4.2 Reorganization energy and charge mobility for OPVC activity

In designing novel solar cell devices there is need of linking charge transport properties and the molecular structure of the conjugated material. Reorganization energy of a molecular system cast a profound understanding of structure and charge transfer property relationship. The hole reorganization energy is key in determining charge carrier mobility in the donor of the OPVC as it conveys holes after exciton dissociation and influences parametric hole coupling. High hole mobility for charge-carrier leads to high short circuit current, and is a central parameter for OPV materials as it impacts, extraction and recombination dynamics of charge. It's factual that low reorganization energy leads to a high charge mobility [234-236]. Of interest here is the internal reorganization energy as the external reorganization is ignored due to the stiff environment. Small value of internal reorganization energy is associated with higher solid-state charge carrier mobility in an isolated molecule

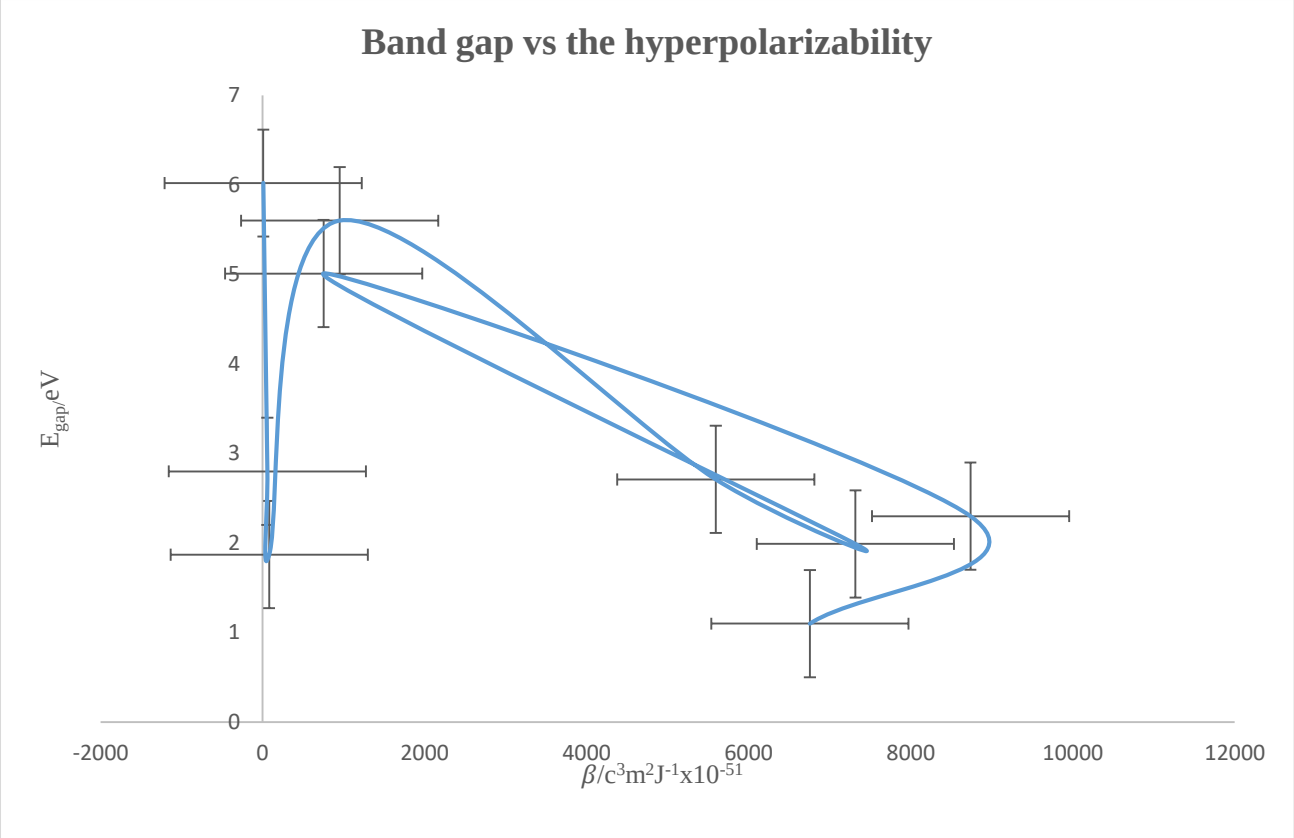

Fig.3.6 Band gap against the hyperpolarizability for K-phenanthrene, K-azulene and Rb-perylene

Table 3.5a Charge transport properties of the virgin GNRs

Molecular properties	phenanthrene			azulene			perylene
	RHF	B3LYP	BPBE	RHF	B3LYP	BPBE	RHF
V_h	0.134	0.15	0.14	0.55	0.51	0.50	1.00
V_e	0.06	0.06	0.07	0.42	0.44	0.43	0.40
λ_e	0.313	0.250	0.253	0.612	0.588	0.544	0.440
λ_p	0.421	0.212	0.259	0.364	0.639	0.257	0.570

Table 3.5b Charge transport properties of the GNRs metal derivatives

Molecular properties	k-phenanthrene			k-azulene			Rb-perylene		
	RHF	B3LYP	BPBE	RHF	B3LYP	BPBE	RHF	B3LYP	BPBE
V_h	0.24	0.19	0.36	0.33	0.17	0.01	0.94	0.36	0.35
V_e	0.43	0.62	0.28	0.39	0.26	0.06	0.49	0.28	0.26
λ_e	0.292	0.241	0.235	0.478	0.216	0.231	0.231	0.263	0.256
λ_p	0.183	0.218	0.251	0.168	0.159	0.167	0.240	0.261	0.256

The reorganization energies are shown in table 3.5 above. Commonly, Alq3 (tris(8-hydroxyquinolinato)aluminum(III), λ_e = 0.276 eV) and TPD (N,N-diphenyl-N,N-bis(3-methlphenyl)-(1,1-biphenyl)-4,4-diamine, λ_p = 0.290 eV) are considered as prototypic electron and hole transport materials, respectively that are used in this work for comparison [237, 238]. The reorganization energies show that metalated GNRs are better transport materials than the investigated virgin GNRs as they possess comparative lower value for the reorganization energy and in most cases lower than the prototypic Alq3 for electron and TPD for hole transport. The absence of electron correlation effect diminish the charge transport ability as in the RHF/6-31+g(d,p) level of theory for all the GNRs and the metal derivatives. K-azulene at the B3LYP/6-31+g(d,p) level of theory (λ_e = 0.216eV, λ_p =0.159eV) is the best electron and hole transport material amongst the studied GNRs and their metal derivatives. Rb-perylene possess good electron and hole transport properties at all three investigated level of theory. The results indicate that GNRs metal derivatives can be used as a good ambipolar hole and electron charge transport materials under the proper operating conditions and are therefore prospective charge transport materials for the assembly of optoelectronic devices such as organic lead emitting diodes (OLEDs).

In order for GNRs and their metal derivatives to be used as potential donor materials in OPVCs they should possess low value of the hole reorganization energy, lower than that of the prototypic hole transporter TPD, as the donor transports holes after exciton dissociation at the BHJ. Both virgin and metalated GNRs are good hole transporters, except at the RHF/6-31+g(d,p) for the virgin GNRs as they have hole reorganization energy greater than 0.290eV. Azulene is not also a good hole transporter at the B3LYP/6-31+g(d,p). In general terms the

metal GNRs have lower hole reorganization energy than the virgin GNRs at any level of theory, thus will serve as better donor materials in BHJ OPVCs. Consequently, these metalated GNRs have high short circuit current and are therefore characterized as emblematic transport materials due to their high hole mobility. K-azulene has the smallest hole reorganization energy at any level of theory than any of the rest two molecules. We are interested with the transport of holes, as we are characterizing donor materials which transfer holes after exciton dissociation. The carrier mobility of conjugated polymers are several orders of magnitude lesser than their crystalline counterparts due to recombinative carrier loss and could be improved by increasing carrier concentration and making sure that the conjugated polymer have a thin active layer that serve to reduce the optical absorption.

The computed transfer integral for hole-transport V_h and electron-transport V_e processes of the studied molecules are listed in table 3.5 above. High transfer integral value are needed for good preformat charge transfer molecules [239]. The investigated GNR metal derivative are better hole and electron transfer materials in agreement with the results obtained for the reorganization energy than the virgin GNR except for azulene. Phenanthrene transfer holes better than electrons while the metal derivative transfers electrons better than holes, while azulene follows the reverse trend. Perylene and its metal derivative at the RHF/6-31+g(d,p) level of theory is a better hole than electron transmitter, this goes same for GNR metal derivative at the two DFT methods. The hole and electron transfer rate against temperature for azulene are displayed in fig.3.7 below and are seen to reduce with temperature, the molecular materials operate best at charge transfer at low temperatures.

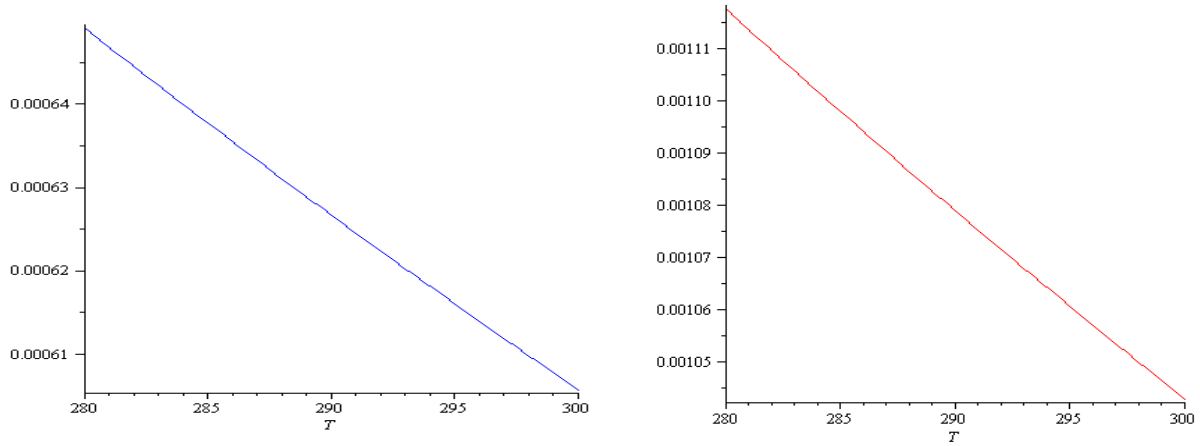

Fig.3.7 Hole charge transfer rate against temperature for azulene (left) and electron transfer rate against temperature for azulene (right) at B3LYPlevel of theory.

3.4.3 Nonlinear optical behavior for OPVC activity

Nonlinear optical (NLO) parameters such as α, $\Delta\alpha$, and β are of high relevance to comprehend the performance and behavior of OPVCs are shown in table 3.1. These properties measures the extent of the delocalization of intramolecular charge for the donor electrons [240]. High values for NLO properties provide a higher efficiency of charge mobility from donor to acceptor. According to Balanay [241], this greatly affects short-circuit current density, as well as the solar cell system efficiency. In related literature, the increase in NLO properties in some organic dyes and porphyrins is directly related with the increment in the photovoltaic performance of those systems [241-243]. The values of the hyperpolarizability, average polarizability and anisotropy in all the studied GNRs are greater in all the GNRs metalated molecules than in the starting molecule at all level of theory. The NLO values of α, $\Delta\alpha$, and β are significantly amplified for the studied metalated GNRs and are equally pronounced as compared to values obtained in [216]. Comparing our hyperpolaribility with the prototypic push-pull molecules, *para*-nitroaniline (p-NA) and urea with hyperpolarizabilities respectively, $5.01\times10^{-50}c^3m^2/J^2$, and $1.38\times 10^{-51}c^3m^2/J^2$ [200, 220, 221], it is observed that all the studied metal GNR have hyperpolarizabilities greater than the two prototypic molecules except k-phenanthrene at the RHF/6-31+g(d,p). This indicates a significant charge mobility efficiency from the donor GNRs metal derivative to acceptor PCBM. These high values of NLO properties are equally of interest in materials for emerging communication technologies and optical signals processing. The greatest NLO property is shown by Rb-perylene at all level theory.

Despite the incessant advances on the development of new organic polymers and innovative device engineering, the PCE of OPV devices has steadily improved to value of not more than 10% over the past years[143, 144, 244, 245]. Nonetheless, this efficiency isn't adequate to meet the realistic specifications for commercialization, which emanates from the mismatch of the absorption of the photoactive material to the terrestrial solar spectrum. Nevertheless Compared to silicon-based devices, polymer solar cells are lightweight (which is important for small autonomous sensors), potentially disposable and inexpensive to fabricate (sometimes using printed electronics), flexible, customizable on the molecular level and potentially have less adverse environmental impact. Polymer solar cells also have the potential to exhibit transparency, suggesting applications in windows, walls, flexible electronics, etc.

3.5 Mechanical properties and thermal stability

Stability is a very useful parameter in the design of potential optoelectronic device, such property is calculated through the chemical hardness ŋ which measures the resistance of a chemical species to electron cloud deformation or polarization under small perturbations from chemical reactions. Stabilities of the GNRs were investigated and predicted from interaction energies (ΔE_{int}). These properties were calculated using the equation

$$\eta = \frac{1}{2}\left(\frac{\partial \mu}{\partial N}\right) = \frac{1}{2}\left(\frac{\partial^2 E}{\partial N^2}\right) = \frac{IP - EA}{2} \qquad 3.2$$

where μ is the chemical potential, N is the total electron number, IP is the adiabatic ionization potential and EA is the adiabatic electron affinity.

$$\Delta E_{\text{int}} = E_{metal\ GNR} - (E_{virgin\ GNR} + H_2) \qquad 3.3$$

ΔE_{int} is calculated taking into consideration stoichiometry coefficient at each level of theory. As can be seen from table 3.2, the virgin GNRs are kinetically more stable and therefore chemically less reactive than its metal counterpart in all the levels of theory. The formation of the metal derivatives is favorable under ordinary temperature and pressure as ΔE_{int} is negative at all level of theory and for all the investigated GNRs. Rb-perylene corrobatively with the reactiveness of Rb has the smallest hardness of 0.555eV and thus is least stable and is therefore more reactive than any of the chemical species. Metalation is therefore counterproductive to chemical stability. The values of the thermodynamic properties of the GNRs and their metal derivatives shown and analyses as in table 3.6 also show some sought of structural molecular stability. The relatively high values of ŋ for the metalated molecules coupled with the negative values for the interaction energies indicate that they are energetically stable and therefore can be identified as excellent material for the construction of optoelectronic devices for nonlinear applications, making the goal of achieving novel materials for NLO application with better efficiencies, coupled with attributable practical performance such as chemical stability and easy processability for making technological applications closer.

3.6 Effect of metalation on the Thermodynamic properties of the GNRs and their metal counterpart

The thermodynamics properties of the molecules are shown in the table 3.6. We noticed that the Zero-point vibrational energy (ZPVE) and total electronic energy are approximately the same for the three levels of theory for each molecule. The Energy values reflect the stability of

the organic molecule. The zero-point energy is a correction to molecular vibration at 0K. These results are indicative of the fact that the simulations are done under similar ambient conditions, so the molecules are stable and the slight variation in the thermodynamic properties are due to the inclusion of correlation effects. Electron correlation effects decrease all the investigated thermodynamic value for all the molecules. The sum of total electronic energies for phenanthrene is similar to that obtained by Alan Hinchliffe, at the HF/6-311G(3d,2p) level of theory [246]. The metal derivatives of the GNRs is seen to be more unstable than the virgin GNRs as they have high negative values for the electronic energy (E_0), Sum of electronic and zero-point Energies, Sum of electronic and thermal Energies, Sum of electronic and thermal Enthalpies, Sum of electronic and thermal Free Energies, confirming earlier results obtained in section 3.5, on reduced stability of the metal GNRs than their virgin counterpart, which though is not too low for optoelectronic and OPVC applications

Table 3.6a Thermodynamic properties of the investigated virgin GNRs

Properties	Phenanthrene			Azulene			Perylene
	RHF	B3LYP	BPBE	RHF	B3LYP	BPBE	RHF
$ZPVE(J/mol)$	545375.9	510122.6	496799.9	403888.9	381553.5	373720.7	711840.3
$E_0(au)$	-536.04	-539.57	-539.29	-383.31	-385.94	-385.66	-764.45
$\epsilon_1(au)$	-535.83	-539.38	-539.1	-383.16	-385.79	-385.52	-764.17
$\epsilon_2(au)$	-535.83	-539.37	-539.09	-383.15	-385.78	-385.51	-764.16
$\epsilon_3(au)$	-535.82	-539.38	-539.09	-383.15	-385.78	-385.51	-764.16
$\epsilon_4(au)$	-535.87	-539.41	-539.13	-383.19	-385.82	-385.55	-764.21

Table 3.6b Thermodynamic properties of the investigated GNRs metal derivatives

Properties	k-phenanthrene			k-Azulene			Rb-perylene		
	RHF	B3LYP	BPBE	RHF	B3LYP	BPBE	RHF	B3LYP	BPBE
$ZPVE(J/mol)$	371139	348059.7	463960.7	371139	348059.7	339125.6	674301.2	630197.1	613396.7
$E_0(au)$	-981.9	-985.24	-1138.48	-981.9	-985.24	-984.98	-787.61	-792.89	-792.52
$\epsilon_1(au)$	-981.75	-985.11	-1138.3	-981.75	-985.11	-984.85	-787.36	-792.65	-792.28
$\epsilon_2(au)$	-981.75	-985.1	-1138.29	-981.75	-985.1	-984.84	-787.34	-792.64	-792.27
$\epsilon_3(au)$	-981.74	-985.1	-1138.29	-981.74	-985.1	-984.84	-787.34	-792.64	-792.27
$\epsilon_4(au)$	-981.79	-985.14	-1138.34	-981.79	-985.14	-984.88	-787.4	-792.7	-792.33

Electronic energy (E_0), Zero-point vibrational energy (ZPVE)

ϵ_1 =Sum of electronic and zero-point Energies, ϵ_2 = Sum of electronic and thermal Energies, ϵ_3 =Sum of electronic and thermal Enthalpies, ϵ_4 =Sum of electronic and thermal Free Energies

3.7 Vibrational analysis and spectra

Each GNR and its metal derivative has similar mode of vibration, all active in the infrared and Raman spectrum. Phenanthrene and its metal derivative have 66 modes, while azulene has 48 and perylene has 90. The modes seem to increase in proportion to the size of the GNR, as is expected. The Raman and infrared spectrum of the molecule are given in fig 3.8 to fig 3.13. Such frequency analysis was done to confirm the stability of the optimized structures. As indicated in these spectra, no imaginary frequencies were found. Indicating local minima were attained at the end of the optimization. Observing the various graphs for the Raman activity molecular vibration spectroscopy analysis, indicates almost the same frequency range of vibrations cause almost the same change in polarizability of the GNRs and their metal derivative. The frequency range causing the greatest polarizabilities are generally between 900-1800cm^{-1} and the 3000-3600cm^{-1} frequencies for all the molecules and at all level of theory, though with slight variation. Phenanthrene has the greatest polarizability between 1200-1800cm^{-1} and from 3000-3600 cm^{-1}, while its metal counterpart has it from 300-1800cm^{-1} and from 3000-3600cm^{-1}. Azulene has the greatest polarizability from 600-1800cm^{-1} and from 3000-3450cm^{-1} while K-azulene has its greatest polarizability from 900-1800cm and 3000-3450cm^{-1}. Perylene follows from 1200-1800cm^{-1} and 3300-3450cm^{-1}. The metal counterpart ranges from 600-1800 cm^{-1} and 3000-3600 cm^{-1}. The molecules are in most cases highly Raman active at the BPBE/6-31+g(d,p) level of theory at each frequency and least at the RHF/6-31+g(d,p), indicating the inclusion of electron correlation effects increases the Raman activity of the molecule. Metalation broadens and increases the frequency range of polarization

Observing the infrared activity graphs also indicates that similar frequency vibration range cause similar change in the permanent dipole moment of the molecules with the greatest change found around the 1500cm^{-1} and the 3000cm^{-1} frequencies. Metalation is seen to increase the IR activity of the molecule. Such spectroscopic analysis will provide a structural fingerprint by which the molecules can be identified.

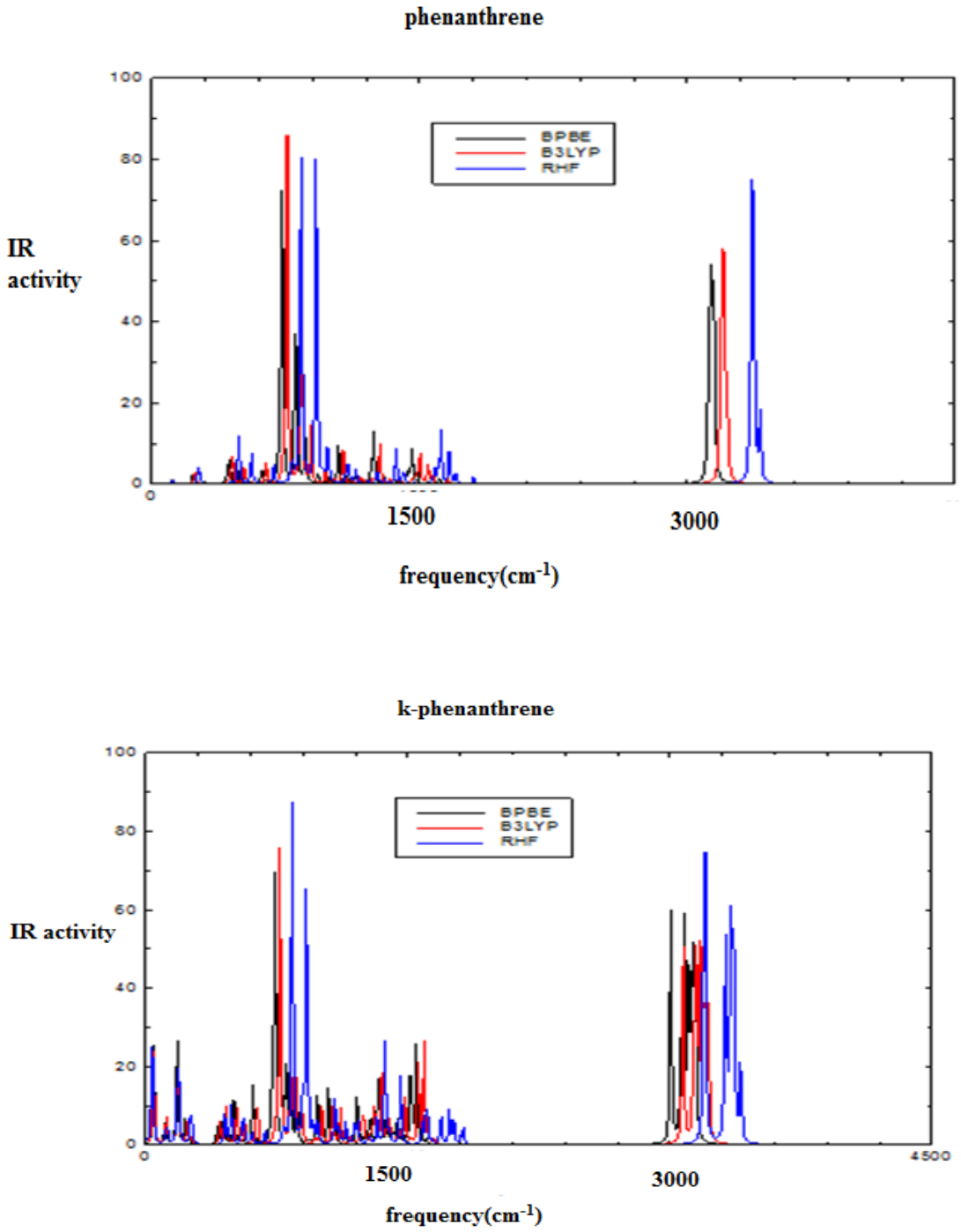

Fig 3.8 IR activity of phenanthrene and K-phenanthrene

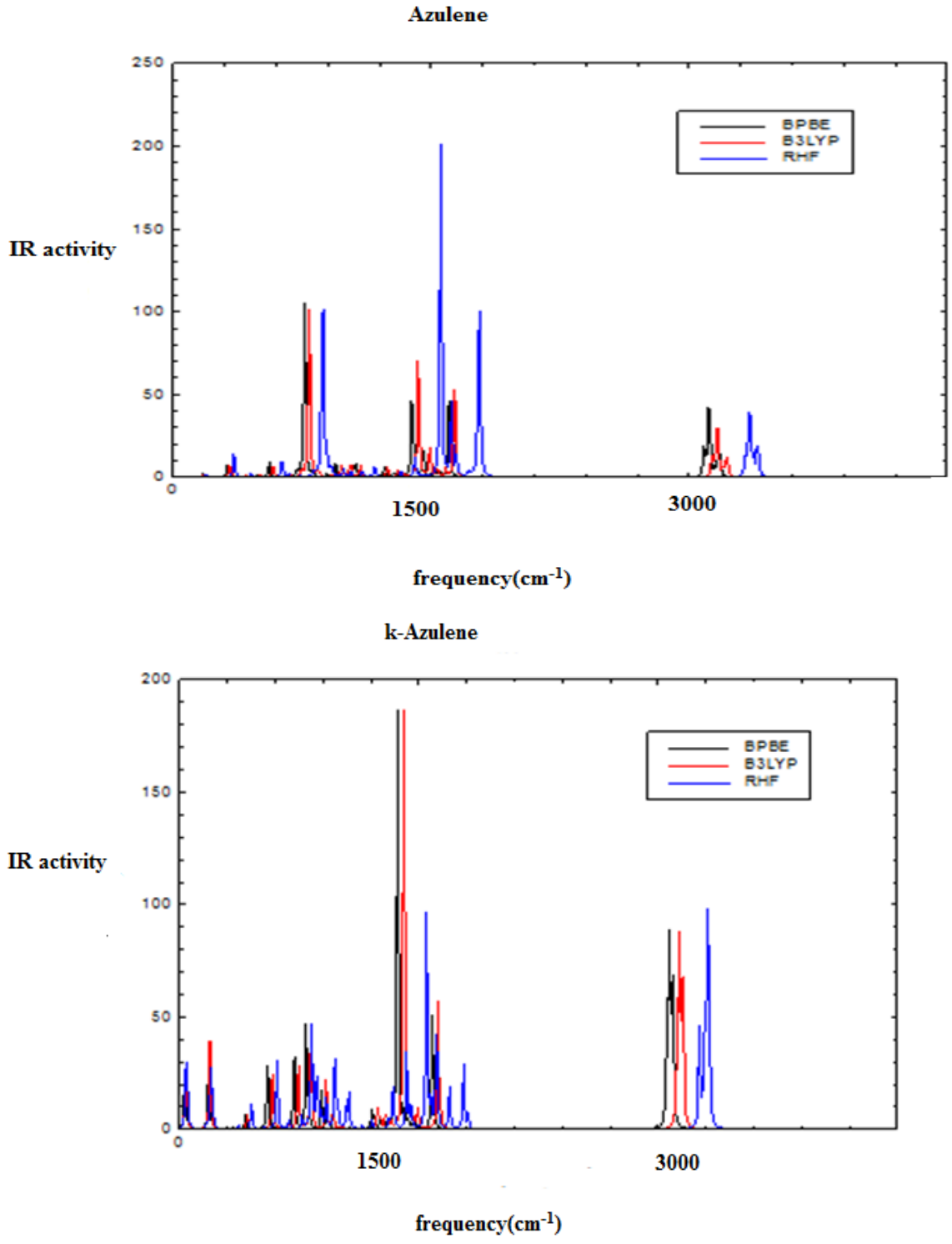

Fig 3.9 IR activity of azulene and k-azulene

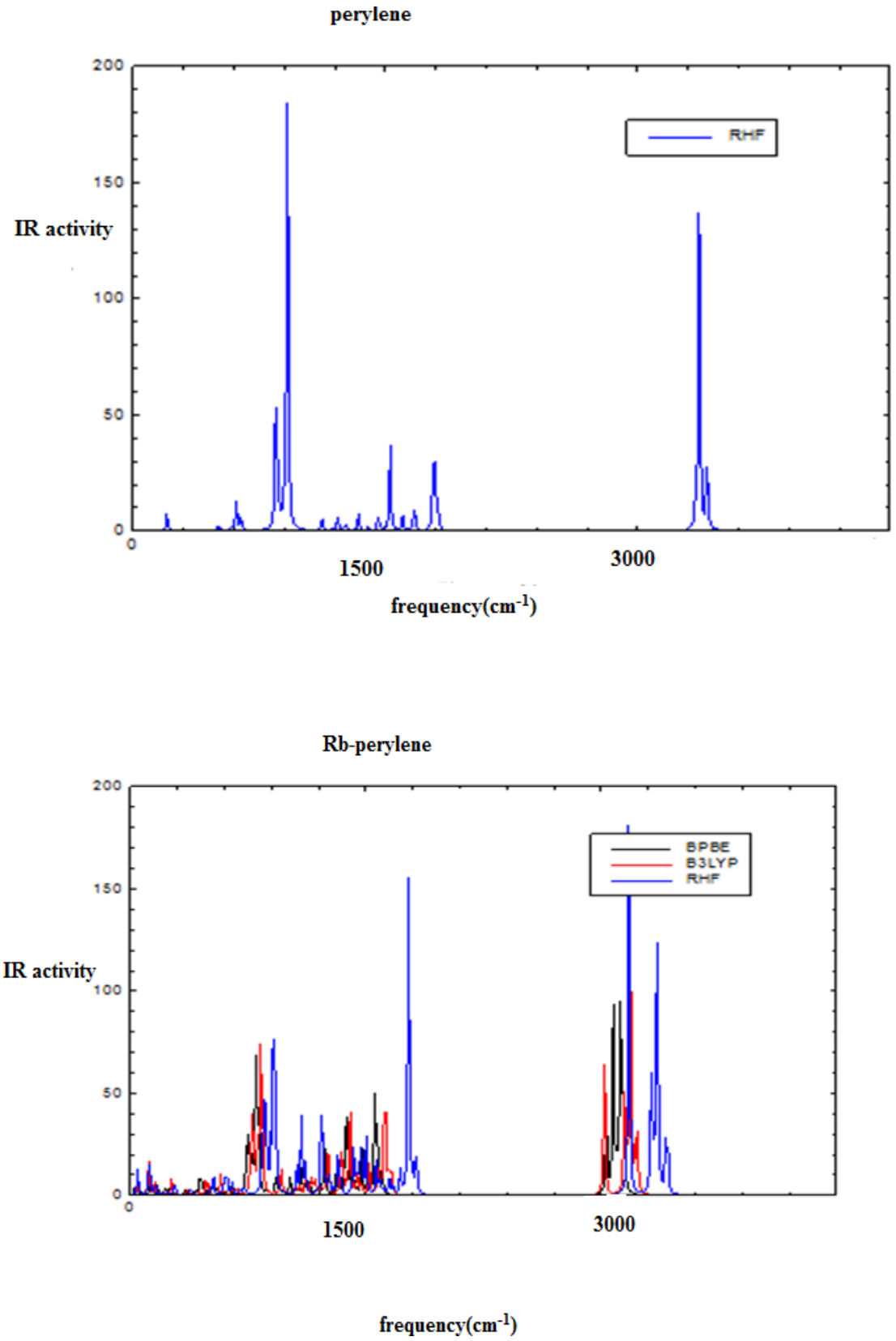

Fig 3.10 IR activity of perylene and Rb-perylene

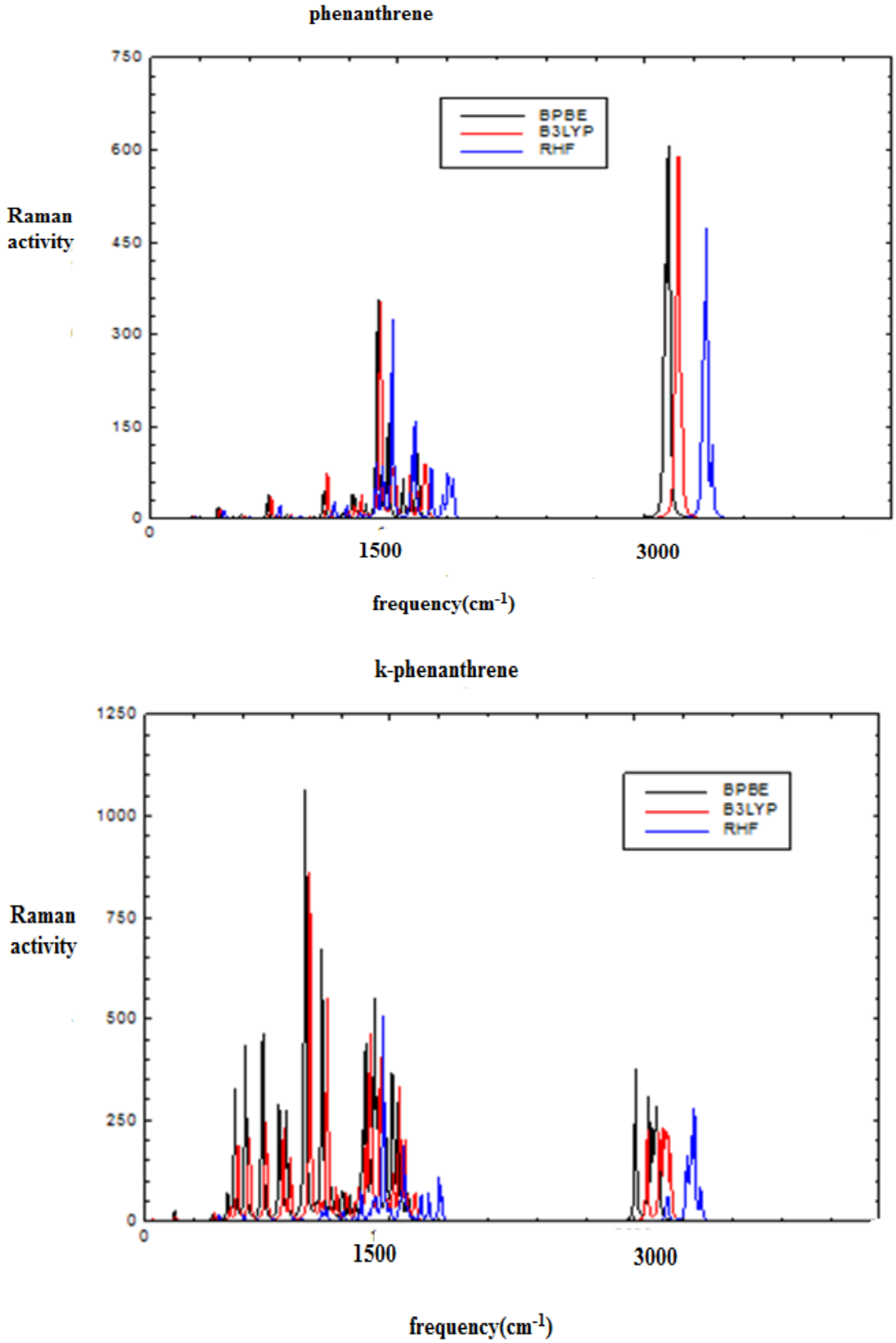

Fig 3.11 Raman activity of phenanthrene and k-phenanthrene

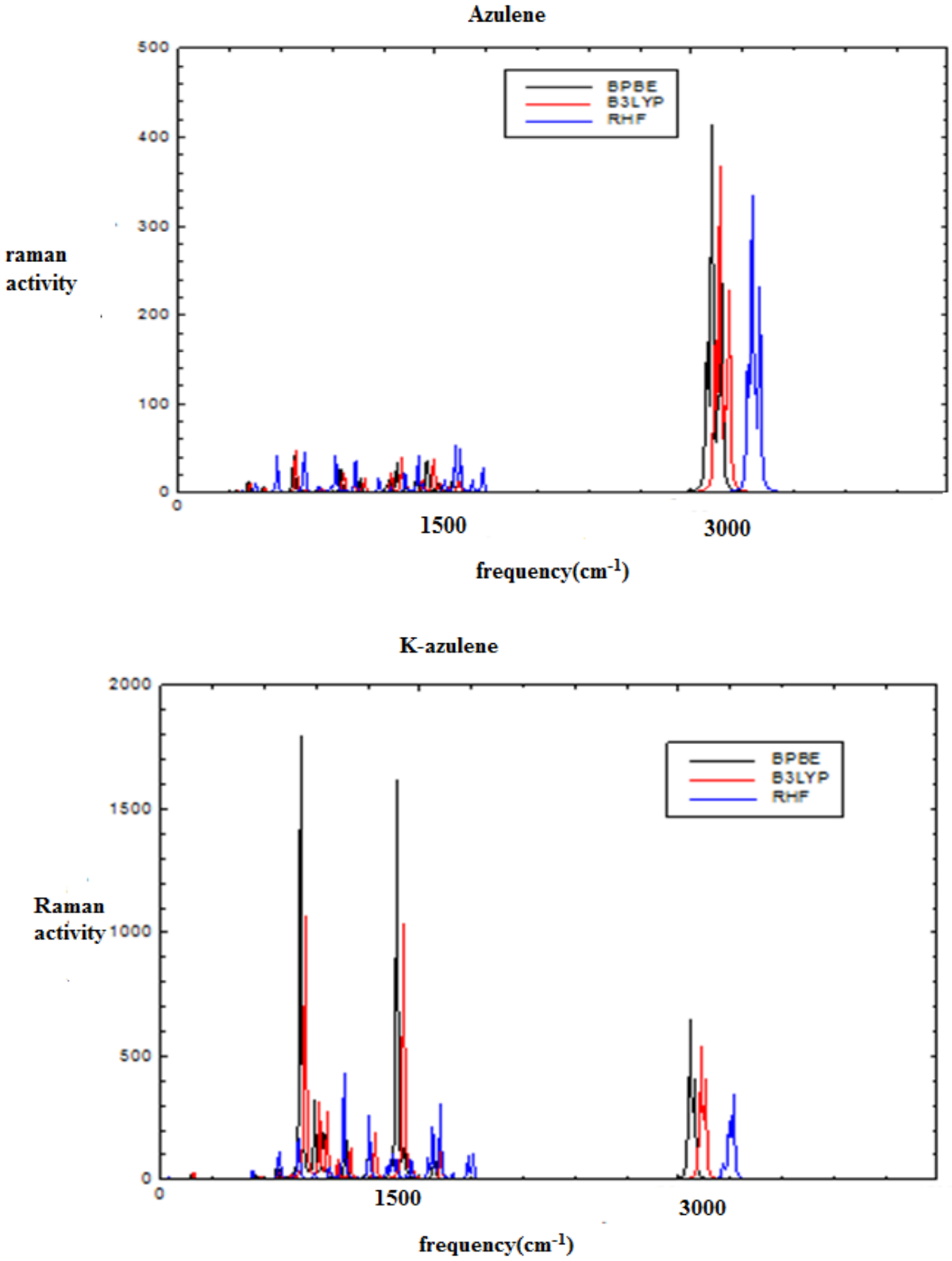

Fig 3.12 Raman activity of azulene and k-azulene

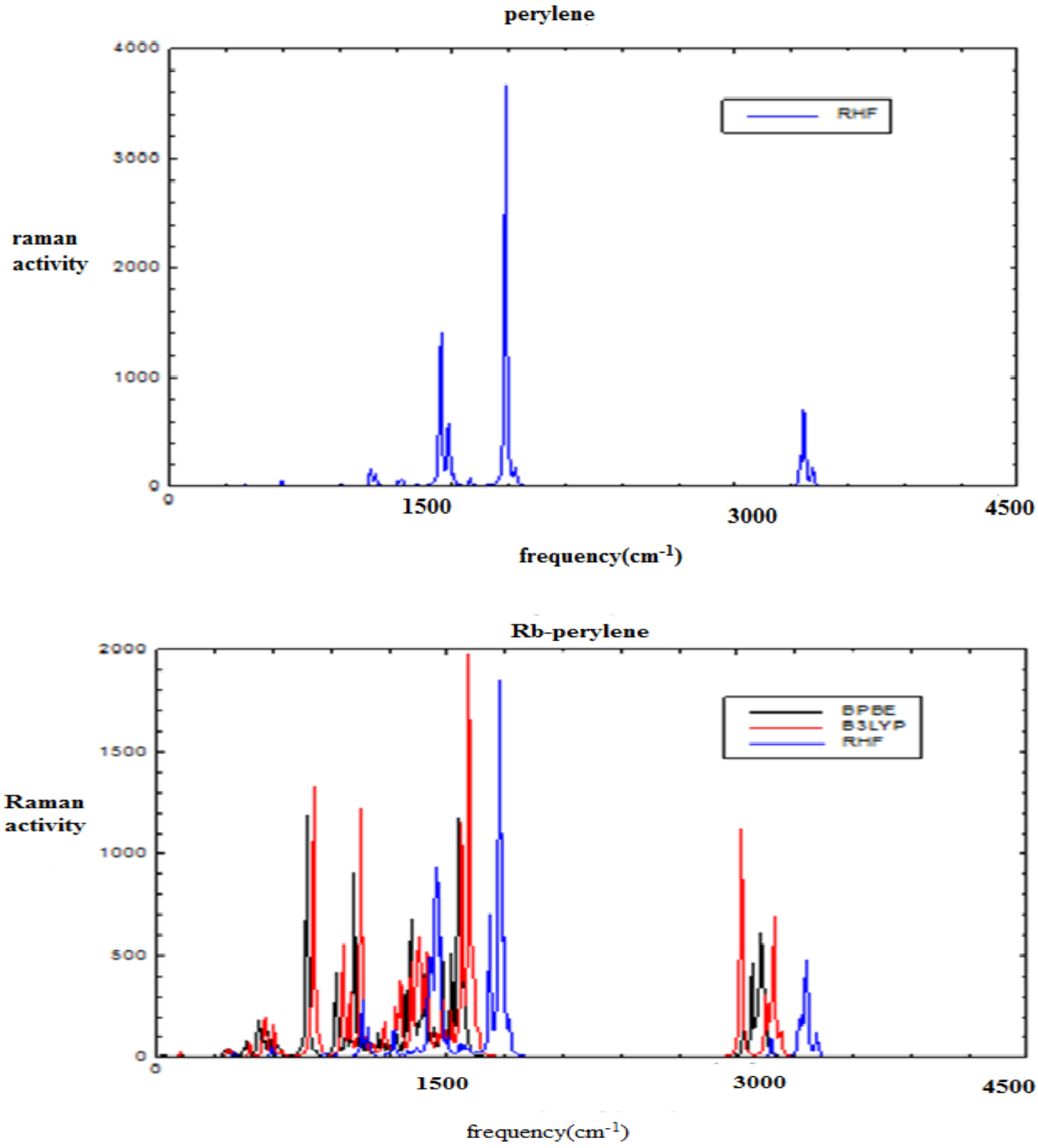

Fig 3.13 Raman activity of perylene and Rb-perylene

3.8 Conclusion

Metal-organic electronic molecules are drawing great attention newly because of the diversity of molecular models and numerous electronic applications. GNRs are a class of organic compound with a lot of potential application in the field of optoelectronic, reason we investigate the impact of metal substitution on the GNRs on its nonlinear, charge transport, mechanical stability, OPV properties. Theoretical calculations were performed using the ab

initio RHF and the density functional theory (DFT) method, via the exchange-correlation functionals BPBE and B3LYP, alongside the basis 6-31+g(d,p). From the results obtained the metal GNRs show high nonlinear optical activity than the virgin GNR which is interestingly higher than the classical urea and *para*-nitroaniline (p-NA). These studied GNRs are therefore fascinating building materials for constructing optoelectronic and photonic devices suitable for second- and third-order NLO activity. The same trend is obtained for charge transport properties showing GNRs metal derivatives are good ambipolar charge transport materials with transport qualities better in most cases than the prototypic Alq3 (tris(8-hydroxyquinolinato)aluminum(III), λ_e = 0.276eV) and TPD (N,N-diphenyl-N,N-bis(3-methlphenyl)-(1,10-biphenyl)-4,40-diamine, λ_p = 0.290eV) with promising charge transport application for the manufacture of organic light emitting diodes (OLEDs). K-azulene at the B3LYP/6-31+g(d,p) level of theory (λ_e = 0.216eV, λ_p =0.159eV) is the best electron and hole transport material amongst the studied GNRs and their metal derivatives. Rb-perylene possess good electron and hole transport properties at all three investigated level of theory. The small hole reorganization energy when compared to the classical hole transport molecule TPD, shows that the donor semiconductor metal GNRs in the domain of OPVC operation have a laudable hole mobility in the process of charge carrier transmission and could therefore provide a high short circuit current. In contrast to the improvement in nonlinear optical activity and charge transport properties upon metal substitution of the GNRs, the metal stability is seen to unexpectedly decrease.

Our computational results predicted, the photovoltaic properties of the metalated GNRs and the virgin counterpart to serve as donor material in OPV cells. The materials possess a disapproving large band gap at the RHF and B3LYP/6-31+g(d,p) level of theory as compared to the below 1.9eV recommended value for OPVC, but with this value attained at the BPBE/6-31+g(d,p)level of theory for the metal GNRs. Rb-perylene at the BPBE/6-31+g(d,p)level of theory has the smallest band gap of 1.10eV. They also have commendable small gap, when compared to traditional crystalline inorganic semiconductors materials, with well-placed position of HOMO and LUMO levels. The metal GNRs perform better than the virgin GNRs in OPVCs functioning in the domain of band gap as the virgin GNRs have large band gaps. The small hole reorganization energy when compared to the classical hole transport molecule TPD, shows that the donor semiconductor metal GNRs have a laudable hole mobility in the process of charge carrier transmission and could therefore provide a high short circuit current. The best hole mobility is shown by K-azulene which also give the greatest value for the exciton

dissociation linked parameter ΔE_{LL}. It is observed that all the virgin GNRs have ΔE_{LL} greater than the required 0.3V minimum, with the greatest value shown by phenanthrene at the 6-31+g(d,p) level of theory. We remark that all the metalated GNRs have a ΔE_{LL} value that is above the 0.3eV requirement, though the virgin GNRs perform better with this parameter than the metal counterpart. All the virgin GNRs have good V_{oc} values above the 1V minimum value for the optimal performance of OPVCs, except for azulene at the BPBE/6-31+g(d,p) level of theory, with the highest value obtained by phenanthrene at the RHF/6-31+g(d,p) level of theory. The open circuit voltage for the metalated GNRs falls moderately short of practical values especially at the DFT methods. However, hope to improve these values could dwell on other determining factors for V_{oc}, such as: donor energy levels, chemical potential gradients, light intensity, morphology (rough or smooth surface), external fluorescence, recombination of charge-carrier, light-source, cell temperatures, charge-carrier recombination, Fermi level pinning. Comparatively, the virgin GNRs perform better than GNRs in the area of V_{oc}.The theoretical predicted value for PCE of our device for Rb-perylene at the BPBE/6-31+g(d,p) level of theory may attain the 10% current mark for OPV cell which is a benchmark research finding and motivation for experimental consolidation of our theoretical work. This gives an additional incentive to design effective new photovoltaic materials efficient bulk heterojunction solar cells. The elevation of the efficiency realized in this research gets this organic polymer a step closer to commercialization. Following the methodology established in the present work, there will be commendable future progress in the modelling of solar cell devices based upon OPV polymers based on GNRs and their metal derivatives. The approach of the present work may be an invaluable tool in acquiring accurate results in the development of innovative data sets of electronic structure properties on OPV polymer and for the fabrication of solar cells, getting these organic polymers a step closer to commercialization.

Equally, the key thermodynamic parameters of the molecules carried out under the same conditions of temperature and pressure show that the molecules are stable. The Raman activity molecular vibration spectroscopy analysis, was done to confirm the stability of the optimized structures. As indicated in these spectra, no imaginary frequencies were found. Indicating local minima were attained at the end of the optimization. The vibration spectroscopy analysis also indicates that similar frequency range of vibrations cause almost the same change in polarizability of the molecule. The frequency range causing the greatest polarizabilities are found around the 1500 cm^{-1} and the 3000cm^{-1} frequencies for all the molecules and at all level of theory. The infrared activity indicates that the same frequency

vibration range cause the same change in the permanent dipole moment of the molecules. Such frequency range are equally found around the 1500 cm^{-1} and the 3000cm^{-1} frequencies for all the molecules and at all level of theory. These spectroscopic analyses provide a structural fingerprint by which the GNRs can be identified.

GENERAL CONCLUSION AND PERSPECTIVE

The aim of this research is to study the electronic and optical properties of a class of organometallic semiconductor materials in the form of graphene nanoribbons (GNRs) for optoelectronic and organic photovoltaic applications, using the theoretical based computational approach where the ab initio methodologies based on Density Functional Theory (DFT) are intensely used by researchers to solve complex problems. As it is found to be more reliable and provides better results concerning the electronic structure calculations in designing and modeling new materials and tuning their properties without prior experimental knowledge. Graphene nanoribbons (GNRs) were chosen as they attract great interest because of their highly tunable electronic, optical, and transport properties. GNRs has attracted considerable importance in the industry and research community due to its outstanding properties. It is quite recent, there has been a large importance towards the study and realization of GNRs based on optical devices designed by appropriate tailoring of the electronic structure, exploiting not only the electric field effect but also other properties as applied strain. The objective of this research was to optimize the geometrical structure of some GNRs organic materials (phenanthrene, azulene and perylene), to investigate the effects of metalation on the NLO, transport and OPV properties of the GNRs, to compare and contrast the properties of the virgin GNRs with their metalated counterparts, to simulate OPV device and investigate its efficiency.

The ab intio RHF, the DFT B3LYP and BPBE methods together with the Pople-style basis set 6-31+g(d,p) were employed in the study to obtain the results presented. Based on our results, the following conclusions have been made:

From the results obtained the metal GNRs show high nonlinear optical activity than the virgin GNR which is interestingly higher than the classical urea and *para*-nitroaniline (p-NA). These studied GNRs are therefore fascinating building materials for constructing optoelectronic and photonic devices suitable for second- and third-order NLO activity. The same trend is obtained for charge transport properties showing GNRs metal derivatives are good ambipolar charge transport materials than the virgin GNRs and also have transport qualities better in most cases than the prototypic Alq3 (tris(8-hydroxyquinolinato)aluminum(III), λ_e = 0.276eV) and TPD (N,N-diphenyl-N,N-bis(3-methlphenyl)-(1,1-biphenyl)-4,4-diamine, λ_p = 0.290eV) with promising charge transport application in for the manufacture of organic light emitting diodes

(OLEDs). In contrast to the improvement in nonlinear optical activity and charge transport properties upon metal substitution of the GNRs, the mechanical stability is seen to unexpectedly decrease.

We observe the fact the materials, both virgin and their metal derivatives possess a disapproving large band gap at the rhf and b3lyp/6-31+g(d,p) level of theory as compared to the below 1.9eV recommended value for OPVC, but with this value attained at the bpbe/6-31+g(d,p)level of theory. Rb-perylene at the bpbe/6-31+g(d,p)level of theory has the smallest band gap of 1.10eV. We also notice that the GNRs also have commendable small gap, when compared to traditional crystalline inorganic semiconductors materials, with well-placed position of HOMO and LUMO levels. The small hole reorganization energy when compared to the classical hole transport molecule TPD, shows that the donor semiconductor metal GNRs have a laudable hole mobility in the process of charge carrier transmission and could therefore provide a high short circuit current. The best hole mobility is shown by K-azulene which also give the greatest value for the exciton dissociation linked parameter ΔE_{LL}. All the molecules also have exciton dissociation value greater than the 0.3eV minimum required value. The open circuit voltage for the metal GNRs falls moderately short of practical values especially at the dft methods, though hope to valorize it could stem from other determining factors like donor energy levels, chemical potential gradients, light intensity and morphology. The theoretical predicted value for PCE of our device for Rb-perylene may attain the 10% current mark for OPV cell which is a benchmark research finding and motivation for experimental consolidation of our theoretical work. This gives an additional incentive to design effective new photovoltaic materials efficient bulk heterojunction solar cells. The elevation of the efficiency realized in this research gets this organic polymer a step closer to commercialization. The NLO values of α, $\Delta\alpha$, and β are significantly amplified with β for the metalated GNRs greater than the prototypic push-pull molecule, urea. This would represent potential systems that would effectively transfer electronic charge from the donor to the acceptor

Following the methodology established in the present work, there will be commendable future progress in the modelling of solar cell devices based upon OPV polymers based on GNRs metal derivatives. The approach of the present work may be an invaluable tool in acquiring accurate results in the development of innovative data sets of electronic structure properties on OPV polymer and for the fabrication of solar cells, getting these organic polymers a step closer to commercialization.

This study gives a great impetus in the search of nanomaterials for optoelectronic and photovoltaic technology, this research could be further expounded by taking a time dependent DFT study on the effects of metalation on the nonlinear optical, charge transport and photovoltaic properties of some graphene nanoribbons

This study could also be extended to other class of organic compound like graphene carbon tubes and other organic molecules that have interesting NLO properties

This study could still be further expounded taking into consideration other parameters like the solvent effect, temperature and pressure

REFERENCES

1. Kivala, M.; Diederich, F., Acetylene-derived strong organic acceptors for planar and nonplanar push− pull chromophores Acc. Chem. Res., 42, 235 (2009)

2. Kato, S.; Diederich, F., Non-planar push–pull chromophores Chem. Commun. 2010, 46, (1994).

3. Meier, H., Angew. Conjugated oligomers with terminal donor–acceptor substitution, Chem., Int. Ed., 44, 2482, (2005)

4. Kivala, M.; Diederich, F., Conjugation and optoelectronic properties of acetylenic scaffolds and charge-transfer chromophores, Pure Appl. Chem., 80, 41,(2008)

5. Marder, S. R.; Perry, J. W., Molecular materials for second-order nonlinear optical applications, Adv. Mater., 5, 804, (1993)

6. Coe, B. J., Molecular materials possessing switchable quadratic nonlinear optical properties, Chem. - Eur. J., 5, 2464(1999).

7. Asselberghs, I.; Clays, K.; Persoons, A.; Ward, M. D.; McCleverty, J., Switching of molecular second-order polarisability in solution, J. Mater. Chem., 14, 2831, (2004)

8. Y Ouyang, D Wu, R Fu, Graphene oxide-supported two-dimensional microporous polystyrene, MRS Online Proceedings Library volume 1549, 25–29 (2013)

9. Lin, Y.; Li, Y.; Zhan, X., Small molecule semiconductors for high-efficiency organic photovoltaics, Chem. Soc. Rev., 41, 4245, (2012)

10. Wu, Y.; Zhu, W., Organic sensitizers from D–π–A to D–A–π–A: effect of the internal electron-withdrawing units on molecular absorption, energy levels and photovoltaic performances, Chem. Soc. Rev., 42, 2039 (2013)

11. C. K. Wang, P. Macak, Y. Luo, and H. Ågren. Effects of π centers and symmetry on two-photon absorption cross sections of organic chromophores, J. Chem. Phys., 114:9813, (2001).

12. P. Macak, Y. Luo, P. Norman, and H. Ågren. Electronic and vibronic contributions to two-photon absorption of molecules with multi-branched structures, J. Chem. Phys., 113:7055, (2000)

13. K. A. Nguyen, J. E. Rogers, J. E. Slagle, P. N. Day, R. Kannan, L.-S. Tan, P. A. Fleitz, and R. Pachter, Effects of conjugation in length and dimension on spectroscopic properties of fluorene-based chromophores from experiment and theory, J. Phys. Chem. A, 110:13172, (2006).

14. K. A. Nguyen, P. N. Day, and R. Pachter, One-and two-photon spectra of platinum acetylide chromophores: a TDDFT study, J. Phys. Chem. A, 113:13943, (2009)

15. M. Albota, D. Beljonne, J. L. Bredas, J. E. Ehrlich, J. Fu, A. A. Heikal, S. E. Hess, T. Subramaniam, W. W. Webb, X. Wu, and C. Xu. Design of organic molecules with large two-photon absorption cross sections, Science, 281:1653, (1998)

16. Hernandez, R., S. Easter, M. Murphy-Mariscal, F. Maestre, M. Tavassoli, E. Allen, C. Barrows, J. Belnap, R. Ochoa-Hueso, and S. Ravi, Environmental impacts of utility-scale solar energy. Renewable and Sustainable Energy Reviews,. 29: p. 766-779 (2014)

17. Brabec, C.J., Organic photovoltaics: technology and market. Solar Energy Materials and Solar Cells,. 83(2): p. 273-292 (2004)

18. Benanti, T.L. and D. Venkataraman, Organic solar cells: An overview focusing on active layer morphology. Photosynthesis Research,. 87(1) 73-81 (2006)

19. Nunzi, J.-M., Organic photovoltaic materials and devices. C. R. Physique,3(4) 523–542, 15 (2002)

20. Y. Cui, H. Yao, J. Zhang, T. Zhang, Y. Wang, L. Hong, Over 16% efficiency organic photovoltaic cells enabled by a chlorinated acceptor with increased open-circuit voltages, nature comm. 10, 2515, 19 (2019)

21. Y. Cui, H. Yao, L. Hong, T. Zhang, Advanced Materials Communication, Achieving Over 15% Efficiency in Organic Photovoltaic Cells via Copolymer Design, advanced materials, 31(14) 1808356 (2019)

22. M. Aliofkhazraei, N.A. William I. Milne, (Graphene Science Handbook Electrical and Optical Properties" by Taylor & Francis Group, LLC. 2016)

23. N. S. Moghaddam, M. T. Ahmadi,M. Rahmani, N. Aziziah et.al. "Monolayer Graphene Nanoribbon p-n Junction" IEEE (2011)

24. A. K. Bodenmann and A. H. MacDonald, “Graphene: Exploring carbon flatland,” Physics Today, 60, 8, 35–41, (2007).

25. S. Sahoo, A. K. Dutta “Graphene: A New Star In Material Science”; Emerging Science. 2, 2, 16, (2010)

26. D. Banerjee, S. Sahoo “Energy band nonparabolicity and density of states of graphene” NSNTAIJ, vol.7,no. 6, 2013. S. E.Bryan “Structural And Electrical Properties Of Epitaxial Graphene Nanoribbons” Georgia Institute of Technology A Dissertation Ph.D. May (2013)

27. H. E. Ruda “Widegap II–VI Compounds for Opto-electronic Applications “Springer Science & Business Media, 1, (2013)

28. Miyamoto, Y.; Nakada, K.; Fujita, M. First-principles study of edge states of H-terminated graphitic ribbons, Phys. Rev. B, 59, 9858 (1999)

29. Jiao, L., Zhang, L., Wang, X., Diankov, G., Dai, H. First-principles study of edge states of H-terminated graphitic ribbons Nature, 458, 877 (2009)

30. C. Bonner, Bottom-Up Synthesis and Electronic Structure of Graphene Nanoribbons on Surfaces (University of California Berkeley, Berkeley, CA, United States 2018)

31. Kosynkin, D. V., Higginbotham, A. L., Sinitskii, A., Lomeda, J. R., Dimiev, A., Price, B. K.; Tour, J. M. Longitudinal unzipping of carbon nanotubes to form graphene nanoribbons, Nature, 458, 872, (2009)

32. Cano-Márquez, A. G.; Rodríguez-Macías, F. J.; Campos-Delgado, J.; Espinosa-González, C. G.; Tristán-López, F.; Ramírez-González, D.; Cullen, D. A.; Smith, D. J.; Terrones, M.; Vega-Cantú, Y. I. Nano Lett., 9, 1527 (2009).

33. Elias, A. L.; Botello-Mendez, A. s. R.; Meneses-Rodriguez, D.; Jehova Gonzalez, V.; Ramírez-Gonzalez, D.; Ci, L.; Munoz-Sandoval, E.; Ajayan, P. MM. Nano Lett., 10, 366 (2009).

34. Wang, X.; Dai, H. Etching and narrowing of graphene from the edges, Nat. Chem., 2, 661, (2010)

35. Kato, T.; Hatakeyama, R. Site- and alignment-controlled growth of graphene nanoribbons from nickel nanobars, Nat. Nanotechnol., 7, 651,(2012).

36. C. Chen, W. Fan, T. Ma, X. Fu, Fabrication of functionalized nitrogen-doped graphene for supercapacitor electrodes, Ionics volume 20, pages1489–1494 (2014)

37. Novoselov, K. S.; Geim, A. K.; Morozov, S. V.; Jiang, D.; Zhang, Y.; Dubonos, S. V.;Grigorieva, I. V.; Firsov, A. A. Science, 306, 666,(2004)

38. Li, X.; Wang, X.; Zhang, L.; Lee, S.; Dai, H. Chemically derived, ultrasmooth graphene nanoribbon semiconductors, Science, 319, 1229, (2008)

39. Stankovich, S.; Dikin, D. A.; Dommett, G. H. B.; Kohlhaas, K. M.; Zimney, E. J.; Stach, E. A.; Piner, R. D.; Nguyen, S. T.; Ruoff, R. S. Graphene-based composite materials, Nature, 442, 282, (2006)

40. Li, D.; Muller, M. B.; Gilje, S.; Kaner, R. B.; Wallace, G. G. Processable aqueous dispersions of graphene nanosheets, Nat. Nanotechnol., 3, 101, (2008)

41. Tung, V. C.; Allen, M. J.; Yang, Y.; Kaner, R. B. High-throughput solution processing of large-scale graphene, Nat. Nanotechnol., 4, 25, (2009).

42. D Tošić, Z Marković, M Dramićanin, IH Antunović, Gamma ray assisted fabrication of fluorescent oligographene nanoribbons, 47, 8, 1996-2000, (2012)

43. Han, M. Y.; Özyilmaz, B.; Zhang, Y.; Kim, P. Energy band-gap engineering of graphene nanoribbons, Phys. Rev. Lett., 98, 206805, (2007)

44. Vo, T. H.; Shekhirev, M.; Kunkel, D. A.; Morton, M. D.; Berglund, E.; Kong, L.; Wilson, P.M.; Dowben, P. A.; Enders, A.; Sinitskii, A. Large-scale solution synthesis of narrow graphene nanoribbons, Nat. Commun., 5, 3189, (2014).

45. Vo, T. H.; Shekhirev, M.; Kunkel, D. A.; Orange, F.; Guinel, M. J. F.; Enders, A.; Sinitskii, A. Bottom-up solution synthesis of narrow nitrogen-doped graphene nanoribbons, Chem. Commun., 50, 4172 (2014).

46. Sakaguchi, H.; Kawagoe, Y.; Hirano, Y.; Iruka, T.; Yano, M.; Nakae, T. Formation of Dibenzopentalene-linking Polymers under the Two-zone CVD and Wet Conditions, Adv. Mater, 26, 4134, (2014).

47. Yang, X.; Dou, X.; Rouhanipour, A.; Zhi, L.; Räder, H. J.; Müllen, K. Two-dimensional graphene nanoribbons, J. Am. Chem. Soc., 130, 4216, (2008)

48. Grill, L.; Dyer, M.; Lafferentz, L.;. Nano-architectures by Covalent Assembly of Molecular Building Blocks. Nat. Nanotechnol., 2, 687, (2007)

49. Bieri, M.; Treier, M.; Cai, J.; Porous Graphenes: Two-Dimensional Polymer Synthesis with Atomic Precision. Chem. Commun., 6919–6921, (2009)

50. Walch, H.; Gutzler, R.; Sirtl, T.; Eder, G.; Lackinger, M. Material- and Orientation-Dependent Reactivity for Heterogeneously Catalyzed Carbon–Bromine Bond Homolysis. J. Phys. Chem. C, 114, 12604, (2010)

51. Bieri, M.; Nguyen, M.-T.; Gröning, O J Cai, Two-Dimensional Polymer Formation on Surfaces: Insight Into the Roles of Precursor Mobility and Reactivity. J. Am. Chem. Soc., 132, 16669, (2010)

52. Blunt, M. O.; Russell, J. C.; Champness, N. R.; Beton, P. H. Templating Molecular Adsorption Using a Covalent Organic Framework. Chem. Commun., 46, 7157, (2010)

53. Krasnikov, S. A.; Doyle, C. M.; Sergeeva, N. N Alexei B., Formation of Extended Covalently Bonded Ni Porphyrin Networks on the Au(111) Surface. Nano Res., 4, 376, (2011)

54. Cardenas, L.; Gutzler, R.; Lipton-Duffin, J.; Chaoying F.; Jaclyn L. B.; b, Laurentiu E. Dinca.; Synthesis and Electronic Structure of a Two Dimensional p-Conjugated Polythiophene. Chem. Sci., 4, 3263, (2013)

55. Lafferentz, L.; Ample, F.; Yu, H.; Conductance of a Single Conjugated Polymer as a Continuous Function of Its Length. Science, 323, 1193, (2009).

56. Lipton-Duffin, J. A.; Ivasenko, O.; Perepichka, D. F.; Rosei, F. Synthesis of Polyphenylene Molecular Wires by Surface-Confined Polymerization. Small, 5,592, (2009)

57. Wang, W.; Shi, X.; Wang, S.; Van Hove, M. A.; Lin, N. Single-Molecule Resolution of an Organometallic Intermediate in a Surface-Supported Ullmann Coupling Reaction. J. Am. Chem. Soc., 133, 13264, (2011)

58. Kittelmann, M.; Rahe, P.; Nimmrich, M.; On-Surface Covalent Linking of Organic Building Blocks on a Bulk Insulator. ACS Nano, 5, 8420, (2011)

59. Dienel, T.; Gómez-Díaz, J.; Seitsonen, A. P.; Dehalogenation and Coupling of a Polycyclic Hydrocarbon on an Atomically Thin Insulator. ACS Nano, 8, 6571, (2014)

60. Morchutt, C.; Björk, J.; Krotzky, S.; Gutzler, R.; Kern, K. Covalent Coupling Via Dehalogenation on Ni(111) Supported Boron Nitride and Graphene. Chem. Commun., 51, 2440,(2015)

61. Kolmer, M.; Ahmad Zebari, A. A.; Prauzner-Bechcicki, J. S.; Polymerization of Polyanthrylene on a Titanium Dioxide (011)-(2_1) Surface. Angew. Chem. Int. Ed., 52, 10300, (2013)

62. Kolmer, M.; Zuzak, R.; Ahmad Zebari, A. A.; On-Surface Polymerization on a Semiconducting Oxide: Aryl Halide Coupling Controlled by Surface Hydroxyl Groups on Rutile TiO2(011). Chem. Commun., 51, 11276, (2015)

63. Lafferentz, L.; Eberhardt, V.; Dri, C.; Controlling On-Surface Polymerization by Hierarchical and Substrate-Directed Growth. Nat. Chem., 4, 215, (2012)

64. Eichhorn, J.; Nieckarz, D.; Ochs, O.; On-Surface Ullmann Coupling: The Influence of Kinetic Reaction Parameters on the Morphology and Quality of Covalent Networks. ACS Nano, 8, 7880, (2014)

65. Cai, J.; Ruffieux, P.; Jaafar, R.; Atomically Precise Bottom-Up Fabrication of Graphene Nanoribbons. Nature, 466, 470, (2010)

66. van der Lit, J.; Boneschanscher, M. P.; Vanmaekelbergh, D.; Suppression of Electron–Vibron Coupling in Graphene Nanoribbons Contacted Via a Single Atom. Nat. Commun., 4, 2023, (2013)

67. Mullick Chowdhury S, Lalwani G, Zhang K, Yang JY, Neville K, Sitharaman B. Cell specific cytotoxicity and uptake of graphene nanoribbons. Biomaterials 34: 283–293, (2013)

68. Lanphere JD, Rogers B, Luth C, Bolster CH, Walker SL. Stability and transport of graphene oxide nanoparticles in groundwater and surface water. Environ Eng Sci 31(7): 350–359, (2014)

69. Lin D, Tian X, Wu F, Xing B, Fate and transport of engineered nanomaterials in the environment. J. Environ. Qual. 39: 1896–1908, (2010)

70. Chen L, Hu P, Zhang L, Huang S, Luo L, Huang C., Toxicity of graphene oxide and multi-walled carbon nanotubes against human cells and zebrafish. Sci. China Chem. 55: 2209–2216, (2012)

71. Talukdar Y, Rashkow JT, Lalwani G, Kanakia S, Sitharaman B. The effects of graphene nanostructures on mesenchymal stem cells. Biomaterials 35(18): 4863–4877, (2014)

72. Chang Y, Yang S-T, Liu J-H, Dong E, Wang Y, Cao A, Liu Y, Wang H., In vitro toxicity evaluation of graphene oxide on A549 cells. Toxicol. Lett. 200: 201–210, (2011)

73. Kanakia S, Toussaint JD, Mullick Chowdhury S, Tembulkar T, Lee S, Jiang YP, Lin RZ, Shroyer KR, Moore W, Sitharaman, B., Dose ranging, expanded acute toxicity and safety pharmacology studies for intravenously administered functionalized graphene nanoparticle formulations. Biomaterials 35(25): 7022–7031, (2014)

74. Wang K, Ruan J, Song H, Zhang J, Wo Y, Guo S, Cui D.. Biocompatibility of graphene oxide. Nanoscale Res. Lett. 6: 1–8, (2011)

75. Seabra AB, Paula AJ, De Lima R, Alves OL, Duran N., Nanotoxicity of graphene and graphene oxide. Chem. Res. Toxicol. 27: 159–16, (2014)

76. Li Y, Yuan H, Von Dem Bussche A, Creighton M, Hurt RH, Kane AB, Gao H., Graphene microsheets enter cells through spontaneous membrane penetration at edge asperities and corner sites. Proc. Natl. Acad. Sci. 110: 12295–12300, (2013)

77. Zhang L, Xia J, Zhao Q, Liu L, Zhang Z., Functional graphene oxide as a nanocarrier for controlled loading and targeted delivery of mixed anticancer drugs. Small 6: 537–544, (2010)

78. Matesanz M-C, Vila M, Feito M-J, Linares J, Goncalves G, Vallet-Regi M, Marques P-AA, Portoles M-T., The effects of graphene oxide nanosheets localized on F-actin filaments on cell-cycle alterations. Biomaterials 34: 1562–1569, (2013)

79. Liao K-H, Lin Y-S, Macosko CW, Haynes CL., Cytotoxicity of graphene oxide and graphene in human erythrocytes and skin fibroblasts. ACS Appl. Mater. Interfaces 3: 2607–2615, (2011)

80. Omid Akhavan, Elham Ghaderi, Hamed Emamy, Fatima Akhavan, Genotoxicity of graphene nanoribbons in human mesenchymal stem cells, Carbon 54, 419-431, (2013)

81. Geim, A. K.; Novoselov, K. S. The rise of graphene. Nature Materials, 6, 183–191, (2007)

82. Geim, A. K. Graphene: status and prospects. Science, 324, 1530–1534, (2009)

83. Novoselov, K. S.; Fal'ko, V. I.; Colombo, L.; Gellert, P. R.; Schwab, M. G.; Kim, K. A. Roadmap for graphene. Nature, 490, 192−200, (2012)

84. J. Lin, A.R.O. Raji, K. Nan, Z. Peng, Z. Yan, E.L.G. Samuel, D. Natelson, J.M. Tour, Iron oxide nanoparticle and graphene nanoribbon composite as an anode material for high-performance Li-ion batteries, Adv. Funct. Mater. 24, 2044–2048, (2014)

85. L. Jian, Z. Peng, C. Xiang, G. Ruan, Z. Yan, D. Natelson, J.M. Tour, Graphene nanoribbon and nanostructured SnO2 composite anodes for lithium ion batteries, ACS Nano 7, 6001–6006, (2013)

86. Y. Zhu, J.M. Tour, Graphene nanoribbon thin films using layer-by-layer assembly, Nano Lett. 10 4356–4362, ((2010)

87. V. Volman, Y. Zhu, A.-R.O. Raji, B. Genorio, W. Lu, C. Xiang, C. Kittrell, J.M. Tour, Radio-frequency-transparent, electrically conductive graphene nanoribbon thin films as deicing heating layers, ACS Appl. Mater. Interfaces 6, 298– 304, (2014)

88. Y. Yang, L. Li, H. Fei, Z. Peng, G. Ruan, J.M. Tour, Graphene nanoribbon/V2O5 cathodes in lithium-ion batteries, ACS Appl. Mater. Interfaces 6, 9590– 9594, (2014).

89. L. Li, A.R.O. Raji, J.M. Tour, Graphene-wrapped MnO2–graphene nanoribbons as anode materials for high-performance lithium ion batteries, Adv. Mater. 25, 6298–6302, (2013)

90. Z. Johari, F.K.A. Hamid, M.T. Ahmadi, F.K.C. Harun, R. Ismail, The effect of interconnect on the circuit performance of 22 nm graphene nanoribbon field effect transistor and MOSFET, J. Comput. Theor. Nanosci. 10, 1305–1309, (2013)

91.X. Wang, Y. Ouyang, X. Li, H. Wang, J. Guo, H. Dai, Room temperature all semiconducting sub-10 nm graphene nanoribbon field-effect transistors, Phys. Rev. Lett. 100, 206803, (2008)

92. C. Stampfer, J. Güttinger, S. Hellmüller, F. Molitor, K. Ensslin, T. Ihn, Energy gaps in etched graphene nanoribbons, Phys. Rev. Lett. 102, 056403, (2009)

93. X. Wang, Y. Ouyang, L. Jiao, H. Wang, L. Xie, J. Wu, J. Guo, H. Dai, Graphene nanoribbons with smooth edges behave as quantum wires, Nat. Nanotechnol. 6, 563–567, (2011)

94. V. Ryzhii, V. Mitin, M. Ryzhii, N. Ryabova, T. Otsuji, Device model for graphene nanoribbon phototransistor, Appl. Phys. Express 1, 669–675, (2008).

95. F. Bonaccorso, Z. Sun, T. Hasan, A.C. Ferrari, Graphene photonics and optoelectronics, Nat. Photonics 4, 611–622, (2010)

96. Kasap, S. O. and Sinha, R.K., Optoelectronics and Photonics: Principles and Practices. (Prentice Hall New Jersey, Vol. 340. (2001)

97. Liu, J. M., Photonic Devices, (Cambridge University Press, 2005)

98. G. W. Ejuh, S. Nouemo, N. F. Tchangnwa et J. M. Ndjaka, "Computational determination of the Electronic and Nonlinear Optical properties of the molecules 2-(4-aminophenyl) Quinoline, 4-(4 aminophenyl) Quinoline, Anthracene, Anthraquinone and Phenanthrene," Mater. Lett. 178 221–226, (2016)

99. F. Karimi, A. H. Davoody, and I. Knezevic, Nonlinear optical response in graphene nanoribbons: The critical role of electron scattering, PHYSICAL REVIEW B97, 245403 (2018)

100. Y. Wang, D. R. Andersen, Third-order terahertz response of gapped, nearly-metallic armchair graphene nanoribbons, Journal of Physics: Condensed Matter, 28, 475301 (2016)

101. Y. Wang, D. R. Andersen, Nonlinear THz response of metallic armchair graphene nanoribbon superlattices, Journal of Physics D: Applied Physics, 49, 46 (2016)

102. X. Jin, Z. Ma, G. Liu, D. Hu, C. Song, In-situ ionothermal precipitation of well-dispersed ZnO nanoparticles onto 2-dimension neat graphene sheets with excellent photocatalytic activity, Journal of Environmental Chemical Engineering, 8, 4, 104030 (2020)

103. L. Brey and H. A. Fertig, "Electronic states of graphene nanoribbons studied with the Dirac equation", Phys. Rev. B 73, 235411(1)-235411(5) (2006)

104. L. Yang, M. L. Cohen, S. G. Louie, "Excitonic effects in the optical spectra of graphene nanoribbons", Nano Lett. 7, 3112–3115 (2007).

105. D. Prezzi, D. Varsano, A. Ruini, A. Marini, E. Molinari, "Optical properties of graphene nanoribbons: the role of many-body effects", Phys. Rev. B 77, 041404(1)-041404(4) (2008).

106. D. Prezzi, D. Varsano, A. Ruini, E. Molinari, "Quantum dot states and optical excitations of edge modulated graphene nanoribbons", Phys. Rev. B 84, 041401(1)-041401(4) (2011).

107. V. W. Brar, M. S. Jang, M. Sherrott, J. J. Lopez, and H. A. Atwater, "Highly Confined Tunable Mid Infrared Plasmonics in Graphene Nanoresonators", Nano Lett. 13, 2541-2547 (2013)

108. H. K. Avetissian, B. R. Avchyan, G. F. Mkrtchian, and K. A. Sargsyan, On the extreme nonlinear optics of graphene nanoribbons in the strong coherent radiation fields, arXiv:2005.09450 [cond-mat.mes-hall] (2020)

109. N. Merino-D´ íez, A. Garcia-Lekue, Width-Dependent Band Gap in Armchair Graphene Nanoribbons Reveals Fermi Level Pinning on Au(111), Nano , 11, 11, 11661–11668, (2017)

110. J. Nakamura, T. Nitta, A. Natori, Electronic and magnetic properties of BNC ribbons, Phys. Rev. B 72, 205429 (2005)

111. B. Sahu, H. Min, A.H. MacDonald, S.K. Banerjee, Energy gaps, magnetism, and electric-field effects in bilayer graphene nanoribbons, Phys. Rev. B 78, 045404 (2008)

112. A. Betti, G. Fiori, G. Iannaccon, Strong mobility degradation in ideal graphene nanoribbons due to phonon scattering, Appl. Phys. Lett. 98, 212111 (2011)

113. F. Schwierz, Graphene transistors, Nat. Nanotechnol. 5, 487–496, (2010)

114. C.W.J. Beenakker, H. V. Houten, Quantum transport in semiconductor nanostructures, Solid State Phys. 44 ,1–228, (2004)

115. J. Baringhaus, M. Ruan, F. Edler, A. Tejeda, M. Sicot, I. Taleb, A.-P. Li, Z. Jiang, E.H. Conrad, C. Berger, C. Tegenkamp, W.A. de Heer, Exceptional ballistic transport in epitaxial graphene nanoribbons, Nature 506, 349–354, (2014)

116. L. Jiao, X. Wang, G. Diankov, H. Wang, H. Dai, Facile synthesis of high-quality graphene nanoribbons, Nat. Nanotechnol. 5, 321–325, (2010)

117. Kokil, A., Yang, K. & Kumar, J. Techniques for Characterization of Charge Carrier Mobility in Organic Semiconductors. J. Polym. Sci. Part B Polym. Phys. 50, 1130–1144 (2012).

118. Obradovic, B., Analysis of Graphene Nanoribbons as a Channel Material for Field-Effect Transistors. Appl. Phys. Lett. 88, 142102 (2006).

119. Kuik, M., 25th Anniversary Article: Charge Transport and Recombination in Polymer Light-Emitting Diodes. Adv. Mater. 26, 512–531 (2014).

120. Chen, Z., Synthesis of Graphene Nanoribbons by Ambient-Pressure Chemical Vapor Deposition and Device Integration. J. Am. Chem. Soc. 138, 15488–15496 (2016)

121. Zdetsis, A. D. & Economou, E. N. Rationalizing and Reconciling Energy Gaps and Quantum Confinement in Narrow Atomically Precise Armchair Graphene Nanoribbons. Carbon 116, 422–434 (2017).

122. Kimouche, A., Ultra-Narrow Metallic Armchair Graphene Nanoribbons. Nat. Commun. 6, 10177 (2015).

123. Jänsch Daniel., Ultra-Narrow Low-Band gap Graphene Nanoribbons from Bromoperylenes—Synthesis and Terahertz-Spectroscopy. Chem. – Eur. J. 23, 4870–4875 (2017).

124. Bennett, P. B., Bottom-Up Graphene Nanoribbon Field-Effect Transistors. Appl. Phys. Lett. 103, 253114 (2013).

125. Llinas, J. P.; Short-Channel Field-Effect Transistors with 9-Atom and 13-Atom Wide Graphene Nanoribbons. Nat. Commun. 8, (2017).

126. V.W.W. Yam, WOLEDs and Organic Photovoltaics (Springer, Heidelberg, 2010)

127. A. E. Becquerel, Comptes Rendus De L'Académie Des Sciences, 9, 145, (1839)

128. A. Marti Green, D. Ewan Dunlop, Prog. Photovolt. 27(7), 565–575 (2019)

129. J.F. Geisz, M.A. Steiner, N. Jain, IEEE J. Photovolt. 8(2), 626–632 (2018)

130. G. P. Smestad, F.C. Krebs, C.M. Lampert, C.G. Granqvist, Sol. Energy Mater. Sol. Cells 92(4), 371–373 (2008)

131. H. Yao, Y. Cui, D. Qian, S. Carlito, J. Am. Chem. Soc. 141(19), 7743–7750 (2019)

132. Y. Li, J. D. Lin, X. Che, Y. Qu, F. Liu, L.S. Liao, J. Am. Chem. Soc. 139(47), 17114–17119 (2017)

133. Zachariah A., Yao L., Volodimyr V., Fulleropyrrolidine interlayers: Tailoring electrodes to raise organic solar cell efficiency, Science 346, (6208), 441-444 (2014)

134. N. Yeh, P. Yeh, Renew. Sustain. Energy Rev. 21, 421–431 (2013)

135. B. A. Gregg, M. C. Hanna, Comparing organic to inorganic photovoltaic cells: Theory, experiment, and simulation, J.Appl.Phys., 15-3-2003, 93, 3605-3614

136. Gevorgyan, S., Production, Characterization and Stability of Organic Solar Cell Devices. Risø National Laboratory for Sustainable Energy. Risø-PhD, No. 55(EN) (2010).

137. R. Kroon, M. Lenes, J. C. Hummelen, P. W. M. Blom, and B. De Boer, Small band gap polymers for organic solar cells (polymer material development in the last 5 years), Polym.Rev., , 48, 531-582 (2008)

138. M. C. Scharber, D. Wuhlbacher, M. Koppe, P. Denk, C. Waldauf, A. J. Heeger, and C. L. Brabec, Design rules for donors in bulk-heterojunction solar cells - Towards 10 % energy-conversion efficiency, Adv.Mater., 17-3-2006, 18, 789-794

139. M. Theander, A. Yartsev, D. Zigmantas, V. Sundstrom, W. Mammo, M. R. Andersson, and O. Inganas, Photoluminescence quenching at a polythiophene/C-60 heterojunction, Physical Review B, 15-5, 61, 12957-12963 (2000)

140. G. Yu and A. J. Heeger, Charge Separation and Photovoltaic Conversion in Polymer Composites with Internal Donor-Acceptor Heterojunctions, J. Appl. Phys., 78, 4510-4515 (1995)

141. H. Paul, C. David, B.P. Rand, Acc. Chem. Res. 42(11), 1740–1747 (2009)

142. M. Riede, T. Mueller, W. Tress, R. Schueppel, K. Leo, Nanotechnology 19, 42 (2008)

143. T. Yang, M. Wang, C. Duan, X. Hu, L. Huang, J. Peng, F. Huang, X. Gong, Energy Environ. Sci. 5(8), 8208–8214 (2012)

144. X. Li, W.C.H. Choy, L. Huo, F. Xie, W.E.I. Sha, B. Ding, X. Guo, Y. Li, J. Hou, J. You, Adv. Mat. 24(22), 3046–3052 (2012)

145. Son, Y.-W; Cohen, L. M.; Louie, G. S. Half-Metallic Graphene Nanoribbons. Nature, 444, 347, (2006)

146. Wakabayashi K., Electronic Transport Properties of Nanographite Ribbon Junctions. Phys. Rev. B, 64, 125428, (2001)

147. Ezawa, M. Peculiar Width Dependence of the Electronic Properties of Carbon Nanoribbons. Phys. Rev. B, 73, 045432 (2006)

148. Bai, J.; Huang, Y. Fabrication and Electrical Properties of Graphene Nanoribbons. Mater. Sci. Eng., R70, 341–353, (2010)

149. Hsu, H.; Reichl, L. E. Selection Rule for the Optical Absorption of Graphene Nanoribbons. Phys. Rev. B, 76, 045418, (2007)

150. Yang, F.; Shtein, M.; Forrest, S. R. Controlled Growth of a Molecular Bulk Heterojunction Photovoltaic Cell. Nat. Mater., 4, 37–4, (2005)

151. X. Gong, M. Tong, F.G. Brunetti, J. Seo, Y. Sun, Bulk Heterojunction Solar Cells with Large Open-Circuit Voltage: Electron Transfer with Small Donor-Acceptor Energy Offset, 23,20 2272-2277, (2011)

152. Brédas, J. L.; Norton, J. S.; Cornil, J.; Coropceanu, V. Molecular Understanding of Organic Solar Cells: The Challenges. Acc. Chem. Res., 42, 1691–1699, (2009)

153. Westenhoff, S.; Howard, I. A.; Hodgkiss, J. M.; Kirov, K. R.; Bronstein, H. A.; Williams, C. K.; Greenham, N. C.; Friend, R. H. Charge Recombination in Organic Photovoltaic Devices with High Open-Circuit Voltage. J. Am. Chem. Soc., 130, 13653–13658, (2008)

154. S. J. Lee, J. Y. Kim, H. P. Kim, D. Kim, An organic photovoltaic featuring graphene nanoribbons, Chem. Commun., 51, 9185-918, (2015)

155. Jensen F., Introduction to computational chemistry (2nd edition), John Wiley and Sons Ltd, the Atrium, Southern Gate, Chichester, West Sussex, England, 192–260, (2007).

156. Fitts D.D., Principles of quantum mechanics: as applied to chemistry and chemical physics, (Cambridge University Press, Cambridge, 2002)

157. Ramachandran K.I., Deepa G. & Namboori K., Computational chemistry and molecular modeling (principles and applications, Springer, Berlin, Germany, 2008)

158. Levine I.N., Quantum chemistry (5th edition), Printice Hall Inc., New Jerzey, USA, 366–600, (2000).

159. Lowe J.P. & Paterson K.A., Quantum chemistry (3rd edition), Elsevier Academic Press, London, England, pp. 168–178, (2006)

160. Orio M., Pantazis D.A. & Neese F.. Density functional theory. Photosynthesis Research, 102, 443–453, (2009)

161. Szabo A. & Ostlund N.S., Modern quantum chemistry: introduction to advanced electronic structure theory (Dover publications Inc., New York, USA, 43–55, 1989)

162. Hehre J.H., A guide to molecular mechanics and quantum chemical calculations, Wavefunction, Inc., Irvine, USA, pp. 753–771, (2003).

163. Atkins P.W. & Friedman R.S., Molecular quantum mechanics (3rd edition), (Oxford University press, Oxford, USA, 278–318, 1999).

164. Young D.C., Computational chemistry: a practical guide for applying techniques to real-world problems (John Wiley & Sons Inc., New York, USA, 19–45, 2001)

165. Lewars G.E., Computational chemistry: introduction to the theory and applications of molecular and quantum mechanics (2nd edition), Springer, New York, USA, 175–510, (2011)

166. Adamo C. & Jacquemin D., The calculations of excited-state properties with time-dependent density functional theory. Chemical Society Reviews, 42, 845–856, (2013).

167. Peverati R. & Truhlar D.G., Quest for a universal density functional: the accuracy of density functionals across a broad spectrum of databases in chemistry and physics. Philosophical Transactions of the Royal Society, A372, 1–52, (2014).

168. Kumar A., Deval V., Tandon P., Gupta A. & D'silva E.D., Experimental and theoretical (FT-IR, FT-Raman, UV–Vis, NMR) spectroscopic analysis and first-order hyperpolarizability studies of non-linear optical material: (2E)-3-[4-(methylsulfanyl) phenyl]-1-(4-nitrophenyl) prop-2-en-1-one using density functional theory. Spectrochimica Acta part A, 130, 41–53, (2014).

169. A.V. Sinitskiy, V.S. Pande, Deep neural network computes electron densities and energies of a large set of organic molecules faster than density functional theory (DFT), arXiv:1809.02723 (2018)

170. Hohenberg P. & Kohn W., Inhomogeneous electron gas. Physical Review, 136, B864–B871, (1964).

171. Cramer C.J., Truhlar D.G., Density functional theory for transition metals and transition metal chemistry. Physical Chemistry Chemical Physics, 11, 10757–10816, (2009)

172. Geerlings P., De Proft F., Langenaeker W., Conceptual density functional theory. Chemical Reviews, 103, 1793–1873, (2003)

173. Koch W. & Holthausen M.C., A chemist's guide to density functional theory (2nd edition), (Wiley-VCH Verlag GmbH, New York, USA, 3–89, 2001).

174. Parr R.G. & Yang W., (Density-Functional Theory of Atoms and Molecules, (Oxford University Press, New York, USA, 1989)

175. Tsipis A.C., DFT flavor of coordination chemistry. Coordination Chemistry Reviews, 272, 1–29, (2014)

176. Becke A.D., Density-functional exchange-energy approximation with correct asymptotic behavior. Physical Review A, 38, 3098–3100, (1988).

177. Lee C.T., Yang W.T. & Parr R.G., Development of the colle-salvetti correlation-energy formula into a functional of the electron-density. Physical Reviews B - Condensed Matter and Materials Physics, 37, 785–789, (1988).

178. Perdew J. P., Density-functional approximation for the correlation energy of the inhomogeneous electron gas. Physical Review B, 34, 8822–8824, (1986).

179. Perdew J.P., Burke K. & Ernzerhof M., Generalized gradient approximation made simple. Physical Review Letters, 77, 3865–3868, (1996).

180. Y. & Truhlar D.G., A New Local Density Functional for Main-Group Thermochemistry, Transition Metal Bonding, Thermochemical Kinetics, and Noncovalent Interactions. The Journal of Chemical Physics, 125, 194101: 1–18, (2006).

181. Tao J., Perdew J.P., Staroverov V.N. & Scuseria G.E., Climbing the density functional ladder: nonempirical meta-generalized gradient approximation designed for molecules and solids. Physical Review Letters, 91, 146401, (2003).

182. Zhao Y. & Truhlar D.G., Applications and validations of the Minnesota density functionals. Chemical Physics Letters, 502, 1–13, (2011)

183. Matczak P. & Wojtulewski S., Performance of Møller-Plesset second-order perturbation theory and density functional theory in predicting the interaction between stannylenes and aromatic molecules. Journal of Molecular Modeling, 21, 41, (2015).

184. Yanai T., Tew D.P. & Handy N.C., A new hybrid exchange–correlation functional using the coulomb-attenuating method (CAM-B3LYP). Chemical Physics Letters, 393, 51–57, (2004)

185. Chai J-D. & Head-Gordon M., Systematic optimization of long-range corrected hybrid density functionals. The Journal of Chemical Physics, 128, 084106, (2008).

186. García de la Vega J.M. & Miguel B., Basis sets for computational chemistry (Chapter 3), Montero L.A., Díaz L.A. & Bader R. (ed), Introduction to advanced topics of computational chemistry, Editorial de la Universidad de La Habana, Havana, 41–70, (2003)

187. Rappoport D. & Furche F., Property-optimized Gaussian basis sets for molecular response calculations. The Journal of Chemical Physics, 133, 134105, (2010)

188. Zheng J., Xu X. & Truhlar D.G., Minimally Augmented Karlsruhe Basis Sets. Theoretical Chemistry Accounts, 128, 295–305, (2011)

189. Gaussian 09, Revision A.02, M. J. Frisch, G. W. Trucks, H. B. Schlegel, G. E. Scuseria, M. A. Robb, J. R. Cheeseman, G. Scalmani, V. Barone, B. Mennucci, G. A. Petersson, H. Nakatsuji, M. Caricato, X. Li, H. P. Hratchian, A. F. Izmaylov, J. Bloino, G. Zheng, J. L. Sonnenberg, M. Hada, M. Ehara, K. Toyota, R. Fukuda, J. Hasegawa, M. Ishida, T. Nakajima, Y. Honda, O. Kitao, H. Nakai, T. Vreven, J. A. Montgomery, Jr., J. E. Peralta, F. Ogliaro, M. Bearpark, J. J. Heyd, E. Brothers, K. N. Kudin, V. N. Staroverov, R. Kobayashi, J. Normand, K. Raghavachari, A. Rendell, J. C. Burant, S. S. Iyengar, J. Tomasi, M. Cossi, N. Rega, J. M. Millam, M. Klene, J. E. Knox, J. B. Cross, V. Bakken, C. Adamo, J. Jaramillo, R. Gomperts, R. E. Stratmann, O. Yazyev, A. J. Austin, R. Cammi, C. Pomelli, J. W. Ochterski, R. L. Martin, K. Morokuma, V. G. Zakrzewski, G. A. Voth, P. Salvador, J. J. Dannenberg, S. Dapprich, A. D. Daniels, O. Farkas, J. B. Foresman, J. V. Ortiz, J. Cioslowski, and D. J. Fox, Gaussian, Inc., Wallingford CT, (2009).

190. Ray Dennington, Todd Keith and John Milam, GaussView, Version 5., Semichem Inc., Shawnee Mission KS, (2009)

191. P. Calaminici, K. Jug et A. M. Köster, “Density functional calculations of molecular polarizabilities and hyperpolarizabilities,” J. Chem. Phys. 109 (18), 7756-7763, (1998)

192. F. Mançois, “Nouveaux composés photochimiques dédiés aux applications optiques Non Linéaires,” Université Bordeaux 1, thèse de doctorat 1-208, (2009)

193. H. D. Cohen et C. C. J. Roothaan, “Electric Dipole Polarizability of Atoms by the Hartree—Fock Method. I. Theory for Closed-Shell Systems,” The Journal of Chemical Physics 43 (10) 34-39, (1965)

194. N. K. Nkungli J. N. Ghogomu, Concomitant Effects of Transition Metal Chelation and Solvent Polarity on the First Molecular Hyperpolarizability of 4-Methoxyacetophenone Thiosemicarbazone: A DFT Study, J. theoretical Chemistry, 10.1155 7909576 (2016)

195. A. Francisco, M.G. SantosaLuis, D. AbegãoafRuben. Fonseca, Bromo-and chloro-derivatives of dibenzylideneacetone: Experimental and theoretical study of the first molecular hyperpolarizability and two-photon absorption, Journal of Photochemistry and Photobiology A, 369 70-76 (2019)

196. F. REIF, "Fundamentals of Statistical and Thermal Physics," McGraw-Hill 5 1-651, (1965)

197. K. Fukui, T. Yonezawa, C. Nagata, "Molecular orbital theory of orientation in aromatic, heteroaromatic, and other conjugated molecules," The Journal of Chemical Physics 22 (8) 1433-1442, (1954)

198. K. Fukui, "The role of frontier orbitals in chemical reactions (Nobel Lecture)," Angewandte Chemie International Edition in English 21 (11) 801-809, (1982)

199. A. Veved, G. W. Ejuh, N. Djongyang, Study of the optoelectronic and piezoelectric properties of ZrO2 doped PVDF from quantum chemistry calculations, Chinese Journal of Physics 63 213–219, (2020)

200. C. Fonkem, G. W. Ejuh,• F. Tchangnwa Nya, R. A. Yossa Kamsi, J. M. B. Ndjaka, Theoretical study of optoelectronic properties of the molecule 2-cyano-3-[4-(diphenylamino)phenyl] acrylic acid, 17(3), 533–543, (2019)

201. G. Maragatham, S. Selvarani, P. Rajakumar, S. Lakshmi, Structure determination and quantum chemical analysis of chalcone derivatives, J. Mol. Struct. (2018), 1179(5), , 568-575, (2019)

202. S. Ranjini, T.K. Kundu, Nonbonding interaction analyses on PVDF/ [BMIM] [BF4] complex system in gas and solution phase, J. Mol. Model. 25, 131, (2019)

203. R. Sarkar, T.K. Kundu, Density functional theory studies on PVDF/ionic liquid composite systems, J. Chem. Sci. 130 (8) 115, (2018)

204. R. Ghoreishi, M. Kia, Chemical reactivity and adsorption properties of pro-carbazine anti-cancer drug on gallium-doped nanotubes: a quantum chemical study, J. Mol. Model. 25 (2), 46, (2019)

205. V. Lemaur, M. Steel, D. Beljonne, J.-L. Brédas and J. Cornil, J. Am. Chem. Soc. 127, 6077, (2005)

206. D.L. Cheung and A. Troisi, Theoretical study of the organic photovoltaic electron acceptor PCBM: Morphology, electronic structure, and charge localization, J. Chem. Phys. 114, 20479, (2010)

207. Y.A. Duan, Y. Geng, H.B. Li, J.L. Jin, Y. Wu, Z.M. Su, Theoretical characterization and design of small molecule donor material containing naphthodithiophene central unit for efficient organic solar cells, J Comput. Chem., 34 (19) 1611-1619 (2013)

208. J. Cornil, D. Beljonne, J. P. Calbert and J. L. Bre´das, Adv. Mater., 13, 1053, (2001)

209. R Sun, D Deng, J Guo, Q Wu, J Guo, Spontaneous open-circuit voltage gain of fully fabricated organic solar cells caused by elimination of interfacial energy disorder, energy and environmental science, 8 (2019)

210. H. Bronstein, C.B. Nielsen, B.C. Schroeder, The role of chemical design in the performance of organic semiconductors, Nature Reviews Chemistry volume 4, 66–77 (2020)

211. W. Tress, K. Domanski, B. Carlsen, A. Agarwalla, Performance of perovskite solar cells under simulated temperature-illumination real-world operating conditions, Nature Energy volume 4, 568–574 (2019)

212. M. Stolterfoht, P. Caprioglio, The impact of energy alignment and interfacial recombination on the internal and external open-circuit voltage of perovskite solar cells, Energy Environ. Sci.,12 2778-2788 (2019)

213. S. Yang, J. Dai, Z. Yu, Y. Shao, Y. Zhou, Tailoring passivation molecular structures for extremely small open-circuit voltage loss in perovskite solar cells, J. Am. Chem. Soc. 141, 14 5781-5787 (2019)

214. E. Zimmermann, P. Ehrenreich, T. Pfadler, Erroneous efficiency reports harm organic solar cell, Nature Photonics volume 8, 669–672 (2014)

215. S.S. Shin, J.H. Suk, B.J. Kang, W. Yin, S.J. Lee, Energy-level engineering of the electron transporting layer for improving open-circuit voltage in dye and perovskite-based solar cells, Energy Environ. Sci.,12 958-964 (2019)

216. A. Guillen-Lopez, M. Robles, Electronic structure and non-linear optical properties of organic photovoltaic systems with potential applications on solar cell devices, Theoretical Chemistry Accounts, 137 (85) 1432-2234 (2018)

217. Q.Q. Pan, S.B. Li, Y. Wu, G. Sun, Y. Geng, Z. M. Su, A comparative study of a fluorene-based non-fullerene electron acceptor and PC61BM in an organic solar cell at a quantum chemical level RSC Adv, 6 81164-81173 (2016)

218. M. Sui, S. Li, Q. Pan, G. Sun, Y. Geng, Theoretical characterization on photoelectric properties of benzothiadiazole- and fluorene-based small molecule acceptor materials for the organic photovoltaics, J Mol Model 23 (28) 1610-2940 (2017)

219. R. A. Yossa Kamsia, G.W. Ejuh, P. Mkoungae, J.M.B. Ndjakaa, Study of the molecular structure, electronic and chemical properties of Rubescin D molecule, Chinese Journal of Physics 63 104–121, (2020)

220. S. Ramalingam, M. Karabacak, S. Periandy, N. Puviaran, D. Tanuja, Spectroscopic (infrared, Raman, UV and NMR) analysis, Gaussian hybrid computational investigation (MEP maps/HOMO and LUMO) on cyclohexanoneoxime, Spectrochim. Acta Part A Mol. Biomol. Spectrosc. 96 207–220, (2012)

221. H. Tanak, A. A. Agar, O. Buyukgungor, Experimental (XRD, FT-IR and UV–Vis) and theoretical modeling studies of Schiff base (E)-N′-((5-nitrothiophen-2-yl)methylene)-2-phenoxyaniline, Spectrochim. Acta Part A, 118(29) 672–682, (2014)

222. J. Yao, Z. Cai, Z. Liu, C. Yu, H. Luo, Y. Yang, S. Yang, G. Zhang and D. Zhang, Macromolecules, 48, 2039-2047, (2015)

223. G.W. Ejuh, F. Tchangnwa Nya, M.T. Ottou Abe, F.F. Jean-Baptiste, J.M.B. Ndjaka, Electronic structure, physico-chemical, linear and nonlinear optical properties analysis of coronene, 6B-, 6N-, 3B3N-, substituted C24H12 using RHF, B3LYP and wB97XD methods, Opt. Quant. Electron. 49, 382, (2017)

224. F. REIF, “Fundamentals of Statistical and Thermal Physics,” McGraw-Hill 5, 1-651, (1965)

225. H. Alyar, “A review on nonlinear optical properties of donoracceptor derivatives of naphthalene and azanaphthalene,”Reviews on Advanced Materials Science, 34(1) 79–87, (2013)

226. Pearson, R.G. Hard and soft acids and bases. J. Am. Chem. Soc. 85, 3533–3539, (1963)

227. C. Yang, J. Zhang, N. Liang, H. Yao, Effects of energy-level offset between a donor and acceptor on the photovoltaic performance of nonfullerene organic solar cells, J. Mater. Chem. A 32 (7), 18889-18897(2019)

228. M. Horie, J. Kettle, C.Y Yu, L. A. Majewski, S.W. Chang, J. Kirkpatrick, S.M. Tuladhar, Cyclopentadithiophene-benzothiadiazole oligomers and polymers; synthesis, characterisation, field-effect transistor and photovoltaic characteristics, J Mater Chem 22 381–389 (2012)

229. K. Tvingstedt, K. Vandewal, A. Gadisa, F. Zhang, J. Manca, O. Inganäs, Electroluminescence from charge transfer states in polymer solar cells, J Am Chem Soc. 131 (33) 11819- 11824 (2009)

230. D.B. Staple, P.A.K Oliver, I.G. Hill, Derivation of the open-circuit voltage of organic solar cells, Phys Rev B 89 (20) 1719 (2014)

231. Y Ie, M Karakawa, S Jinnai, H Yoshida, Electron-donor function of methanofullerenes in donor–acceptor bulk heterojunction systems Chem. Commun., 50, 4123-4125 (2014)

232. G.A. Buxton, N. Clarke, Predicting structure and property relations in polymeric photovoltaic devices, Phys. Rev. B 74, 085207 (2006)

233. D. Mhlbacher, M. Scharber, M. Morana, Z. Zhu, D. Waller, R. Gaudiana, C. Brabec, High photovoltaic performance of a low band gap polymer. Adv Mat 18(21) 2884–2889 (2006)

234. R.A. Marcus, Electron transfer reactions in chemistry. Theory and experiment, Rev. Mod. Phys. 65 (3) 599 (1993)

235. R. A. Marcus, Chemical and electrochemical electron-transfer theory, Annu. Rev. Phys. Chem. 15 (1) 155–196 (1964)

236. M. Bourass, A. Touimi Benjelloun, M. Benzakour, M. Mcharfi, F. Jhilal, F. Serein-Spirau, DFT/TD-DFT characterization of conjugational electronic structures and spectral properties of materials based on thieno[3,2-b][1]benzothiophene for organic photovoltaic and solar cell applications, Journal of Saudi Chemical Society 21 563–574 (2017)

237. R. Jin, K. Lia and X. Hana, Improving optoelectronic and charge transport properties of D–p–D type diketopyrrolopyrrolepyrene derivatives as multifunctional materials for organic solar cell applications, RSC Adv., 9, 22597, (2019)

238. B. C. Lin, C. P. Cheng, Z. Q. You and C. P. Hsu, Charge transport properties of tris (8-hydroxyquinolinato) aluminum (III): Why it is an electron transporter, J. Am. Chem. Soc., 127, 66–67, (2005).

239. Bredas J. L., Beljonne D, Coropceanu V, Cornil, Charge-transfer and energy-transfer processes in π-conjugated oligomers and polymers: a molecular picture, J Chem Rev 104 4971, (2004)

240. M. Senge, M. Fazekas, E. Notaras, W. Blau, M. Zawadzka, Nonlinear optical properties of porphyrins. Adv Mat 19(19) 2737–2774 (2007)

241. M.D. Balanay, O.H. Kim, Optical properties of porphyrin analogues for solar cells: an NLO approach. Curr Appl Phys 11 109–116 (2011)

242. C.R. Zhang, Z.J. Liu, Y.H. Chen, H.S. Chen, Y.Z. Wu DFT and TD-DFT study on structure and properties of organic dye sensitizer TA-St-CA. Curr Appl Phys 10 (1) 77–83 (2010)

243. C.R. Zhang, Z.J. Liu, Y.H. Chen, H.S. Chen, Y.Z. Wu DFT and TDDFT study on organic dye sensitizers D5, DST and DSS for solar cells. J Mol Struct Theochem 899 86–93, (2010).

244. H Yin, KL Chiu, P Bi, G Li, C Yan, Enhanced electron transport and heat transfer boost light stability of ternary organic photovoltaic cells incorporating non-fullerene small molecule and polymer, 5,10 1900497, (2019)

245. Z. He, C. Zhong, S. Su, M. Xu, H. Wu, and Y. Cao, Enhanced power-conversion efficiency in polymer solar cells using an inverted device structure, Nat. Photon 6 591–595 (2012)

246. A. Hinchliffe1and H. J. S. Machado, Density Functional Studies of Molecular Polarizabilities. Anthracene and Phenanthrene, Int. J. Mol. Sci, 1, 8-16, (2000)

LIST OF PUBLICATIONS

1 **E. MAINIMO**, G.W. Ejuh, J.M.B. Ndjaka, Metal modulated effects on the optoelectronic and charge transport properties of some graphene nanoribbons, optical and quantum electronics, 53 (4), 1-14 (2021)

2 **E. MAINIMO**, G.W. Ejuh, J.M.B. Ndjaka , Effect of metalation on some graphene nanoribbons for potential application as donor in organic photovoltaic cells, journal of materials science: materials in electronics 31(24), 21923-21933, (2020)